

T.C.
MARMARA UNIVERSITY
INSTITUTE FOR GRADUATE STUDIES IN
PURE AND APPLIED SCIENCES

126157

MODIFICATION AND DEVELOPMENT
OF AN INTERNAL COMBUSTION ENGINE
SIMULATION COMPUTER PROGRAM

Barış YILMAZ
(1411018-19990074)

THESIS
FOR THE DEGREE OF MASTER OF SCIENCE
IN
MECHANICAL ENGINEERING PROGRAMME

T.C. YÜKSEKÖĞRETİM KURULU
DOKÜMANTASYON MERKEZİ
SUPERVISOR
Doç.Dr. M. Zafer GÜL

İSTANBUL 2002

126157

MARMARA UNIVERSITY
THE INSTITUTE FOR
GRADUATE STUDIES IN PURE AND APPLIED SCIENCES

ACCEPTANCE AND APPROVAL DOCUMENT

**MODIFICATION AND DEVELOPMENT OF AN INTERNAL
COMBUSTION ENGINE SIMULATION COMPUTER PROGRAM**

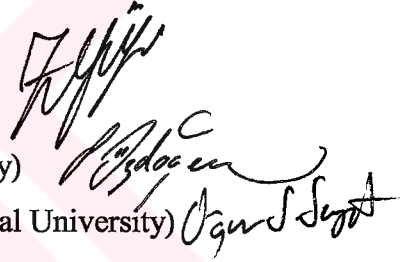
Established committee listed below, on July.23, 2002 and 2002/13-15.... by the *INSTITUTE FOR GRADUATE STUDIES IN PURE AND APPLIED SCIENCES*' Executive Committee, have accepted Mr.Barış YILMAZ 's Master of Science thesis, titled as "MODIFICATION AND DEVELOPMENT OF AN INTERNAL COMBUSTION ENGINE SIMULATION COMPUTER PROGRAM" in Mechanical Engineering.

COMMITTEE

Advisor : Doç Dr. M. Zafer GÜL (Marmara University)

Member : Prof. Dr. Sibel ÖZDOĞAN (Marmara University)

Member : Doç. Dr. Oğuz Salim SÖĞÜT (Istanbul Technical University)



Date of thesis' / dissertation's defense before the committee : 15.08.2002

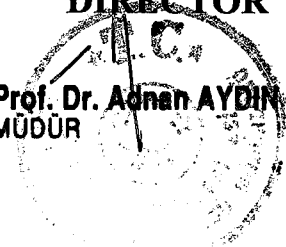
APPROVAL

Mr. / Mrs. / Miss. Barış YILMAZ..... has satisfactorily completed the requirements for the degree of ~~Doctor of Philosophy~~ / Master of Science in Mechanical Engineering..... at Marmara University.

Mr. / Mrs. / Miss. Barış YILMAZ..... is eligible to have the degree awarded at our convocation on 2002/16-29.12.2002 Diploma and transcripts so noted will be available after that date.

Istanbul

DIRECTOR
Prof. Dr. Adnan AYDIN
MÜDÜR



ACKNOWLEDGEMENT

I would like to express my gratitude to my advisor, M. Zafer GUL, for his advice, support and encouragement throughout preparing this thesis. I would like to thank Barbaros GENCER for his helps in preparing preprocessor program. I would also like to thank my officemates for their helps in every way and my parents and brothers for their supports and encouragements in preparing this thesis.

07.08.2002

Barış YILMAZ

CONTENTS

	PAGE
ACKNOWLEDGEMENT	I
CONTENTS	II
ÖZET	V
ABSTRACT	VII
CLAIM FOR ORIGINALITY	IX
LIST OF SYMBOLS.....	X
Greek letters	XI
ABBREVIATIONS.....	XII
LIST OF FIGURES.....	XIII
LIST OF TABLES.....	XV
PART I INTRODUCTION AND OBJECTIVES	1
I.1. INTRODUCTION.....	1
I.2. THE PROBLEM STAMENT.....	2
PART II GENERAL BACKGROUND	3
II.1. INTRODUCTION	3
II.2. REVIEW OF RELATED LITERATURE	4
II.2.1. Computational Studies	4
II.2.2. Turbulence Modeling Aspects	6
PART III MATHEMATICAL MODEL.....	8
III.1. INTRODUCTION.....	8
III.1.1. The General Governing Equations.....	8

III.1.2. Ensemble-Averaged Equations	10
III.1.3. Boundary Conditions	13
III.1.3.1. Walls, Stagnation Enthalpy, Symmetry Axis	14
III.1.3.2. Boundary Conditions At Planes Of Inlet And Exhaust Apertures..	14
III.1.4. Equations For Moving Coordinate Frames	15
PART IV TURBULENCE MODEL	18
IV.1. WHAT IS TURBULENCE	18
IV.2. TURBULENCE MODELS	19
IV.2.1. Mixing Length Model	21
IV.2.2. The k-ε model	22
IV.2.2.1 The k -equation	23
IV.2.2.2 The ε -Equation.....	24
IV.2.3 The k-ε model variants:	26
IV.2.4. The modified k-ε-τ model	27
IV.2.4.1. Boundary conditions.....	29
IV.2.4.1.a. Walls, Stagnation Enthalpy and Symmetry Axis.....	29
IV.2.4.1.b. Planes of inlet and exhaust apertures.....	30
PART V SOLUTION PROCEDURE	31
V.1. INTRODUCTION	31
V.2. METHOD OF DISCRETIZATION	31
V.2.1. Derivation of The General Difference Equations	32
V.2.2. The Differencing Schemes:	34
V.2.2.1. Assessment Of Boundary conditions:	35
V.3 OVERALL SOLUTION PROCEDURE	36
V.3.1. Solution of Discretized Equations:	38
V.3.2. Outline of The Solution Procedure	38
PART VI THESIS STUDIES AND RESULTS	41
VI.1. THESIS STUDIES	41
VI.1.1. The Specification of The Inlet and Initial Conditions	44
VI.2. RESULTS AND DISCUSSIONS	45
VI.2.1. The Predictions and Comparisons for Case I	45
VI.2.1.1. Induction Stroke (TDC to $\Theta=180^\circ$ CA).....	45
VI.2.1.2. Compression Stroke ($\Theta=180^\circ$ CA to $\Theta=360^\circ$)	46
VI.2.1.3. Comparison of Results with The Experimental Data	48
VI.2.2. The Predictions and Comparisons for Case II	50
VI.2.2.1. Induction Stroke (TDC to $\Theta=180^\circ$ CA).....	50
VI.2.2.2. Compression Stroke ($\Theta=180^\circ$ CA to $\Theta=360^\circ$)	50
VI.2.2.3. Comparison of Results with The Experimental Data	51
PART VII DISCUSSIONS AND EVALUATIONS	53

REFERENCES	88
APPENDIX A.....	90
APPENDIX B.....	91
APPENDIX C.....	114
CURRICULUM VITAE	115



ÖZET

Son on yıl içinde, yakıt ekonomisinin artırılması, gürültü ve atık seviyelerinin azaltılması için içten yanmalı motorlar ile ilgili pekçok araştırma yapılmaktadır. Bu durum, içten yanmalı motor içi akışın gelişimi ve yanma ile etkileşimi hakkında daha fazla bilgi gerektirir.

İçten yanmalı motor silindirlerindeki akışın zamana bağımlı, üç boyutlu ve hareketli sınır koşullarına sahip olması nedeniyle sayısal veya deneysel olarak incelenmesi oldukça zordur. Bunun yanında, motor çevrimlerinde akış çoğunlukla türbülanslıdır. Bu yüzden, analiz yapmak akışın düzenli olduğu durumlardan daha zordur.

Akış gelişiminin detaylı analizi kütle, momentum ve enerji korunum kısmı diferansiyel denklemlerinin çözümünü gerektirir. Bu diferansiyel denklemler lineer değildir, birbiriyle ilişkilidir ve denklemleri analitik olarak çözmek oldukça zordur. Sayısal yöntemlerle çözüm yanma odasının birbirine komşu sonlu kontrol hacimlere bölünmesiyle başlar. Daha sonra, diferansiyel denklemler sonlu hacimler biçimine dönüştürülür. Son olarak, bu dönüştürülmüş denklemler çözüm algoritmaları kullanılarak çözülür. Ayrıca, silindir içindeki türbülans alanını modellemek için ek denklemler gerekir. Türbülans modelleri ile ilgili pekçok çalışma vardır; örneğin 'the mixing length' modeli, k - ε türbülans modeli ve versiyonları gibi.

İçten yanmalı motor içi akışlarının diğer akış türlerinden farklılığı hacimsel sıkıştırma ve genişleme özellikleridir. Standart k - ε türbülans modeli bu durumlar için doğru sonuçlar vermemektedir. Bu nedenle, bu model motor içi akışlar için çeşitli çalışmalarda yeniden düzenlenmiştir. Morel ve Mansour sıkıştırma etkilerini modelleyen en iyi versiyonlardan birini geliştirmiştir.

İki-denklemlerinin eksikliklerini gidermek için üç-denklemler model, k - ε - τ türbülans modeli, geliştirildi. Bu tez çalışmasında üç-denklemler modelinin geliştirilmiş bir versiyonu kullanıldı.

Bu çalışmada, üç-denklemler modeli ile Morel ve Mansour iki-denklemler modeli sonuçları çeşitli motor içi akış durumları için karşılaştırıldı. Bu karşılaştırmalar düz yüzeyli piston için farklı iki sıkıştırma oranındaki sonuçları içerir. Ayrıca, her iki modelden elde edilen sonuçlar Lazer Doppler Anemometre ile elde edilmiş deneysel sonuçlarla karşılaştırıldı. Sonuçta, $k-\varepsilon-\tau$ turbülans modelinin karşılaştırma yapılan çoğu noktada $k-\varepsilon$ turbülans modelinden daha iyi ortalama aksel hız ve turbülans çalkantı profilleri verdiği gözlemlendi.

07.08.2002

Barış YILMAZ



ABSTRACT

There are a plenty of researchs, especially in last decade, on internal combustion engines in order to increase the fuel economy and to decrease the level of noise and waste. That requires the more complete understanding of flow evolution and its interaction with the combustion in internal combustion engine cylinder.

Fluid flow within internal combustion engine cylinders is extremely complex to analyse numerically or experimentally due to having time-dependent and three dimensional characteristics with moving boundaries. Moreover, the flow is mostly turbulent in engine cycles, so, making analysis very difficult, than if it were laminar flow.

The detailed analysis of flow evolution requires solution of the governing partial differential equations of conservation of mass, momentum and energy. These are non-linear, coupled and too complex to allow analytical solutions. The numerical solutions start with discretizing the combustion chamber volume into adjacent control volumes of finite dimensions. Then, the governing differential equations converted into finite volume form. Finally, this discretized equations are solved by using solution algorithms. Furthermore, additional equations are required for the modeling of the turbulence field in cylinder. There are a lot of works on turbulence models such as the mixing length model, the $k-\varepsilon$ turbulence model and its variants.

The distinctiveness of the internal combustion engine flows is the bulk expansion and compression characteristics. The standard $k-\varepsilon$ turbulence model does not give accurate results for these cases. So, this model has been modified in several internal combustion engine researches. The Morel and Mansour model is one of the best variant in simulating the compression effects.

A three-equation model, $k-\varepsilon-\tau$ turbulence model, was developed to overcome the deficiencies in two-equation model. A modified version of three-equation model was used in this thesis.

In this study, results of the $k-\varepsilon-\tau$ turbulence model and Morel and Mansour $k-\varepsilon$ turbulence model were compared for various in-cylinder engine flows. These include two different compression ratios with flat-top piston cases. Results of both models were also compared with the Laser Doppler Anemometry measurements. It was seen that the modified version of $k-\varepsilon-\tau$ turbulence model produced better axial mean velocity and turbulence intensity profiles in most of the locations than did $k-\varepsilon$ model.

07.08.2002

Bariş YILMAZ

CLAIM FOR ORIGINALITY

In this study, an internal combustion engine simulation program was modified and restructured for testing the performance of three-equation, $k-\varepsilon-\tau$, turbulence model. Results for two different compression ratios with flat-top piston cases were compared with the two-equation model version and measurements.

Similar studies have been made on different simulation programs, using different turbulence models, and different grid densities. However, the modifications and grid densities, used in this thesis for three-equation model, have not been studied before.

07.08.2002

Assoc. Prof. Zafer GÜL

Barış YILMAZ

LIST OF SYMBOLS

A	:	Coefficient of finite volume equations (subscripted P, W, E, S, SW, SE, NW and NE)
a	:	Cell-face area (subscripted w, e, s, and n)
A_M	:	Minimum area of the valve throat
B	:	Cylinder (Bore) diameter
C_D	:	Valve discharge coefficient
$C_{\epsilon 1}, C_{\epsilon 2}, C_{\epsilon 3}$:	Coefficients of ϵ -equation
$C_{\tau 1}, C_{\tau 2}$:	Coefficients of τ -equation
D	:	Valve diameter
f	:	Weighting factor
h_s	:	Stagnation enthalpy
k	:	Turbulent kinetic energy
L	:	Valve lift
L_{cr}	:	Connecting rod length
L_{max}	:	Maximum valve lift
l	:	Dissipation length scale
\dot{m}	:	Mass flow rate through the valve
P	:	Pressure, control volume center when used as subscript
P_{cyl}	:	Cylinder mean pressure
Pe	:	Pecklet number
P_k	:	Turbulence kinetic energy production
R	:	Radial coordinate
S_ϕ	:	Source term in the partial differential and finite difference equations
U	:	Instantaneous velocity
\overline{U}	:	Mean (time or ensemble averaged) velocity
$\overline{\overline{U}}$:	Density weighted ensemble averaged velocity
U_{in}	:	Inlet velocity
u	:	Turbulence fluctuations about \overline{U}
u^*	:	Turbulence fluctuations about $\overline{\overline{U}}$
u'	:	Turbulence intensity
V_r	:	Radial velocity
\overline{V}_p	:	Mean piston velocity
y^+	:	Dimensionless distance from cylinder wall
z	:	Axial coordinate
z_{sep}	:	width of the reverse flow region at wall

Greek letters

α	:	Spatial difference coefficient
β	:	Temporal difference coefficient
ε	:	Turbulence energy dissipation rate
γ	:	Ratio of the specific heats
Γ	:	Turbulent diffusivity
δ_{ij}	:	Kronecker delta
θ	:	Circumferential coordinate
Θ	:	Crank angle
μ	:	Molecular viscosity
μ_t	:	Turbulence viscosity
ν	:	Kinematic viscosity
ξ	:	Non-dimensional axial coordinate
ρ	:	Density
σ_t	:	Turbulent Prandtl/Schmidt number
σ_{ij}	:	Stress tensor
τ	:	Time scale of turbulence energy containing edies
ϕ	:	A dependent variable
ω	:	Engine angular velocity

ABBREVIATIONS

ASM	:	Algebraic Stress Model
BSHD	:	Bounded Scew Hybrid Differencing Scheme
CA	:	Crank Angle
CFD	:	Computational Fluid Dynamics
DNS	:	Direct Numerical Simulation
DSM	:	Differential Stress Model
DWEA	:	Density Weighted Ensemble Averaging
IC	:	Internal Combustion
MM	:	Morel & Mansour
PDE	:	Partial Differential Equation
PISO	:	Pressure Implicit by Splitting of Operators
EPISO	:	Engine PISO
SIMPLE	:	Semi-Implicit Method for Pressure-Linked Equations
TDC	:	Top Dead Center
TDMA	:	Tri-Diagonal Matrix Algorithm
2D	:	Two-Dimensional
3D	:	Three-Dimensional

LIST OF FIGURES

	<u>PAGE</u>
Figure III.1 ... : System configuration and coordinate frame.	17
Figure III.2 : System configuration within moving coordinate frame	17
Figure V.1 : Computational grids, notation and control volumes of scalar variables and axial and radial velocities.	32
Figure VI.1 : Diagram of Imperial College compressing engine simulator and engine cylinder.	42
Figure VI.2 : Variation of valve lift, piston speed and cylinder pressure with crank angle of the model engines	43
Figure VI.3 : Computational grid arrangements; for test Case I and Case II.	54
Figure VI.4 : Velocity field predictions of <i>the MM k-ε model</i> for test Case I at various crank angles in particle tracking and vector plots	55
Figure VI.5 : Velocity field predictions of <i>the k-ε-τ model</i> for test Case I at various crank angles in particle tracking and vector plots	58
Figure VI.6 : Turbulence intensity distributions, predicted by <i>the MM k-ε model</i> for test Case I at various crank angles in contour plots	61
Figure VI.7 : Turbulence intensity distributions, predicted by <i>the k-ε-τ model</i> for test Case I at various crank angles in contour plots	64
Figure VI.8 :The comparison of measured and predicted profiles of axial mean velocity and turbulence intensity for axial location of $z=15$ mm at $CA=36^\circ$; test Case I.	67
Figure VI.9 :The comparison of measured and predicted profiles of axial mean velocity and turbulence intensity for axial location of $z=15$ mm at $CA=90^\circ$; test Case I.	68

Figure VI.10 : The comparison of measured and predicted profiles of axial mean velocity and turbulence intensity for axial location of $z=15$ mm at $CA=270^\circ$; test Case I.	69
Figure VI.11 : The comparison of measured and predicted profiles of axial mean velocity and turbulence intensity for axial location of $z=5, 10, 25$ and 41 mm at $CA=324^\circ$; test Case I.	70
Figure VI.12 : The comparison of measured and predicted profiles of axial mean velocity and turbulence intensity for axial location of $z=10$ and 32 mm at $CA=360^\circ$; test Case I.	71
Figure VI.13 : The comparison of measured and predicted profiles of axial mean velocity and turbulence intensity for axial location of $z=10, 20$ and 32 mm at $CA=380^\circ$; test Case I.	72
Figure VI.14 : Velocity field predictions of <i>the MM k-ϵ model</i> for test Case II at various crank angles in particle tracking and vector plots	73
Figure VI.15 : Velocity field predictions of <i>the k-ϵ-τ model</i> for test Case II at various crank angles in particle tracking and vector plots	76
Figure VI.16 : Turbulence intensity distributions, predicted by <i>the MM k-ϵ model</i> for test Case II at various crank angles in contour plots	79
Figure VI.17 : Turbulence intensity distributions, predicted by <i>the k-ϵ-τ model</i> for test Case II at various crank angles in contour plots	82
Figure VI.18 : The comparison of measured and predicted profiles of axial mean velocity and turbulence intensity for axial location of $z=10$ and 21 mm at $CA=324^\circ$; test Case II.	85
Figure VI.19 : The comparison of measured and predicted profiles of axial mean velocity and turbulence intensity for axial location of $z=5$ and 11 mm at $CA=360^\circ$; test Case II.	86
Figure VI.20 : The comparison of measured and predicted profiles of axial mean velocity and turbulence intensity for axial location of $z=5$ and 14 mm at $CA=380^\circ$; test Case II.	87
Figure C.1 : Preprocessing tool, developed by using Visual Basic programming language.	114

LIST OF TABLES

	<u>PAGE</u>
Table III.1 : Source terms for velocity components and enthalpy.	13
Table III.2 : Source terms for velocity components and enthalpy in cylindrical coordinates.	13
Table VI. 1 : Details of test cases; the Imperial College 2D engine simulator.	43
Table VI. 2 : Valve opening and closing and estimated temperatures of the engine simulator.	44
Table A. 1 : Definition and physical significance of some important turbulence scales in engine research	90

PART I

INTRODUCTION AND OBJECTIVES

I.1. INTRODUCTION

The modeling of engine processes continues to develop as basic understanding of the physics and chemistry of the phenomena of interest steadily expands and as the capability of computers to solve complex equations continues to increase.

The prediction of the details of the flow field within engines, and heat transfer and combustion processes that depend on those flow fields, by numerical solution of the governing conservation equations has become a realizable goal. Such methods have been under development for more than a decade, during which time they have steadily improved their ability to analyze the flow field in realistic engine geometries. However, they still do not have the capability to predict accurately all the features of real engine processes of interest.

This computational, fluid dynamic, engine process analysis codes solve the partial differential equations for conservation of mass, momentum, energy and species concentrations. To apply a computer to the solution of a continuum problem (such as the flow field inside the cylinder), the continuum must be represented by finite number of discrete elements. The most common method of discretization is to divide the region of interest into a number of small zones or cells. These cells form a grid or mesh which serves as a framework for constructing finite volume approximations to the governing partial differential equations. The time variable is similarly discretized into a sequence of small time intervals called time steps, and transient solutions is “marched out” in time: the solution at time t_{n+1} is calculated

from the known solution at time t_n . Three-dimensional formulations of the finite difference equations are required for most practical engine calculations; two-dimensional (or axisymmetric) formulations can be useful, however, under simpler flow situations, and have been more extensively used to date due to their simpler models, computer codes and requirement for less computer time and storage capacity.

The principal components of these multidimensional engine flow models contain the mathematical models, the discretization procedures, and solution algorithm. Mathematical models or equations are used to describe the flow processes. Especially turbulence model, describing the small-scale features of the flow, is important. Mathematically modeled partial differential equations are transformed into algebraic form by using the discretization procedures. Function of the solution algorithm is to solve the algebraic equations.

I.2. THE PROBLEM STAMENT

The most important feature of IC engine flows is the bulk compression/expansion process. There are a plenty of works on predicting the characteristics of in-cylinder flow in an IC engine. The most widely used turbulence model is the $k-\varepsilon$ model. However, it does not work well in modeling of compressed turbulence and some other types of flows discussed below. To better account for compression and expansion effects, Gul [1] extended a three-equation model, called $k-\varepsilon-\tau$ model, first suggested by Wu et al [2] and then applied it to a model engine test cases in order to evaluate its performance in real engine-like flows.

In this study, the new model developed by Gul is applied to model engine test cases for higher grid densities and different time steps to obtain better results. Modifications are made on computer program by partitioning program in subprograms and writing modules that includes common variables. Simulation program is rearranged for Fortran 90 standards.

A simple preprocessing interface is written in Visual Basic programming language to use computer code effectively (**Figure C.1**).

PART II

GENERAL BACKGROUND

II.1. INTRODUCTION

The flow in internal combustion engine cylinders is transient, due to the periodic motions of piston and valves, and is highly three-dimensional in space. The detailed analysis of an in-cylinder flow pattern and temperature distributions requires solution of the governing equations of conservation of mass, momentum and energy. These, however, are non-linear, coupled and too complex to allow analytical solutions; thus numerical solutions are obtained for discrete adjacent control volumes of finite dimensions overlaying the combustion chamber volume, by casting the governing differential equations into finite volume form and then solving latter.

To describe engine operating characteristics models, which describe the thermodynamic, fluid-flow, heat-transfer, and combustion phenomena that govern performance aspects of engines are developed. For the processes that govern engine performance two basic types of models have been developed. These can be categorized as thermodynamic and fluid dynamic in nature, depending on whether the equations which give the model its predominant structure based on energy conservation or on full analysis of the fluid motion. Other labels given to thermodynamic energy-conservation-based models are: zero-dimensional (since in the absence of any flow modeling, geometric features of the fluid motion cannot be predicted), and quasi-dimensional (where specific geometric features are added to the basic thermodynamic approach). Fluid-dynamic-based model are often called

multidimensional models due to their inherent ability to provide detailed geometric information on the flow field based on solution of the governing flow equations.

In this thesis, multi-dimensional approach with two-dimensional is presented. Hence, information about spatial and temporal distribution of flow characteristics can be provided. Two-dimensional axisymmetric flow is removed from three-dimensional flow in real engines; however, it has the advantage of providing accurate assessments of turbulence models to be made more easily and with more confidence. The two-dimensional flow keeps many of the features of engine flow. It is extensively documented by experiments, and allows one to use the realistic high grid densities required for turbulence model evaluation.

The nature of the flow varies markedly through an engine cycle. Thus Reynolds and Mach numbers have high values during inlet flow. The fluid pressure varies from around one bar during intake to perhaps 70 bars during combustion. Likewise, the fluid temperature may vary between 300 K and 2000 K. For most of the engine cycle the flow is definitely turbulent in nature, making analysis very much more difficult, than if it were laminar flow. These difficulties apply not only to numerical analysis but also to experimental investigations.

II.2. REVIEW OF RELATED LITERATURE

II.2.1. Computational Studies

There are two main types of computer models for engine flow and combustion referred as zero-dimensional and multi-dimensional. The former, which is outside the scope of this study, is thermodynamic in nature and does not provide information on spatial variation in cylinder. The multi-dimensional methods, on the other hand, usually have the following components:

- A set of partial differential conservation equations that govern the spatial and temporal variations of physical quantities, such as velocity, pressure, etc.
- Additional equations which represent the mathematical models of subprocesses, e.g. turbulence, spray, combustion etc.
- Numerical procedures for solving the above-mentioned equations over the computational mesh made up of discrete cells covering the whole combustion chamber.

Developments in numerical procedures are taking place mainly in the finite volume (FV) framework, although some recent work can be found on finite element (FE) methods applied to in-cylinder engine flow calculations (Brun et al. [3], Aita et al. [4]). In the FV area the two main centers of development have been the Los Alamos Scientific Laboratory, from which has emanated the well-known KIVA code (Butler et al [5]) embodying a semi-implicit method with a structured non-orthogonal mesh; and Imperial College, which has developed a series of fully-implicit FV methods. However, fully resolved 3-D unsteady accurate flow predictions including all the phenomena found in combustion chamber is still difficult to achieve without any prior experience or ‘tuning parameters’ involved. A general review on multi-dimensional methods in engine can be found, in Gosman [6].

Ahmadi-Befrui [7] simulated the mean flow and turbulence evolution in axisymmetric, disc chamber model engines operating at 200 rpm and compression ratios of 3.5 and 6.7. The investigations involved the assessment of the accuracy of predictions based on three variants of the $k-\varepsilon$ model, developed for the strongly compressible engine flows, namely, those of Watkins [8], Morel & Mansour [9] and El-Tahry [10]. He found that the turbulence models produce closely similar predictions of the mean flow and turbulence intensity and in general, good qualitative and moderate quantitative agreement with measurements was obtained. Moreover, the characteristics of the turbulence evolution were analysed with the aid of the volume-integral balances of the turbulence model transport equations and it was found that:

- The intake jet turbulence is in quasi-steady state and quasi-equilibrium.
- Over the cylinder volume, the turbulence is in quasi-equilibrium during the most of induction.
- The intake-generated mean flow and turbulence decay during compression, and turbulence relaxes into a structure predominantly controlled by the engine geometry at TDC of compression.
- Turbulence generation by intake-generated flow and that by compression contribute towards turbulence sustainment during compression.

Comparison of the behavior of the certain important turbulence parameters, namely the intensity, length scale and dissipation time scale, as predicted by the turbulence model variants, were also presented in order to identify the version that produces physically plausible and consistent variations of these parameters during

the engine cycle. It is concluded this basis that the Watkins [8] version is not suitable for engine applications but the Morel & Mansour[9] and El-Tahry [10] versions are both suitable, with the former one marginally preferable.

Jahanbakhsh [11] performed calculations for cylindrical bowl-in-piston chamber shapes among a number of other test cases pertaining to non-compressing and compressing model engines. Two alternative spatial differencing schemes were tested: one is conventional five-point hybrid central-upwind scheme and the other is nine-point bounded scew hybrid differencing (BSHD) scheme. The results indicated the superiority of the BSHD scheme over the five-point scheme in the flow predictions for the cases considered. It was found that introduction of a piston with a cylindrical bowl, in the absence of swirl, has a negligible effect on the mean and turbulence characteristics of the flow through the induction stroke. The relative performance of the Watkins and El-Tahry versions of the $k-\varepsilon$ model were assessed for the case of re-entrant piston-bowl configuration and it was found that the predictions for the two models were somewhat similar. The Watkins model gives slightly weaker mean flow and larger turbulence intensities during compression stroke. Although the El-Tahry version produces slightly better agreement compared with the experimental data, its estimation of turbulence is less accurate.

Shah and Markatos [12] performed 2D and 3D computations of the in-cylinder turbulent flow with the Watkins and Morel & Mansour version of the $k-\varepsilon$ model as well as the $k-w$ model of Wilcox so as to remove the need to modify one of the model constants in near wall flows. They concluded that the predictions with the Morel & Mansour model appear encouraging for swirl flows for both 2D and 3D cases. It was also suggested that the $k-w$ model might be a better choice for IC engine simulations, and that a similar modification to its standard form may improve the swirl predictions even further, as was the case with the $k-\varepsilon$ model.

II.2.2. Turbulence Modeling Aspects

In multi-dimensional engine studies, turbulence is generally treated by computing the ensemble-averaged motion using the $k-\varepsilon$ turbulence model although the DSM model is now emerging in engine applications. However, the latter requires solution of the seven PDEs (six stresses and one for ε) compared to two (k and ε) in the former. More information can be found in Launder [13].

A number of attempts have been made at deriving a suitable formulation of the k - ε model for the strongly compressible engine flows, namely, by Watkins [8], Reynolds [14], El-Tahry [10], Morel & Mansour [9]. These alternative forms differed from each other mainly in the coefficient of a term S_ε that accounts for the effects of compressibility on the dissipation rate of turbulence kinetic energy.

$$S_\varepsilon = C_{\varepsilon 3} \rho \varepsilon \nabla \cdot \mathbf{u} \quad (\text{II.1})$$

The model used by Watkins[8] employs $C_{\varepsilon 3} = 1.0$. Reynolds [14] accounted for the compression-dilatation effects by considering rapid spherical compression of homogeneous isotropic turbulence and obtained $C_{\varepsilon 3} = -2/3$. This term was then readjusted to yield $C_{\varepsilon 3} = -0.373$ by Ahmadi-Befrui et al. [15]. Morel & Mansour [9] extended Reynolds' analysis to more general types of compression that yielded different values for the coefficients of the ε -equation for each type. Models with $C_{\varepsilon 3} > 0$ can result in length scales larger than distance between the piston and the cylinder head during compression, which clearly unrealistic. As mentioned earlier here, Ahmadi-Befrui [7] compared the performances of some of the above mentioned variants of the k - ε model and found that the Morel & Mansour model is the most suitable one for in-cylinder bowl applications although it performed with moderate success in mean flow and turbulence predictions. Ahmadi-Befrui et al. [15] also showed that the ε -equation with $C_{\varepsilon 3} = 1.0$ results in longer length and dissipation time-scales than $C_{\varepsilon 3} = 0$ and $C_{\varepsilon 3} = -0.373$ in reciprocating engines under motored and firing conditions.

Coleman & Mansour [16] have also proposed a modification to the k - ε model based on direct numerical simulation (DNS) of rapid spherical compression, which takes into account variable viscosity effects, again thorough the coefficient $C_{\varepsilon 3}$. However, this does not necessarily mean that it would provide better predictions in low rapidity ratio cases as found in IC engines.

There have been an increasing number of proposals in recent years which employ more than one time-scale of turbulence in order to overcome some of the deficiencies of a single transport equation for the length scale used in the k - ε or differential stress models.

PART III

MATHEMATICAL MODEL

III.1. INTRODUCTION

III.1.1. The General Governing Equations

The fundamental equations that govern the in-cylinder flow processes, like any other compressible, non-reacting flow, are the Navier-Stokes equations for conservation of momentum, continuity equation for the conservation of mass and the stagnation enthalpy or specific internal energy equation for the conservation of energy, together with an equation of state of the gas relating local values of density, pressure and temperature. In the case of reacting flows, additional equations are required for the concentrations of chemical species and the reaction rates. All the following equations are time dependent and written in Cartesian tensor notation.

1. The continuity equation:

$$\frac{\partial \rho}{\partial t} + \frac{\partial}{\partial x_j} (\rho U_j) = 0 \quad (\text{III.1})$$

2. Navier-Stokes Equations:

$$\frac{\partial}{\partial t} (\rho U_i) + \frac{\partial}{\partial x_j} (\rho U_j U_i) = -\frac{\partial P}{\partial x_i} + \frac{\partial}{\partial x_j} \sigma_{ij} \quad (\text{III.2})$$

where ρ , U , P and σ_{ij} are, respectively, the density, velocity, static pressure and viscous stress tensor σ_{ij} is defined

$$\sigma_{ij} = \mu \left(\frac{\partial U_i}{\partial x_j} + \frac{\partial U_j}{\partial x_i} \right) - \frac{2}{3} \mu \frac{\partial U_l}{\partial x_l} \delta_{ij} \quad (\text{III.3})$$

for a Newtonian fluid where μ is the fluid's molecular viscosity, and δ_{ij} is the 'Kronecker delta' which is unity if $i = j$ and zero if $i \neq j$.

3. Equation for the stagnation enthalpy:

The stagnation enthalpy is defined by the sum of internal, kinetic and potential energies,

$$h_s = e + \frac{U_i U_i}{2} + \frac{P}{\rho} \quad (\text{III.4})$$

And it relates to the absolute temperature, T, by;

$$h_s = C_p T + \frac{U_i U_i}{2} \quad (\text{III.5})$$

where C_p is the specific heat under constant pressure. The governing equation is then

$$\begin{aligned} \frac{\partial}{\partial t}(\rho h_s) + \frac{\partial}{\partial x_j}(\rho U_j h_s) = & \frac{\partial P}{\partial t} + \frac{\partial}{\partial x_j} \left(\frac{\mu}{\sigma_h} \frac{\partial h_s}{\partial x_j} \right) \\ & + \frac{\partial}{\partial x_j} \left[\mu \left(1 - \frac{1}{\sigma_h} \right) \frac{\partial}{\partial x_j} \left(\frac{U_i U_i}{2} \right) \right] \\ & + \frac{\partial}{\partial x_j} \left(\mu U_i \frac{\partial U_j}{\partial x_j} \right) - \frac{2}{3} \frac{\partial}{\partial x_j} \left(\mu U_j \frac{\partial U_i}{\partial x_i} \right) \end{aligned} \quad (\text{III.6})$$

where σ_h is the Prandtl number. The last three terms on the right hand side of equation represent the viscous transformation of the mechanical energy into heat and are negligibly small in the present circumstances [7].

The equation of state of the fluid which links temperature, density and pressure is normally algebraic in form and here, although it is not essential to the analysis, perfect gas relationship is used.

$$P = \rho R T \quad (\text{III.7})$$

where R is the gas constant.

All the transport equations given above and those for other scalar quantities, such as species concentrations, process the following similar form:

$$\frac{\partial}{\partial t}(\rho \phi) + \frac{\partial}{\partial x_j}(\rho U_j \phi) = \frac{\partial}{\partial x_j} \left(\Gamma_\phi \frac{\partial \phi}{\partial x_j} \right) + S_\phi \quad (\text{III.8})$$

where ϕ represents an arbitrary scalar quantity, Γ_ϕ for diffusion coefficient and S_ϕ for sources.

III.1.2. Ensemble-Averaged Equations

The ensemble average is defined as the statistical average value of a property at a given point over a large number of cycles. This averaging scheme is based on decomposing the instantaneous velocity $U(\Theta, i)$ at crank angle Θ in the i^{th} engine cycle as:

$$U(\Theta, i) = \bar{U}_e(\Theta) + u_e(\Theta, i) \quad (\text{III.8})$$

where the ensemble-averaged velocity $\bar{U}_e(\Theta)$ is defined as:

$$\bar{U}_e(\Theta) = \lim_{n \rightarrow \infty} \left[\frac{1}{n} \sum_{i=1}^n U(\Theta, i) \right] \quad (\text{III.9})$$

in which n is the number of cycles. The fluctuating component can be expressed in terms of root-mean-square (rms) value of $u_e(\Theta, i)$ or in other words absolute intensity of turbulence:

$$\sqrt{\bar{u}_e^2(\Theta)} = \lim_{n \rightarrow \infty} \left[\frac{1}{n} \sum_{i=1}^n (U(\Theta, i) - \bar{U}_e(\Theta))^2 \right]^{\frac{1}{2}} \quad (\text{III.10})$$

The replacement of the instantaneous quantities in **Equations III.1,2 and 6** by a mean and fluctuating component

$$\begin{aligned} \rho &= \bar{\rho} + \rho' \\ U_i &= \bar{U}_i + u_i \end{aligned} \quad (\text{III.11})$$

And ensemble averaging the result produces the following:

1. The continuity equation:

$$\frac{\partial}{\partial t} (\bar{\rho}) + \frac{\partial}{\partial x_j} (\bar{\rho} \bar{U}_j + \overline{\rho' u_j}) = 0 \quad (\text{III.12})$$

2. Conservation of momentum:

$$\begin{aligned} \frac{\partial}{\partial t} (\bar{\rho} \bar{U}_i + \overline{\rho' u_i}) + \frac{\partial}{\partial x_j} (\bar{\rho} \bar{U}_j \bar{U}_i + \overline{\rho u_i u_j} + \bar{U}_j \overline{\rho' u_i} + \bar{U}_i \overline{\rho' u_j}) \\ = -\frac{\partial \bar{P}}{\partial x_i} + \frac{\partial}{\partial x_j} \bar{\sigma}_{ij} \end{aligned} \quad (\text{III.13})$$

3. Transport equations for scalar ϕ :

$$\begin{aligned} & \frac{\partial}{\partial t} (\bar{\rho}\bar{\phi} + \overline{\rho'\phi'}) \\ + \frac{\partial}{\partial x_j} (\bar{\rho}\bar{U}_j\bar{\phi} + \overline{\rho u_j\phi'} + \bar{U}_j\overline{\rho'\phi'} + \overline{\phi\rho'u_j} + \overline{\rho'u_j\phi'}) \\ & = \frac{\partial}{\partial x_j} \left(\Gamma_\phi \frac{\partial \bar{\phi}}{\partial x_j} \right) + \bar{S}_\phi \end{aligned} \quad (\text{III.14})$$

where \bar{S}_ϕ is the ensemble-averaged source term. Here turbulent fluctuations in density, ρ' are regarded as negligible compared to $\bar{\rho}$, in several studies [8] and correlations containing ρ' are ignored.

An alternative, advocated for compressible reacting and non-reacting flows is to work with density-weighted ensemble-averaged properties (DWEA), which is proposed by Favre [17]. It has been shown that resulting equations are similar in form to the unweighted-averaged equations with the terms containing ρ' omitted. In this approach, instantaneous variable ϕ is decomposed into its DWEA value $\bar{\phi}$, and fluctuations ϕ^* about this as:

$$\phi = \bar{\phi} + \phi^* \quad (\text{III.15})$$

$\bar{\phi}$ is defined as:

$$\bar{\phi} = \frac{1}{\bar{\rho}(\Theta)} \left[\lim_{n \rightarrow \infty} \frac{1}{n} \sum_{i=1}^n \rho(\Theta, i) \phi(\Theta, i) \right] \quad (\text{III.16})$$

where $\bar{\rho}$ is the ensemble-averaged density, Θ is the crank angle of interest and i is the number of engine cycles.

Governing conservation equations can be written with applying DWEA approach as:

1. The continuity equation:

$$\frac{\partial}{\partial t} (\bar{\rho}) + \frac{\partial}{\partial x_j} (\bar{\rho}\bar{U}_j) = 0 \quad (\text{III.17})$$

2. Conservation of momentum:

$$\frac{\partial}{\partial t} (\bar{\rho}\bar{U}_i) + \frac{\partial}{\partial x_j} (\bar{\rho}\bar{U}_j\bar{U}_i + \overline{\rho u_j^* u_i^*}) = -\frac{\partial \bar{P}}{\partial x_i} + \frac{\partial}{\partial x_j} \bar{\sigma}_{ij} \quad (\text{III.18})$$

3. Transport equations for scalar ϕ :

$$\frac{\partial}{\partial t} (\overline{\rho\phi} + \overline{\rho'\phi'}) + \frac{\partial}{\partial x_j} (\overline{\rho U_j\phi} + \overline{\rho u_j^*\phi^*}) = \frac{\partial}{\partial x_j} \left(\Gamma_\phi \frac{\partial \overline{\phi}}{\partial x_j} \right) + \overline{S}_\phi \quad (\text{III.19})$$

and the averaged form of the perfect gas relationship is;

$$\overline{P} = \overline{\rho} R \overline{T} \quad (\text{III.20})$$

Here one overbar represents an unweighted ensemble-averaged and double overbar represents density-weighted ensemble-averaged quantities. More details can be found in [1].

The foregoing conservation equations of momentum and energy and the transport equations for turbulent parameters, which will be discussed later, are all in similar form and can be expressed by a single general equation:

$$\frac{\partial}{\partial t} (\overline{\rho\phi}) + \frac{\partial}{\partial x_j} (\overline{\rho U_j\phi}) = \frac{\partial}{\partial x_j} \left(\Gamma_\phi \frac{\partial \overline{\phi}}{\partial x_j} \right) + \overline{S}_\phi \quad (\text{III.21})$$

where dependent variable ϕ stands for any of U , V , W , h_s , k , ε or l (for continuity equation) the diffusion coefficient Γ_ϕ and the source term S_ϕ for individual variables are given in **Table III.1**. For three-dimensional flows, **Equation III.21** will be reexpressed in cylindrical-polar coordinate system (r, θ, z) with the corresponding velocity vector $(V_r, V_\theta, V_z)^T$ as:

$$\begin{aligned} \frac{\partial}{\partial t} (\rho\phi) + \frac{\partial}{\partial z} (\rho V_z\phi) + \frac{1}{r} \frac{\partial}{\partial r} (\rho r V_r\phi) + \frac{1}{r} \frac{\partial}{\partial \theta} (\rho V_\theta\phi) = \\ \frac{\partial}{\partial z} \left(\Gamma_\phi \frac{\partial \phi}{\partial z} \right) + \frac{1}{r} \frac{\partial}{\partial r} \left(r \Gamma_\phi \frac{\partial \phi}{\partial r} \right) + \frac{1}{r} \frac{\partial}{\partial \theta} \left(\frac{\Gamma_\phi}{r} \frac{\partial \phi}{\partial \theta} \right) + S_\phi(r, \theta, z) \end{aligned} \quad (\text{III.22})$$

where the overbars are omitted for convenience. This coordinate frame is more suitable to analyse the flow in the axisymmetric model of the piston-cylinder assemblies in which $\partial/\partial\theta = 0$. In this case the general transport **Equation III.22** reduces to

$$\begin{aligned} \frac{\partial}{\partial t} (\rho\phi) + \frac{\partial}{\partial z} (\rho V_z\phi) + \frac{1}{r} \frac{\partial}{\partial r} (\rho r V_r\phi) = \\ \frac{\partial}{\partial z} \left(\Gamma_\phi \frac{\partial \phi}{\partial z} \right) + \frac{1}{r} \frac{\partial}{\partial r} \left(r \Gamma_\phi \frac{\partial \phi}{\partial r} \right) + S_\phi(r, \theta, z) \end{aligned} \quad (\text{III.23})$$

and the continuity equation also reduces to

$$\frac{\partial}{\partial t}(\rho) + \frac{\partial}{\partial z}(\rho V_z) + \frac{1}{r} \frac{\partial}{\partial r}(\rho r V_r) = 0 \quad (\text{III.24})$$

The expression of the diffusion coefficient Γ_ϕ and the source term S_ϕ in the above equations, corresponding to the individual variables is given in **Table III.2**.

Table III.1 Source terms for velocity components and enthalpy.

ϕ	Γ_ϕ	S_ϕ
U_i	μ_t	$-\frac{\partial P}{\partial x_j} + \frac{\partial}{\partial x_j} \left(\mu_t \frac{\partial U_i}{\partial x_i} \right) - \frac{2}{3} \frac{\partial}{\partial x_i} \left(\mu_t \frac{\partial U_i}{\partial x_i} + \rho k \right)$
h	$\frac{\mu_t}{\sigma_h}$	$\frac{\partial P}{\partial t}$

Table III.2 Source terms for velocity components and enthalpy in cylindrical coordinates.

ϕ	Γ_ϕ	$S_\phi(r, z)$
V_z	μ_t	$-\frac{\partial P}{\partial z} + \frac{\partial}{\partial z} \left(\mu_t \frac{\partial V_z}{\partial z} \right) + \frac{1}{r} \frac{\partial}{\partial r} \left(r \mu_t \frac{\partial V_r}{\partial z} \right) - \frac{2}{3} \frac{\partial}{\partial z} \left(\mu_t \nabla U + \rho k \right)$
V_r	μ_t	$-\frac{\partial P}{\partial r} + \frac{\partial}{\partial z} \left(\mu_t \frac{\partial V_z}{\partial r} \right) + \frac{1}{r} \frac{\partial}{\partial r} \left(r \mu_t \frac{\partial V_r}{\partial r} \right) + \frac{\rho V_\theta^2}{r} - 2 \mu_t \frac{V_r}{r^2}$ $-\frac{2}{3} \frac{\partial}{\partial r} \left(\mu_t \nabla U + \rho k \right)$
V_θ	μ_t	$-\rho \frac{V_r V_\theta}{r} - \mu_t \frac{V_\theta}{r^2} - \frac{V_\theta}{r} \frac{\partial \mu_t}{\partial r}$
h_s	$\frac{\mu_t}{\sigma_h}$	$\frac{\partial P}{\partial t}$
<p>Here $\nabla U = \frac{\partial V_z}{\partial z} + \frac{1}{r} \frac{\partial}{\partial r} (r V_r)$ and $U = \begin{pmatrix} V_r \\ V_\theta \\ V_z \end{pmatrix}$</p>		

III.1.3. Boundary Conditions

The complete description of a particular engine in mathematical terms requires statements of the starting conditions within the combustion chamber and the

conditions applying at its boundaries. The former are only of influence during the transient (start-up) period and have no influence on cyclically repeating behavior that characterizes the steady operating state. The boundary conditions are, however, always influential and need to be specified at all confining walls and the planes of the inlet and exhaust apertures.

III.1.3.1. Walls, Stagnation Enthalpy, Symmetry Axis

The no-slip condition applies to boundary values at all wall surfaces; all velocity components are zero except the axial velocity on the piston surface, which is set equal to the instantaneous piston velocity.

The boundary conditions for the enthalpy equation can be supplied by specifying the local temperature or heat flux (proportional to the normal gradient in temperature) at each point on the wall. The temperature, however, oscillates during the engine cycle due to variations in the gas temperature and thermal conductance. Fortunately, these oscillations are strongly damped by the thermal inertia of the cylinder [1] and are usually small compared with the gas to wall temperature difference. Thus, insofar as the cylinder processes are concerned, the wall temperature can be regarded as being steady.

The boundary conditions at the symmetry axis are given by $\partial\phi/\partial r = 0$. It means gradients of all dependent variables in the radial direction are equal to zero, except the radial and swirl velocities, which are themselves zero.

III.1.3.2. Boundary Conditions At Planes Of Inlet And Exhaust Apertures

In engine circumstances the velocities through the inlet and exhaust apertures are unknown, but the manifold pressures are usually known or independently calculable. Therefore, in order to determine the magnitudes of the velocities at the apertures, the relation between mass flow rate through the orifice/valve and pressure drop across it must be defined. The equations employed here are typical of those used in engine cycle calculations [8, 18] and are as follows:

i. For subsonic flow, with $P_d / P_u > (2/\gamma+1)^{\gamma/(\gamma-1)}$ mass flow rate is:

$$\dot{m} = C_D A_M \rho_u \sqrt{\gamma R_g T_u} \sqrt{\frac{2}{\gamma-1} \left(\frac{P_d}{P_u}\right)^{\frac{2}{\gamma}} \left[1 - \left(\frac{P_d}{P_u}\right)^{\frac{\gamma-1}{\gamma}}\right]} \quad (\text{III.25})$$

ii. For sonic flow, with $P_d / P_u \leq (2/\gamma+1)^{\gamma/(\gamma-1)}$ mass flow rate is:

$$\dot{m} = C_D A_M \rho_u \sqrt{\gamma R_g T_u} \sqrt{\left(\frac{2}{\gamma-1}\right)^{\frac{\gamma+1}{\gamma-1}}} \quad (\text{III.26})$$

where A_M is the minimum area of the valve throat, γ is the ratio of specific heats, C_D is discharge coefficient (details can be found in [1]) and R_g is the gas constant. The subscripts u and d denote upstream and downstream values respectively. (during intake u represents manifold values whereas d represents cylinder values.)

Boundary conditions for turbulence parameters will be given in the next chapter.

III.1.4. Equations For Moving Coordinate Frames

Due to the piston and inlet valve motion, solution domain changes continuously in time. One can either use a computational grid, which is fixed, in (r, z) space and completely cover the solution domain only when piston is at BDC, or alternatively a more flexible coordinate frame that expands and contracts between cylinder head and piston top can be employed. The first method suffers from problems of resolution and is also quite inefficient with respect to computer storage and time. The latter approach first devised by Watkins [8], and later modified by other researchers such as Johns [19], Jahanbakhsh [11], require a transformation resulting in Eularian-Langrangian method (to cause the grid to move with the mean flow), although proved powerful in solving free surface problems, has the disadvantage of severe mesh distortion in recirculating flow.

The hybrid of Eularian-Langrangian schemes is achieved by a transformation, which replaces the coordinate frame (r, z, t) with the frame (r, ξ, t) , in the form of $\xi = F(z, t)$ which is dependent on the chamber geometry. In general, solution domain is divided into two distinct regions within the expanding-contracting domain, as shown in **Figure III.1** and **Figure III.2**. Namely,

Region 1 : confined between the cylinder head and valve face, that contracts and expands with the valve movement. In this region axial coordinate ξ and the grid velocity U_G are defined as:

$$\begin{aligned}\xi &= \frac{z}{z_v(t)} && \text{for } 0 \leq z \leq z_v(t) \\ U_G &= \xi \frac{dz_v(t)}{dt} && \text{for } 0 \leq z \leq z_v(t)\end{aligned}\tag{III.27}$$

where $z_v(t)$ is the instantaneous position of the valve face (i.e. valve lift).

Region 2: is bounded between the valve face and the piston top $z_p(t)$, which also stretches in accordance with the relative motion between these two. ξ and the grid velocity U_G are defined as:

$$\begin{aligned}\xi &= \frac{z - z_v(t)}{z_p(t) - z_v(t)} && \text{for } z_v(t) \leq z \leq z_p(t) \\ U_G &= (1 - \xi) \frac{dz_v(t)}{dt} + \xi \frac{dz_p(t)}{dt} && \text{for } z_v(t) \leq z \leq z_p(t)\end{aligned}\tag{III.28}$$

The transformed general transport equation is derived by obtaining the transformation formulae for derivatives $\partial/\partial r$, $\partial/\partial z$, $\partial/\partial t$ between the two coordinate systems. So, a variable ϕ can be expressed in both coordinate systems as

$\phi(z, r, t) = \phi'(\xi, r, t)$. Application of relations to the general transport equation in the (z, r, t) coordinates renders

$$\begin{aligned}\frac{1}{z_p} \frac{\partial}{\partial t} (\rho z_p \phi) + \frac{1}{z_p} \frac{\partial}{\partial \xi} (\rho U \phi) + \frac{1}{r} \frac{\partial}{\partial r} (\rho r V_r \phi) = \\ \frac{1}{z_p} \frac{\partial}{\partial \xi} \left(\frac{\Gamma_\phi}{z_p} \frac{\partial \phi}{\partial \xi} \right) + \frac{1}{r} \frac{\partial}{\partial r} \left(r \Gamma_\phi \frac{\partial \phi}{\partial r} \right) + S_\phi(\xi, r)\end{aligned}\tag{III.29}$$

in which U is the local relative axial velocity between the fluid and the coordinate frame $U = V_z - U_G$. The expressions for $S_\phi(\xi, r)$ corresponding to the individual variables U , V , W , h_s and turbulence parameters ($\phi=1$ for continuity equation) are given in [1].

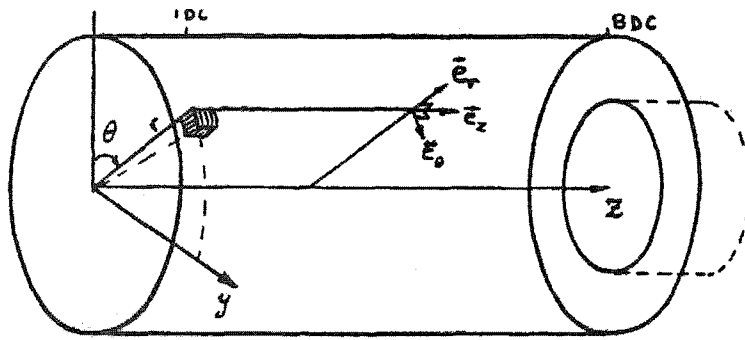


Figure III. 1 System configuration and coordinate frame.

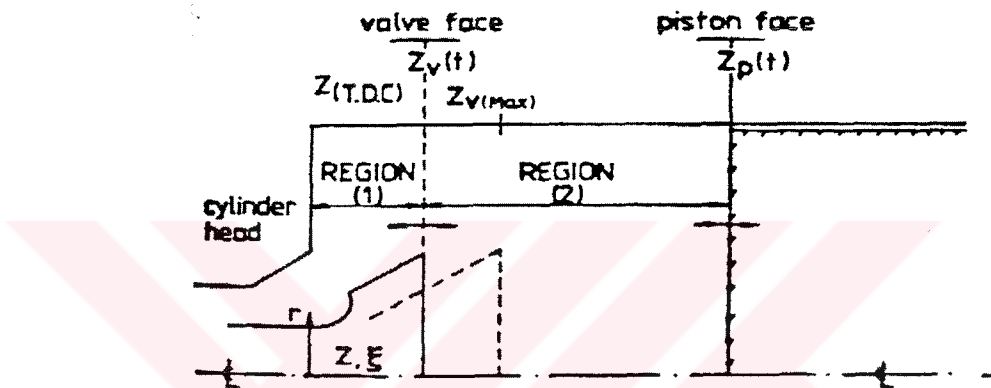


Figure III. 2 System configuration within moving coordinate frame

PART IV

TURBULENCE MODEL

IV.1. WHAT IS TURBULENCE

The Reynolds number of a flow gives a measure of the relative importance of inertia forces and viscous forces. In experiments on fluid systems it is observed that at values below the critical Reynolds number Re_{crit} the flow is smooth and adjacent layers of fluid slide past each other in an orderly fashion. If the applied boundary conditions do not change with the time the flow is steady. This regime is called **laminar** flow.

At values of the Reynolds number above Re_{crit} a complicated series of events takes place that eventually leads to a radical change of the flow character. In the final state the flow behavior is random and chaotic. The motion becomes unsteady even with constant imposed boundary conditions. The velocity and all other flow properties vary in a random and chaotic way. This regime is called **turbulent** flow.

The random nature of a turbulent flow precludes computations based on a complete description of the motion of all the fluid particles. A turbulent flow is characterized by mean values of flow properties (U, V, W, P etc.) and the statistical properties of their fluctuations (u', v', w', p' etc) as discussed in the previous section. Even in flows where the mean velocities and pressures vary in only one or two dimensions in space, turbulent fluctuations always have a three-dimensional spatial character. Turbulent flow structure includes rotational flows; called turbulent eddies, with a range of length scales. Particles of fluid that are initially separated by a long distance can be brought close together by eddying motions in turbulent flows. As a

consequence, heat, mass and momentum are effectively exchanged. The largest turbulent eddies interact with and extract energy from the mean flow by process called **vortex stretching**. The presence of mean velocity gradients in sheared flows distorts the rotational turbulent eddies. Suitably aligned eddies are stretched since one end is forced to move faster than the other.

The characteristic velocity scale \mathcal{S} (m/s) and length scale ℓ (m) of the larger eddies are of the same order as the velocity scale U and length scale L of the mean flow. These large eddies are dominated by inertia effects and viscous effects are negligible. The large eddies are effectively inviscid and angular momentum is conserved during vortex stretching. This causes the rotation rate to increase and the radius of their cross-sections to decrease. Thus the process creates motions at smaller transverse length scales and also at smaller time scales. The stretching work done by the mean flow on the large eddies provides the energy which maintains the turbulence. Smaller eddies are themselves stretched strongly by larger eddies and more weakly by the mean flow. By the way, the kinetic energy is transported from larger eddies to smaller ones.

The structure of largest eddies is highly anisotropic and flow dependent due to their strong interaction with the mean flow. The diffusive action of viscosity tends to smear out directionality at small scales. At high mean flow Reynolds numbers the smallest eddies in a turbulent flow are, therefore, isotropic.

IV.2. Turbulence Models

A turbulence model is a computational procedure to close the system of mean flow equations (continuity and other equations) so that a more or less wide variety of flow problems can be calculated.

In the previous section, additional terms are obtained due to the fluctuating parts of mean flow. These terms contain correlations interpreted as diffusional fluxes of momentum and energy due to turbulence. The objective of turbulence modeling is to express these correlations in terms of mean flow variables and characteristic turbulence properties. There are a number of turbulence models used to solve CFD problems. Namely, zero-equation model (mixing length model), the k - ε turbulence model, Algebraic Stress Model (ASM), Differential Stress Model (DSM) and some others...

Of the classical models the mixing length model and the $k-\varepsilon$ model are presently by far the most widely used. They are based on the presumption that there exists an analogy between the action of the viscous stresses and Reynolds stresses on the mean flow. Both stresses appear on the right hand side of the momentum equation and in Newton's law of viscosity the viscous stresses are taken to be proportional to the rate of deformation of fluid elements. This can be written for an incompressible fluid as:

$$\tau_{ij} = \mu \left(\frac{\partial U_i}{\partial x_j} + \frac{\partial U_j}{\partial x_i} \right) \quad (\text{IV.1})$$

It is experimentally observed that turbulence decays unless there is shear in isothermal incompressible flows. Furthermore, turbulent stresses are found to increase as the mean rate of deformation increases (Boussinesq). It gives

$$\tau_{ij} = \overline{-\rho u_i^* u_j^*} = \mu_t \left(\frac{\partial U_i}{\partial x_j} + \frac{\partial U_j}{\partial x_i} \right) \quad (\text{IV.2})$$

Turbulent transport of heat, mass and other scalar properties is modeled similarly. **Equation IV.2** shows that turbulent momentum transport is assumed to be proportional to the mean gradients of velocity. By analogy, turbulent transport of a scalar is taken to the gradient of the mean value of transported quantity. It can be represented for any scalar quantities as:

$$\overline{-\rho u_i^* \phi_j^*} = \Gamma_t \frac{\partial \phi}{\partial x_j} \quad (\text{IV.3})$$

where Γ_t is the turbulent diffusivity.

Since turbulent transport of momentum and heat is due to the same mechanism, it can be expected that the value of the turbulent diffusivity Γ_t be close to that of turbulent viscosity μ_t . A turbulent Prandtl/Schmidt number is defined as:

$$\sigma_t = \frac{\mu_t}{\Gamma_t} \quad (\text{IV.4})$$

Most CFD works assume this to be the case and use values of σ_t around 1.

IV.2.1. Mixing Length Model

This model attempts to describe the stresses by means of simple algebraic formulae for μ_t as a function of position. Kinematic turbulent viscosity has dimensions of m^2/s and can be expressed as a product of a turbulent velocity scale \mathcal{G} (m/s) and length scale ℓ (m) in one-dimension. This relation can be formulated as:

$$\nu_t = C \mathcal{G} \ell \quad (\text{IV.5})$$

where C is a dimensionless constant. and dynamic viscosity is:

$$\mu_t = C \rho \mathcal{G} \ell \quad (\text{IV.6})$$

most of the kinetic energy of turbulence is contained in the largest eddies and the turbulent length scale ℓ is therefore the characteristic of these eddies which interact with the mean flow. So, in two dimensions the only significant Reynolds stress is $\tau_{xy} = \tau_{yx} = -\overline{\rho u_i^* u_j^*}$ and the only significant mean velocity gradient is $\partial U / \partial y$. And the velocity scale can be rewritten as:

$$\mathcal{G} = c \ell \left| \frac{\partial U}{\partial y} \right| \quad (\text{IV.7})$$

where c is also a dimensionless constant. Combining **Equations IV.5** and **IV.7** and absorbing constants C and c into a new length scale ℓ_m , kinematic viscosity is:

$$\nu_t = \ell_m^2 \left| \frac{\partial U}{\partial y} \right| \quad (\text{IV.8})$$

this is **Prandtl's mixing length model**. Reynolds stresses can be described as:

$$\tau_{xy} = \tau_{yx} = -\overline{\rho u_i^* u_j^*} = \rho \ell_m^2 \left| \frac{\partial U}{\partial y} \right| \frac{\partial U}{\partial y} \quad (\text{IV.9})$$

turbulence is a function of the flow and if the turbulence changes it is necessary to account for this within the mixing length model by varying ℓ_m .

The mixing length model can also be used to predict turbulent transport of scalar quantities. The only turbulent transport term which matters in the two-dimensional flows for which the mixing length is useful is modeled as follows:

$$-\overline{\rho u_i^* \phi^*} = \Gamma_t \frac{\partial \phi}{\partial y} \quad (\text{IV.10})$$

where $\Gamma_t = \mu_t / \sigma_t$ and v_t is found from equation (IV.8). Rodi[20] recommends values for σ_t as 0.9 in near wall flows, 0.5 for jets and mixing layers and 0.7 in axisymmetric jets.

Mixing length model is easy to implement, cheap in terms of computing resources and has good predictions for thin shear flows and boundary layers. However, it is completely incapable of describing flows with separation and recirculation and only calculates mean flow properties and turbulent shear stress.

IV.2.2. The k - ε model

The influence of the turbulence on the mean flow can be expressed by means of mixing length model if the convection and diffusion of turbulence properties is neglected. As in the case of recirculating flows these properties cannot be neglected so, mixing length model is no longer feasible.

The k - ε model was first developed by Jones and Launder [21] to predict turbulence dynamics. This two-equation model focuses on the mechanisms that affect the turbulent kinetic energy. It is the most widely validated turbulence model, however, it has poor performance in a variety of cases such as swirling flows, rotating flows and some others [22]. In this model two extra partial differential equations are solved for turbulence kinetic energy k and its dissipation rate ε . Turbulence viscosity is given by:

$$\mu_t = C_\mu \rho k^2 / \varepsilon \quad (\text{IV.11})$$

where C_μ is an empirical coefficient and taken as $C_\mu = 0.09$, determined from the experiments in thin shear layer flows.

The instantaneous kinetic energy $k(t)$ of a turbulent flow is the sum of the mean K and turbulent k kinetic energies.

$$K = \frac{1}{2}(U^2 + V^2 + W^2) \quad \text{and} \quad k = \frac{1}{2}(\overline{u^2} + \overline{v^2} + \overline{w^2}) \quad k(t) = K + k \quad (\text{IV.12})$$

IV.2.2.1 The k-equation

Transport equations of turbulent kinetic energy for density weighted ensemble average quantities can be obtained by subtracting the average momentum **Equation III.18** from its instantaneous counterpart **Equation III.2**, then multiplying the resultant equation for the fluctuating component u_i^* by u_i^* and averaging as in the case of constant density flows [7].

The result is:

$$\frac{\partial}{\partial t}(\overline{\rho k}) + \frac{\partial}{\partial x_j}(\overline{\rho U_j k}) = d_k + P_k - \overline{\rho \varepsilon} - \overline{u_i^* \frac{\partial P}{\partial x_i}} + \overline{p \frac{\partial u_i^*}{\partial x_i}} \quad (\text{IV.13})$$

(I) (II) (III) (IV) (V) (VI)

Except for the last two terms at the right hand side of the above equation, it is similar to its counterpart for incompressible flow. The terms in the rhs of the equation cannot be calculated as presented and require modeling within the eddy viscosity framework [23]. The meanings of terms in the above equation can be summarized as:

- I. Left hand side of equation represents the rate of change and transport of turbulence kinetic energy by convection.
- II. d_k is the diffusion term and includes three components, which are transport of turbulence kinetic energy by pressure fluctuations, viscous and Reynolds stresses.

$$d_k = -\frac{\partial}{\partial x_j}(\overline{p u_j^*}) + \frac{\partial}{\partial x_j}(\overline{u_i^* \sigma_{ij}^*}) - \frac{1}{2} \frac{\partial}{\partial x_j}(\overline{\rho u_j^* u_i^* u_i^*}) \quad (\text{IV.14})$$

it is modeled by gradient diffusion hypothesis and habitually taken as [8,23]:

$$d_k = \frac{\partial}{\partial x_j} \left(\frac{\mu_t}{\sigma_k} \frac{\partial k}{\partial x_j} \right) \quad (\text{IV.15})$$

in eddy viscosity modeling framework where σ_k is the turbulence Prandtl number.

- III. P_k represents production of turbulent kinetic energy due to interaction of the Reynolds stresses with the mean flow gradients. This term gives a positive contribution in the equation.

$$P_k = -\overline{\rho u_i^* u_j^* \frac{\partial U_i}{\partial x_j}} \quad (\text{IV.16})$$

this term is modeled by using Boussinesq constitutive relation as:

$$P_k = \mu_t \left(\frac{\overline{\partial U_i}}{\partial x_j} + \frac{\overline{\partial U_j}}{\partial x_i} \right) \frac{\overline{\partial U_i}}{\partial x_j} - \frac{2}{3} \left(\mu_t \frac{\overline{\partial U_l}}{\partial x_l} + \overline{\rho} k \right) \frac{\overline{\partial U_l}}{\partial x_l} \quad (\text{IV.17})$$

IV. The fourth term in right hand side (rhs) of equation is the dissipation rate of turbulence kinetic energy caused by work done by the smallest eddies against viscous stresses. For high Reynolds number flows and assumption of local isotropy this term can be written as:

$$\overline{\rho} \varepsilon = \overline{\mu \left(\frac{\partial u_i}{\partial x_j} \frac{\partial u_i}{\partial x_j} \right)} \quad (\text{IV.18})$$

V. This term describes the interaction of the density-velocity fluctuation correlation with the mean pressure gradient and is of importance in combustion flows [23]. This term has been neglected as in the [1].

VI. The last term in the equation is zero in constant density flows. It is argued that it has been associated with noise generation therefore considered to be negligibly small [23] at least in low Mach number flows. Mach number is in the range of 0.001-0.04 during compression stroke, therefore, the effect of this term is negligible.

The final form of **k-equation** can be written as:

$$\begin{aligned} \frac{\partial}{\partial t} (\overline{\rho} k) + \frac{\partial}{\partial x_j} (\overline{\rho U_j k}) = \frac{\partial}{\partial x_j} \left(\frac{\mu_t}{\sigma_k} \frac{\partial k}{\partial x_j} \right) + \mu_t \left(\frac{\overline{\partial U_i}}{\partial x_j} + \frac{\overline{\partial U_j}}{\partial x_i} \right) \frac{\overline{\partial U_i}}{\partial x_j} \\ - \frac{2}{3} \left(\mu_t \frac{\overline{\partial U_l}}{\partial x_l} + \overline{\rho} k \right) \frac{\overline{\partial U_l}}{\partial x_l} - \overline{\rho} \varepsilon \end{aligned} \quad (\text{IV.19})$$

IV.2.2.2 The ε -Equation

It is possible to develop similar transport equations for all other turbulence quantities including the rate of viscous dissipation ε [22]. The exact ε -equation contains many unknowns and immeasurable terms. The standard k - ε model, developed by Launder and Spalding [24], has two model equations one for k and other for ε .

Velocity scale \mathcal{V} and length scale ℓ can be represented in terms of k and ε as:

$$\mathcal{G} = k^{1/2} \quad \ell = \frac{k^{3/2}}{\varepsilon} \quad (\text{IV.20})$$

At high Reynolds number flows large eddy length scale ℓ can be used for dissipation term ε . Applying same approach as in the mixing length model the eddy viscosity as follows:

$$\mu_t = C_\rho \mathcal{G} \ell = \rho C_\mu \frac{k^2}{\varepsilon} \quad (\text{IV.21})$$

where C_μ is a dimensionless constant.

General form ε -equation can be written as:

$$\frac{\partial}{\partial t}(\bar{\rho}\varepsilon) + \frac{\partial}{\partial x_j}(\bar{\rho}U_j\varepsilon) = \frac{\partial}{\partial x_j} \left(\frac{\mu_t}{\sigma_\varepsilon} \frac{\partial \varepsilon}{\partial x_j} \right) + C_{\varepsilon 1} \frac{\varepsilon}{k} P_k - C_{\varepsilon 2} \bar{\rho} \frac{\varepsilon^2}{k} \quad (\text{IV.22})$$

where P_k is given in **Equation IV.17**.

The left hand side of **Equation IV.13** contains rate of change and convection terms. The first term of rhs of equation represents diffusion, second term gives production and third term shows destruction of dissipation rate. Prandtl number σ_ε connect the diffusivity to the turbulent viscosity μ_t . Production and destruction of turbulent kinetic energy are always closely linked. The dissipation rate ε is large where production of k is large. The model equation for ε assumes that its production and destruction terms are proportional to the production and destruction terms of the k -equation (**Equation IV.19**). The factor ε/k in the production and destruction terms makes these terms dimensionally correct in the ε -equation.

The k and ε equations contain five adjustable constants C_μ , $C_{\varepsilon 1}$, $C_{\varepsilon 2}$. Their values in standard k - ε model are:

$$C_\mu = 0.09, C_{\varepsilon 1} = 1.44, C_{\varepsilon 2} = 1.92, \sigma_\varepsilon = 1.30, \sigma_k = 1.00$$

The k - ε model has achieved notable successes in calculating a wide variety of thin shear layer and recirculating flows. The model performs well in confined flows where the Reynolds shear stresses are most important.

In spite of the numerous successes, the model shows only moderate agreement in unconfined flows. The model also has problems in swirling flows and flows with large rapid, extra strains (e.g. highly curved boundary layers and diverging passages)

since it does not contain a description of the subtle effects of streamline curvature on turbulence [22]. In order to overcome these deficiencies versions of models have been developed.

IV.2.3 The k-ε model variants:

The standard k-ε model does not perform well in compressed turbulence as in the compression stroke of the IC engine cycle. Because it is mainly developed for shear flows.

There are a number of the k-ε model variants. Watkins [8] derived an ε-equation for variable density flows, in which correlations containing density fluctuations were neglected. In his model a new term was added in ε-equation as:

$$S_\varepsilon = C_{\varepsilon 3} \rho \varepsilon \nabla \cdot u \quad (\text{IV.23})$$

which results from the compressibility effects appear as a natural product of the derivation with $C_{\varepsilon 3}=1$. He also neglected all other terms arising from compressibility effects.

Reynolds [14] showed that dissipation equation derived by Watkins does not predict the case of homogeneous turbulence field under rapid spherical compression correctly. For homogeneous turbulence, the convection and diffusion terms are zero and assuming “rapid distortion” the dissipation rate and destruction of ε term are neglected. In rapid distortion the angular momentum of the turbulent eddies should be conserved [25]. Therefore, the product of the turbulent length and velocity scales should remain constant during compression. Thus,

$$\ell_t k^{1/2} = C_\mu^{3/4} \frac{k^2}{\varepsilon} = \text{constant} \quad (\text{IV.24})$$

and under these circumstances, $C_{\varepsilon 3}$ terms becomes:

$$C_{\varepsilon 3} = \frac{2}{3}(C_{\varepsilon 1} - 2) \quad (\text{IV.25})$$

where $C_{\varepsilon 1}=1.44$ and $C_{\varepsilon 3}=-0.373$.

Morel and Mansour [9] extended Reynolds’ analysis to a number of compression cases that further includes cylindrical and unidirectional rapid

compression that lead to different values of $C_{\varepsilon 3}$ at each case. In this model source term for k -equation is suggested as in that of standard model and production term in ε -equation is modified.

$$S_k = P_k - \rho \varepsilon \quad (IV.26)$$

$$S_\varepsilon = \frac{\varepsilon}{k} \left[C_{\varepsilon 1} G - C_{\varepsilon 2} \bar{\rho} \varepsilon - \frac{2}{3} \nabla \bar{U} (C'_{\varepsilon 1} \mu_{eff} \nabla \bar{U} + C''_{\varepsilon 1} \bar{\rho} k) \right] \quad (IV.27)$$

where

$$P_k = G - \frac{2}{3} \nabla \bar{U} (\mu_{eff} \nabla \bar{U} + \bar{\rho} k) \quad (IV.28)$$

$$G = \mu_{eff} \left[2 \left\{ \left(\frac{\partial U}{\partial z} \right)^2 + \left(\frac{\partial V}{\partial r} \right)^2 + \left(\frac{V}{r} \right)^2 \right\} + \left(\frac{\partial V}{\partial z} + \frac{\partial U}{\partial r} \right)^2 \right] \quad (IV.29)$$

in cylindrical polar coordinates. Here $\mu_{eff} = \mu + \mu_t$ and $\mu_t = \rho C_\mu k^2 / \varepsilon$ and diffusivity terms are given as:

$$\Gamma_k = \frac{\mu_{eff}}{\sigma_k}, \quad \Gamma_\varepsilon = \frac{\mu_{eff}}{\sigma_\varepsilon} \quad (IV.30)$$

where constants in the equation are:

$$\sigma_k = 1.0, \quad \sigma_\varepsilon = 1.22, \quad C_\mu = 0.09, \quad C_{\varepsilon 2} = 1.92, \quad C_{\varepsilon 1} = 1.44, \quad C'_{\varepsilon 1} = 1.32, \quad C''_{\varepsilon 1} = 4.5$$

There are some more studies on the k - ε model to increase the model performance especially in compressed turbulence with different model constants [1].

IV.2.4. The modified k - ε - τ model

The k - ε model was developed for thin shear layer flows, and is known not to work well in more complex flows i.e. in recirculating flow, in adverse pressure gradients, in swirling flow etc [22]. All of these conditions prevail at some time during IC engine flows.

Therefore, there seems to be a need to develop more advanced turbulence models that are capable of returning more accurate predictions. One such model, which generally has been more successful than the k - ε model in predicting the flow field of other industrial or engineering flows, is the differential stress model (DSM) [26]. This requires the solution of transport equations for the Reynolds shear and

normal stresses, as well as for ε . Thus in three-dimensional flows, the model requires the solution of seven equations, in addition to the mean flow equations.

A peculiarity of IC engine flows is the bulk compression/expansion process. Gul [1] developed a less complex model, based on DNS results of Wu et al [2], to better account for these effects during compression and expansion. The effects of this on the mean flow and turbulence structure have been handled by adding additional terms to the ε equation only, related to the dilatation of the mean flow. In addition to above discussed terms, in this work this is applied by solving an extra equation for turbulence time-scale τ .

The modified k - ε - τ model equations can be written as follows:

***k*-equation:**

$$\frac{\partial}{\partial t}(\overline{\rho k}) + \frac{\partial}{\partial x_j}(\overline{\rho U_j k}) = \frac{\partial}{\partial x_j} \left(\frac{\mu_t}{\sigma_k} \frac{\partial k}{\partial x_j} \right) + P_k - \overline{\rho \varepsilon} \quad (\text{IV.31})$$

***\varepsilon*-equation:**

$$\frac{\partial}{\partial t}(\overline{\rho \varepsilon}) + \frac{\partial}{\partial x_j}(\overline{\rho U_j \varepsilon}) = \frac{\partial}{\partial x_j} \left(\frac{\mu_t}{\sigma_\varepsilon} \frac{\partial \varepsilon}{\partial x_j} \right) + C_{\varepsilon 1} \frac{P_k}{\tau} - C_{\varepsilon 2} \overline{\rho} \frac{\varepsilon}{\tau} - \frac{1}{3} C_{\varepsilon 3} \overline{\rho} \varepsilon \nabla \cdot \overline{U} \quad (\text{IV.32})$$

***\tau*-equation:**

$$\begin{aligned} \frac{\partial}{\partial t}(\overline{\rho \tau}) + \frac{\partial}{\partial x_j}(\overline{\rho U_j \tau}) &= \frac{\partial}{\partial x_j} \left(\frac{\mu_t}{\sigma_\tau} \frac{\partial \tau}{\partial x_j} \right) + C_{\tau 0} \overline{\rho} - C_{\tau 1} \overline{\rho} z \\ &\quad - C_{\tau 2} \frac{P_k}{\varepsilon} z - C_{\tau 3} \overline{\rho} \tau \frac{\nabla \cdot \overline{U}}{3} \end{aligned} \quad (\text{IV.33})$$

where z is the ratio of the two turbulence time scales, namely

$$z = \frac{\varepsilon \tau}{k} \quad (\text{IV.34})$$

The model constants are

$$C_{\varepsilon 1} = 0.75, \sigma_\tau = 1.1, C_{\varepsilon 2} = 1.0, C_{\varepsilon 3} = 0.67, C_{\tau 0} = 1.054, C_{\tau 1} = 1.1, C_{\tau 2} = 0.59, C_{\tau 3} = 0.83.$$

As there are now two independent time scales, eddy viscosity can be defined in two different ways:

$$\mu_t = C_\mu \rho \frac{k^2}{\varepsilon} \quad \text{or} \quad \mu_t = C_\mu \rho z_0^{-1} k \tau \quad (\text{IV.35})$$

the second order correlations of scalar quantities ($\overline{\rho u_i \phi_j^*}$) and velocity components are modeled by the eddy viscosity approach as:

$$-\overline{\overline{\rho u_i^* \phi_j^*}} = \Gamma_{\phi,T} \frac{\partial \overline{\phi}}{\partial x_j} \quad (\text{IV.36})$$

where $\Gamma_{\phi,T}$ is the turbulent eddy diffusivity and is evaluated as:

$$\Gamma_{\phi,T} = \frac{\mu_t}{\sigma_{\phi,T}} \quad (\text{IV.37})$$

$\sigma_{\phi,T}$ is the turbulent Prandtl-Schmidt number. As discussed above its value is in the order of unity.

IV.2.4.1. Boundary conditions

IV.2.4.1.a. Walls, Stagnation Enthalpy and Symmetry Axis

Boundary conditions for the mean flow were mentioned above and now that for the turbulent quantities will be discussed.

At walls a one-layer wall function treatment was used. Close to the wall the flow is influenced by viscous effects and does not depend on free stream parameters. The mean flow velocity only depends on the distance y from the wall, fluid density ρ and viscosity μ and the wall shear stress τ_w . So, $U(y, \rho, \mu, \tau_w)$ and dimensional analysis shows that

$$u^+ = \frac{U}{u_t} = f(y^+) \quad \text{and} \quad y^+ = \frac{\rho u_t y}{\mu} \quad (\text{IV.38})$$

this is called the **law of the wall** and contains two important dimensionless groups u^+ and y^+ . For thin layers of $y^+ < 5$ $u^+ = y^+$. Outside the viscous sublayer ($30 < y^+ < 500$) a region exists where viscous and turbulent effects are both important. In this region the **log-law layer** treatment is used.

$$u^+ = \frac{1}{\kappa} \ln(Ey^+) \quad (\text{IV.39})$$

where $\kappa=0.4187$ and $E=9.793$ are constants.

Applying log-law layer assumption dissipation rate and time scale are found as in [1]:

$$\varepsilon = \frac{C_\mu^{3/4} k^{3/2}}{\kappa y} \quad \text{and} \quad \tau = z_l \frac{k}{\varepsilon} \quad (\text{IV.40})$$

where z_l is a constant, $0.47 < z_l < 0.54$. Other derived quantities can be found on [1]

Centerline boundary conditions were zero gradient and fluxes set to zero due to the axisymmetry.

IV.2.4.1.b. Planes of inlet and exhaust apertures

The intake flow was assumed to enter the domain tangential to the valve-seat-angle with a uniform profile. Inlet turbulence parameters were calculated from the following relations; $k_{in}=0.01V_{in}^2$, $\varepsilon_{in}=c_{\mu}^{0.75}k_{in}^{1.5}/l_{in}$, $\tau_{in}=k_{in}/(\varepsilon_{in}C_{\varepsilon 2})$ where the inlet length scale is assumed to be $l_{in}=0.045L$ (L is valve lift)



PART V

SOLUTION PROCEDURE

V.1. INTRODUCTION

The solution method, which is of the finite-volume variety, includes steps. At first, the solution domain is divided into a finite number of discrete cells, then the derived partial differential equations in the preceding sections are converted into algebraic equations and finally the numerical values of the dependent variables at centers of the cells are determined.

V.2. METHOD OF DISCRETIZATION

Patankar [27] developed a method, which is called finite volume method based on the weighted residuals method for discretizing partial differential conservation equations. In finite volume method solution domain is divided into a number of nonoverlapping control volumes (or cells) such that there is one control volume surrounding each grid point. The differential equations are integrated over each control volume. Piecewise profiles expressing the variation of scalar quantity ϕ between the grid points are used to evaluate the required integrals. The result is the discretization equation containing the values of ϕ for a group of grid points.

Figure V.I illustrates the control volumes and boundaries employed for calculation of scalar quantities and axial and radial velocities in the solution domain. The scalar quantities, including pressure, enthalpy, turbulence variables density and viscosity, are located at the center of the cells denoted by capital letters P, N, S, E, W but axial and radial velocities are displaced to lie on the cell boundaries. The velocity

cells, denoted by small letters p, n, s, e, w, are defined such that the boundaries normal to the velocity direction pass through the pressure nodes. This positioning has the advantages that velocities lie between pressures that drive them, velocities are directly available for calculation of the convective fluxes across the cell boundaries and it avoids the decoupling of the adjacent velocities and pressures.

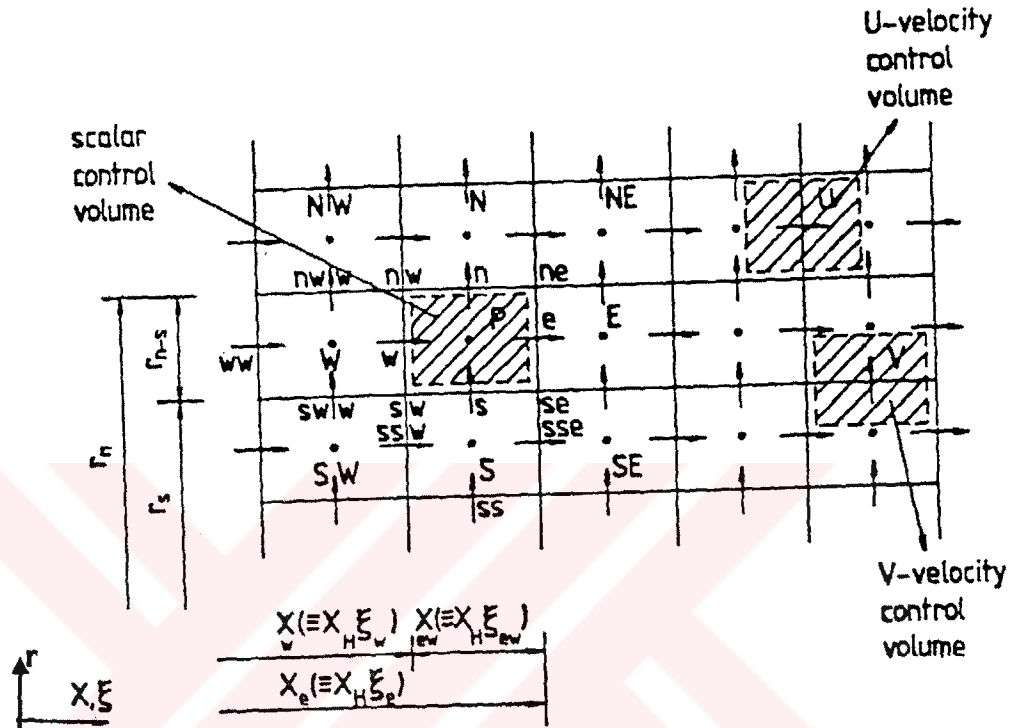


Figure V. 1 Computational grids, notation and control volumes of scalar variables and axial and radial velocities.

V.2.1. Derivation of The General Difference Equations

The discretized form of the general transport Equation III.29 is derived by integrating the equation over a typical cell volume and over a finite time increment δt . The integration of the general transport equation for entity ϕ located at the point P as shown in Figure V.I gives:

$$\begin{aligned}
\frac{1}{\delta t} \int_t^{t+\delta t} \left\{ \int_{\xi_w}^{\xi_e} \int_{r_s}^{r_n} z_p \rho \phi \, r dr \, d\xi + \int_{r_s}^{r_n} \left[\rho U \phi - \frac{\Gamma_\phi}{z_p} \frac{\partial \phi}{\partial \xi} \right]_{\xi_w}^{\xi_e} r dr \right. \\
+ \int_{\xi_w}^{\xi_e} \left[\rho r V_\phi - r \Gamma_\phi \frac{\partial \phi}{\partial r} \right]_{z_p} d\xi \\
\left. - \int_{\xi_w}^{\xi_e} \int_{r_s}^{r_n} S_\phi(\xi, r) z_p r dr \, d\xi \right\} dt = 0
\end{aligned} \quad (V.1)$$

The average values of ϕ and ρ throughout the cell volume can be approximated by the values at node of calculation. The assumptions made on **Equation V.1** and assumptions are given in [1].

Finally the discretized equation can be written in the form as:

$$A_P^n \phi_P^n = \sum_C A_C^n \phi_C^n + A_P^o \phi_P^o + \sum_C A_C^o (\phi_C^o - \phi_P^o) + S_{\phi P} \quad (V.2)$$

The subscripts 'n' and 'o' denote the 'new' and 'old' time levels respectively, separated by the interval δt . \sum_C represents the summation over the surrounding points E, W, N, S and the coefficients are given by:

$$\begin{aligned}
A_E^n &= \beta \dot{m}_e^n (\alpha_e^n - 1) & A_E^o &= (1 - \beta) \dot{m}_e^o (\alpha_e^o - 1) \\
A_W^n &= \beta \dot{m}_w^n \alpha_w^n & A_W^o &= (1 - \beta) \dot{m}_w^o \alpha_w^o \\
A_N^n &= \beta \dot{m}_n^n (\alpha_n^n - 1) & A_N^o &= (1 - \beta) \dot{m}_n^o (\alpha_n^o - 1) \\
A_S^n &= \beta \dot{m}_s^n \alpha_s^n & A_S^o &= (1 - \beta) \dot{m}_s^o \alpha_s^o \\
A_P^n &= A_C^n + A_P^o & A_P^o &= \frac{\rho_P^o V_P^o}{\delta t} - (1 - \beta) \sum_C \dot{m}_C^o \\
V_P &= \frac{1}{2} z_p (r_n^2 - r_s^2) (\xi_e - \xi_w)
\end{aligned} \quad (V.3)$$

where V_P is the cell volume per radian. β is a temporal weighting factor and m_i denote the cell-boundary mass flow rates, which are defined in terms of nodal values of density as:

$$\dot{m}_e = [f_l \rho_P + (1 - f_l) \rho_E] a_e U_e \quad (V.4)$$

f_l is linear interpolation factor, defined as $f_l = \delta \xi_{Ee} / \delta \xi_{EP}$. a_i represents cell boundary areas and α_i is the spatial difference parameter.

The discretized equations are used for dependent variables, in other words, scalar quantities. Treatment on the vectorial variables such as axial and radial

velocities and momentum equations are also required. Above mentioned equations also represent the vectorial variables by replacing variable ϕ with U for axial and V for radial velocities. However, recalculation of mass flow rates is required due to change in cell boundaries.

V.2.2. The Differencing Schemes:

In order to calculate the transported variable ϕ in **Equation V.2** at the cell faces differencing schemes are used. There are a number schemes such as central, upwind, hybrid, QUICK, etc.

The central differencing scheme has been used to represent the diffusion terms in the equation. It uses linear interpolation to calculate cell face values for the convective terms.

One of the major inadequacies of the central differencing scheme is its inability to identify flow direction. The upwind differencing scheme takes into account the flow direction when determining the value at the cell face: the convected value of ϕ at the cell face is taken to be equal to the value at the upstream node. Due to its simplicity the upwind differencing scheme has been widely used in early CFD calculations. This scheme produces erroneous results when the flow is not aligned with the grid lines. To overcome these deficiencies in differencing schemes Spalding [28] developed the hybrid-differencing scheme, which is based on a combination of central and upwind differencing schemes. The central differencing scheme, which is accurate in second-order, is employed for small Pecklet numbers ($Pe < 2$) and the upwind scheme, which is accurate in first-order, is employed for large Pecklet numbers ($Pe \geq 2$).

In this study hybrid scheme is employed in spatial differencing. The spatial difference parameter α_i is prescribed as:

$$\alpha_i = \begin{cases} 1 & \text{for } Pe > 2 \\ \frac{1}{2} + \frac{1}{Pe} & \text{for } -2 < Pe < 2 \\ 0 & \text{for } Pe < -2 \end{cases} \quad (\text{V.5})$$

The temporal weighting factor β represents the relative contributions of old and new time-level quantities in finite-volume equations. Its value varies between 0 and

1. If β is taken as 0, the scheme is called explicit in which new time values are calculated from old time values. It is a conditionally stable scheme. A linear variation of the variable ϕ between two-time-level is assumed in Crank-Nicholson scheme where $\beta=1/2$. This method is also a conditionally stable. The fully implicit scheme which assumes $\beta=1$ is used in this study. It is an unconditionally stable method and allows the use of arbitrarily large time steps with physically realistic solutions. Furthermore, because of no need to use old time-level coefficients it is efficient in respect of computer storage.

Final term in the general transport equation is source term. Integration over cell volume gives:

$$S_{\phi P} = S_I \phi + S_E \quad (\text{V.6})$$

S_I is included into the coefficient A_p^n in **Equation V.2**. This formulation increases the diagonal dominance of the coefficient matrix and enhances numerical stability if $S_I < 0$. Derivations of source terms for axial and radial momentum equations, stagnation enthalpy and turbulence parameters (k - ϵ - ν) are introduced in [1].

V.2.2.1. Assessment Of Boundary conditions:

The discretized general conservation equation is modified to employ the boundary conditions. It is done by setting the relevant coefficients equal to zero, and inserting the boundary conditions into finite-difference equations for such cells as fictitious source terms via modifications to the linearized source coefficients. ($A_N = 0$, for cells adjacent to north boundary; $A_E = 0$, for cells next to east boundary etc.)

The source terms at the boundaries are written as:

$$S_B = S_I \phi_P + S_E \quad (\text{V.7})$$

where S_I and S_E are determined according to the conditions prescribed at the boundary. In engine case there are three types of boundaries, which are fluid entry and exit planes at the inlet and exhaust valves, axis of symmetry and walls, which are cylinder, cylinder head and piston walls.

At inlet and exhaust apertures scalar quantities and flow properties have to be calculated along this boundary. The mass flow rate is determined by solving orifice **Equations III.25 and III.26** derived in previous sections during flow inlet. A_S

coefficient in discretized **Equations V.2 and V.3**) is set to zero for the cells adjacent to the aperture. The mass flow rate and normal velocity are determined at the exit plane in the similar manner.

Additional grid lines are required between the inlet valve and the cylinder head due to the valve movement as described in **Section III.1.4**. So, the description of the values of the scalar quantities is required along the newly inserted grid lines at the instant of the valve opening. This is done by ascribing the dominating variables at the grid lines next to the cylinder head to the scalar quantities at the instant of the valve opening while the velocities are set to zero. At the instant of the valve closing, the added grid lines are removed. In order to preserve the total mass balance, the mass contained within these grids is added to the remaining cells between the cylinder head and the piston face.

At the symmetry axis, the gradients of all properties are zero except for radial velocity. This condition is implemented by setting the coefficient A_S and boundary source S_B , described in **Equation V.7** to zero. In the case of radial velocity V_{rs} and S_B are set to zero.

The implementation of boundary conditions is also required at walls. This includes discretization of the derived equations in previous sections both for scalar quantities and flow variables [1].

V.3 Overall Solution Procedure

The derived momentum and continuity equations in which every velocity component appears are coupled and non-linear. Furthermore, the role of pressure is complex. Since it appears in momentum equations but there is no equation for pressure. If the pressure gradient is known, the process of obtaining discretized equations for velocities from the momentum equations is similar to that for any scalar. However, the pressure gradient is not normally known before the calculations. If the flow is compressible the continuity equation may be used as a transport equation for density and, in addition to the momentum equations, energy equation is a transport equation for the temperature. So, the pressure may be obtained from the density and temperature by using equation of state. However, if the flow is

incompressible the density is constant. In this case coupling between velocity and pressure introduces a constraint on the solution of the flow field.

Both the problems associated with the non-linearities in the equation set and the pressure-velocity coupling can be solved by adopting iterative solutions strategy such as SIMPLE [27, 22], SIMPLER, PISO, EPISO etc.

The SIMPLE (Semi-Implicit Method for Pressure-Linked Equations) algorithm is a guess and correct procedure for the calculation of the pressure and velocity fields on the staggered grid arrangement. Starting from an initial pressure field p^* its principal steps are:

- Initialize
- Set time step
- Set initial values of u , v , p and ϕ as old values in time
- Solve the discretized momentum equation to yield the intermediate velocity field (U^* , V^*).
- Solve the continuity equation in the form of an equation for pressure correction p' .
- Correct the pressure and velocity by means of

$$p_{I,J} = p_{I,J}^* + p'_{I,J}$$

$$u_{i,j} = u_{i,j}^* + d_{i,j} (p'_{I-1,J} - p'_{I,J})$$

$$v_{i,j} = v_{i,j}^* + d_{I,j} (p'_{I-1,J} - p'_{I,J})$$

$$\text{where } d_{i,j} = \frac{a_{i,j}}{A_{i,j}} \text{ and } d_{I,j} = \frac{a_{I,j}}{A_{I,j}}.$$

a and A represent cell face area and the coefficient of the cell volume equations respectively.

- Solve all other discretized transport equations for scalar ϕ
- Repeat until the fields p , u , v and ϕ have all converged.

All these steps are applied at each time step.

Refinements to SIMPLE algorithm have produced more economical and stable iteration methods. Like SIMPLER (SIMPLE Revised), SIMPLEC (SIMPLE Consistent) and PISO algorithms. An overview of these solution algorithms is presented [22].

The PISO (Pressure Implicit by Splitting of Operators) method of Issa [29] is a pressure-velocity calculation procedure developed originally for the non-iterative computation of unsteady compressible flows. This algorithm involves one predictor step and two corrector steps and may be seen as an extension of SIMPLE, with a further corrector step to enhance it. The temporal accuracy achieved by the predictor-corrector process for pressure and momentum is order of Δt^3 and $3\Delta t^4$ respectively. Therefore, the pressure and velocity fields obtained at the end of the PISO process with a suitably small time step are considered to be accurate enough to proceed to the next time step immediately and the algorithm is non-iterative.

CFD simulation of flow and heat transfer in internal combustion engines requires transient calculations that are inevitably time consuming and expensive especially with three-dimensional geometries. Ahmadi-Befrui et al [30] presented a version of PISO known as EPISO suitable for predicting engine flows.

In this study a modified version of EPISO algorithm developed by Gul was used. In this algorithm, global adjustments are made to the pressure and density fields and time-evolving frame and flow velocities relative to grid lines require to be taken into account. Details of algorithm can be found in [1]. When the normalized sum of the absolute residuals for the velocity equation have fallen below a specified level, in this study taken as 10^{-3} , the solution to the algebraic equations is assumed to have converged.

V.3.1. Solution of Discretized Equations:

The coefficients of discretized equations derived in previous sections give a tri-diagonal matrix. These coefficients and independent variables are solved by using tri-diagonal matrix algorithm (TDMA) developed by Thomas [31]. It is applied iteratively, in line-by-line fashion, to solve multi-dimensional problems and widely used in CFD programs. It has two parts the first of which is used for determination of coefficients, called forward elimination, and the second, back-substitution, is used for inserting coefficients to find out variables.

V.3.2. Outline of The Solution Procedure

The method of solution starts from fields of initial values according to given details of the chamber configuration, piston and valve motion and boundary

conditions. Then it marches forward in increments of time δt , which is equivalent to crank angle $\delta\Theta$, at every interval iteratively solving the coupled finite-volume equations for the dependent variables, until the desired period is covered. Initial conditions at the beginning of computation were evaluated after one complete cycle run. The turbulence quantities set to the initial inlet conditions.

At each time interval, the method updates the fields of variables from the preceding interval in the following sequence of steps:

1. The piston velocity, $U_p(\Theta)$, and position $z_p(\Theta)$ are calculated:

$$z_p(\Theta) = z_{TDC} + \frac{S_t}{2} \left\{ 1 - \cos(\Theta) + \frac{2L_{cr}}{S_t} \left[1 - \left(1 - \left(\frac{S_t}{2L_{cr}} \right)^2 \sin^2 \Theta \right)^{1/2} \right] \right\} \quad (V.8)$$

$$U_p(\Theta) = \frac{S_t}{2} \omega \left\{ \sin \Theta + \frac{1}{2} \left(\frac{S_t}{2L_{cr}} \right) \left[\left(1 - \left(\frac{S_t}{2L_{cr}} \right)^2 \sin^2 \Theta \right)^{-1/2} \sin 2\Theta \right] \right\}$$

in which Θ is the crank angle measured from the TDC of induction, z_{TDC} is the engine clearance, S_t is the engine stroke, L_{cr} is the connecting rod length and ω is the engine angular velocity.

2. The valve lift L is obtained from the valve lift diagram, and its velocity is approximated as:

$$U_{valve} = [z_v(\Theta) - z_v(\Theta - \delta\Theta)] / \delta t \quad (V.9)$$

where $z_v = L - z_{sep}$ and z_{sep} is defined in [8] as:

$$z_{sep} = 0.62 \text{ mm for } 0.113 < L/D < 0.117$$

$$z_{sep} = 1.86 \text{ mm for } 0.117 < L/D$$

3. The axial grid increments are adjusted according to movement of the piston and the valve.
4. The equations for mass flow rate and pressure drop across the valve are solved.
5. The pressure and density are adjusted globally to initial new-time-level values p^g and ρ^g . (here g represents guessed values)
6. The discretized momentum equations are solved to get U_i^* .
7. The pressure field is adjusted locally to give p^* by solving the first pressure-correction equation. The density is also corrected to yield ρ^* and then the

intermediate velocities U_i^{**} are calculated through the first velocity correction.

8. The energy equation is solved to obtain final field values of temperature T^* . Densities are also updated at this stage to an intermediate level $\rho^{*+\frac{1}{2}}$ by using final T^* values.
9. The second pressure correction equation is solved for p_2' and p^* is corrected to obtain p^{**} field. Densities and velocities are updated to ρ^{**} and to U_i^{***} by using second correction equation.
10. The fields of turbulent variables, k , ε and τ , are then obtained by solving their difference equations respectively and iterating this procedure from k to τ equations until the prescribed convergence criterion is satisfied.
11. The turbulent viscosity μ_τ field are calculated and the newly obtained fields are then further updated by repeating steps 6 to 10 until the second convergence criterion is satisfied.
12. Second global adjustment procedure is performed for the final pressure and density fields of the time step and temperature and stagnation energy are adjusted to ensure thermodynamic consistency.
13. The procedure then advances to the next time-level and recommences from level 1 using the currently computed solutions as old time-level values.

PART VI

THESIS STUDIES AND RESULTS

VI.1. THESIS STUDIES

Thesis studies started from updating and modifying the used computer program to the Fortran 90 standards. Computer program was updated and modified by dividing it into subprograms and using modules to store common variables. A simple preprocessor was developed in VB programming language (Figure C.1). Main program was adapted to preprocess. Results were postprocessed by Techplot.

In order to find out the sensitivity of the solutions to the mesh density and size of the computational time-step, a number of tests were performed. Computational grids used for the refinement tests are uniformly spaced, within two distinct regions for the flat-piston case shown in Figure III.2 with 400, 900, 2500, 3600 and finally approximately 10000 nodes and time-steps equivalent to $\delta\theta=0.25$ and 0.5 CA respectively. Here cell-Courant number (Co) was kept within a specific range instead of testing each grid distribution with every time step since the stability of the system would greatly reduce when this number is out of a certain range ($Co_x Co_y = UV(\delta t)^2 / \delta x \delta y \Rightarrow M * N * (\delta t)^2 \approx 800-2000$ where M and N are number of grids in x and y directions respectively).

On the other hand, both the $k-\varepsilon$ and $k-\varepsilon-\tau$ turbulence models were applied to determine accuracy of new turbulence model's results. Experimental data taken by LDA of mean flow velocities and axial and radial turbulent intensities are available in [32,33]. In this study, two different cases for which some of operating conditions are 200 rpm, and compression ratios of 3.5 (Case I) and 6.7 (Case II) were examined.

The maximum valve lift is 7.3 mm for Case I and 8 mm for Case II. These operating conditions are of the model engine simulator developed in the Imperial College. Thus, computer simulation results and performance of the suggested three-equation turbulence model can be compared with the experimental data. The model engine can be seen in **Figure V.1** and details of the test cases are summarized in the **Table VI.1**.

Finally, in IC engine works interpretation of the results, in other words, post-processing of output data is also an important subject. In post-processing of the output data a program, called Techplot, was used. Techplot is a powerful tool for visualizing a wide range of technical data. It offers X-Y plotting two-dimensional and three-dimensional surface plots in a variety of formats and three-dimensional volumetric visualization.

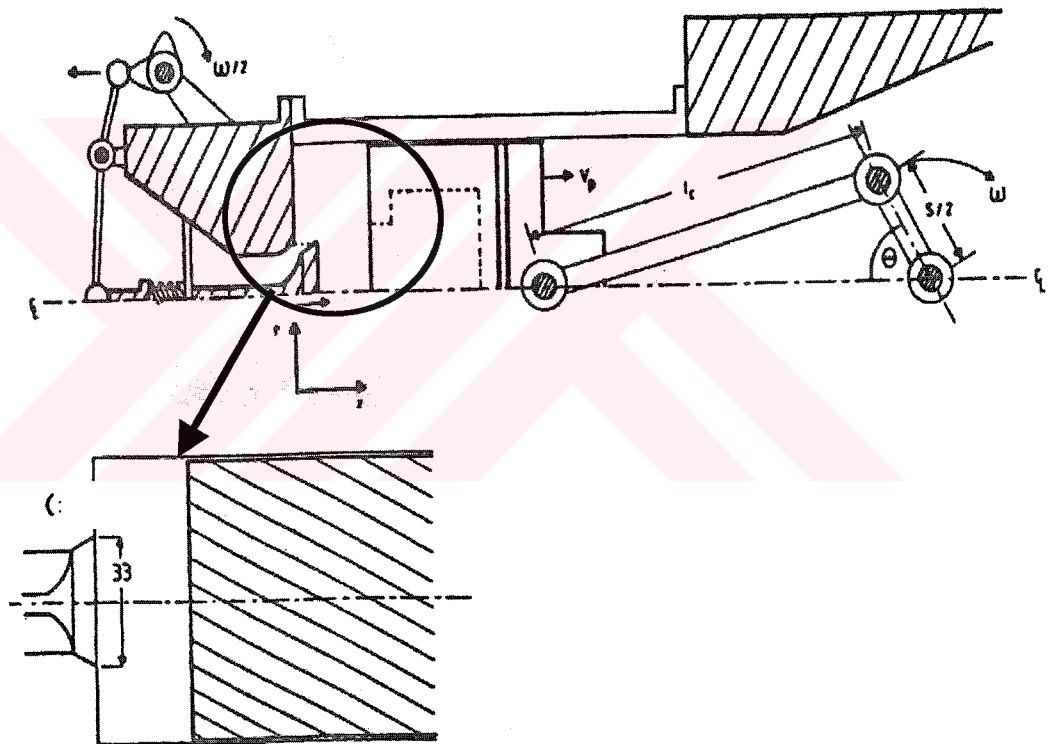


Figure VI. 1 Diagram of Imperial College compressing engine simulator and engine cylinder.

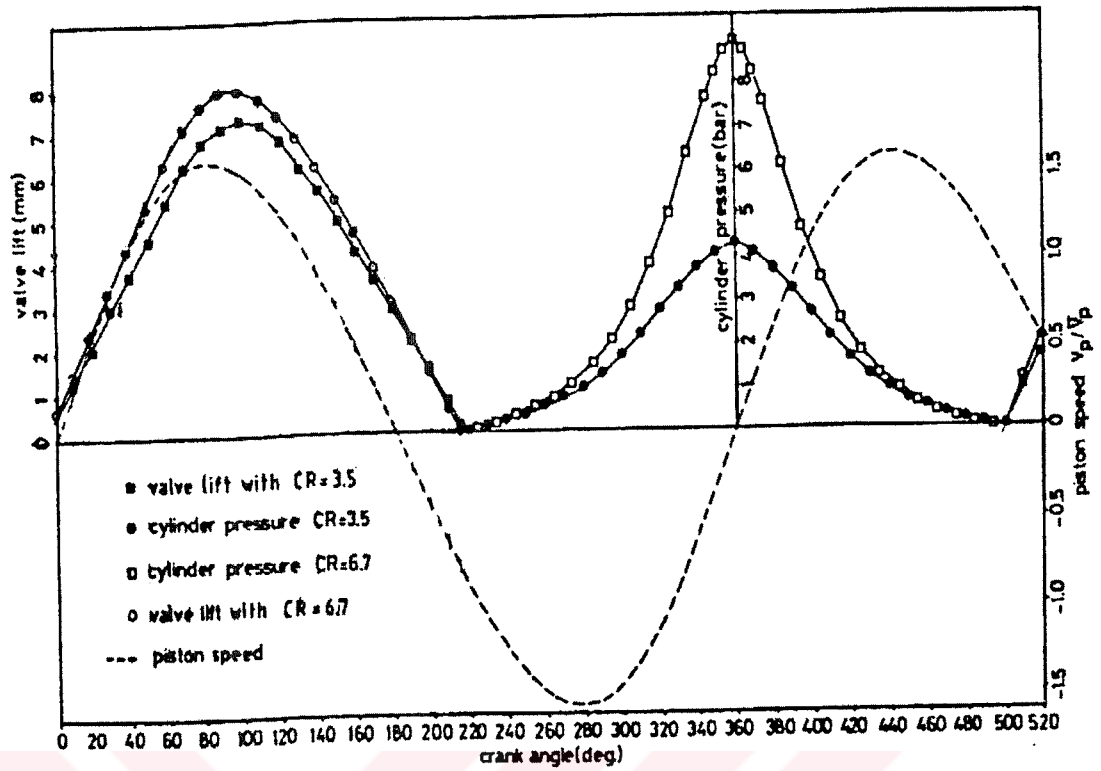


Figure VI. 2 Variation of valve lift, piston speed and cylinder pressure with crank angle of the model engines

Table VI. 1 Details of test cases; the Imperial College 2D engine simulator.

	Case I	Case II
Cylinder Bore [mm]	75	75
Stroke [mm]	94	94
Connecting-Rod Length [mm]	363.5	363.5
Compression Ratio	3.5	6.7
Engine Speed [rpm]	200	200
Mean Piston Velocity [m/s]	0.626667	0.626667
Max. Valve Lift (L_{max}) [mm]	7.3	8
Valve Diameter (D_v) [mm]	34	34
L_{max}/D_v	0.21	0.24
Valve seat angle	60°	60°

VI.1.1. The Specification of The Inlet and Initial Conditions

At the beginning of the computation the inlet and initial values of variables, including mass flow rate, radial and axial velocity components, must be specified. The mass flow was calculated from a zero-dimensional calculation of the overall continuity and energy equations coupled with an orifice discharge coefficient based on inlet Reynolds number. This intake flow was assumed to enter the domain tangential to the valve-seat-angle with a uniform profile. The inlet variables are calculated by the aforementioned equations in Section III.1.3.2. For initial conditions, the in-cylinder turbulence energy k_{in} , the length scale l_{in} and turbulence dissipation rate ε_{in} were specified as:

$$k_{in}=0.056 m^2/s^2, l_{in}=0.03D \text{ (for typical pipe flows)}, \varepsilon_{in}=0.831 m^2/s^3$$

For starting conditions, the in-cylinder values for the turbulence energy and the dissipation rate were assumed to be equal to the inlet boundary values. But, during the engine cycle, the inlet boundary conditions for the turbulence quantities were specified in Section IV.2.4.1.b.

At the start of the induction, the inlet air and in-cylinder temperature and pressure were taken as 295° K and 1 atm respectively.

The computation started at TDC and the initial velocity assumed as zero. However, to decrease the uncertainties the results were evaluated after one complete cycle run (i.e. after 720°). Details of operating conditions are in the table below.

Table VI. 2 Valve opening and closing and estimated temperatures of the engine simulator.

	Case I	Case II
Valve opening for intake	-6° CA	-6° CA
Valve closing for intake	226° CA	226° CA
Valve opening for exhaust	496° CA	496° CA
Valve closing for exhaust	6° CA	6° CA
Cylinder Wall Temp [K]	340	350
Cylinder Head & Wall [K]	340	350
Piston [K]	360	370

Assessment and comparison of solution algorithm, described in Section V.3 as modified EPISO, can be found in [1].

VI.2. RESULTS AND DISCUSSIONS

For both test cases an overall impression of the in-cylinder behavior is provided in terms of plots at selected crank angles. All data shown in figures were obtained for 10000 grid-density run. The predictions of *the MM k-ε* model and the suggested model, *the k-ε-τ* model, were presented in figures.

Computational grid arrangements for test **Case I** and **Case II** can be seen in the **Figure VI.3**.

In **Figure VI.4** and **Figure VI.5**, the predictions of the velocity fields (velocity field and particle tracking) for test **Case I** are presented for both models. And, the turbulence intensity distributions for this test case are shown in **Figure VI.6** & **Figure VI.7** in aforementioned sequence.

The vector plots of velocity field for test **Case II** are shown in **Figure VI.11** and **VI.12** for both models. **Figure VI.11** and **VI.12** illustrate turbulence intensities results for this test case.

The predictions of the axial mean velocity and turbulence intensity profiles of the *MM k-ε* and *the k-ε-τ* models are compared with the experimental data [32] in **Figures VI.8-VI.13** and **Figures VI.18-VI.20** for test **Case I** and **Case II**, respectively.

VI.2.1. The Predictions and Comparisons for Case I

VI.2.1.1. Induction Stroke (TDC to $\Theta=180^\circ$ CA)

The results show that the flow field during early stages of induction (for $CA=36^\circ$ to 90°) is dominated by transient annular intake jet emanating from the valve orifice as can be seen from **Figure VI.4** & **Figure VI.5**. The intake jet entry angle is approximately that of the valve seat (60°). Although appearing to undergo minor deflections, intake flow penetrates and impinges on the piston or cylinder wall, depending on the piston position. Then, it separates into two strong recirculation zones (vortex) one of which is formed at the cylinder head-wall corner and the other is formed behind the inlet valve. Both vortices are toroidal. The center of both recirculation zones appears to be slightly more to left than those of the *k-ε* model [34]. The centers of both recirculation zones move downstream towards the piston

until mid-intake stroke; this movement is small in the former while the latter stretches and becomes the dominant one.

During early intake stroke the turbulence intensity contours of **Figure VI.7** suggest that the origin of induction generated turbulence lies mainly within the shear layers on either side of the induction jet. Turbulence intensity contours have higher gradients at the centers of the recirculation zones and impingement points on the cylinder wall. Turbulence is then transported downstream towards the piston but its diffusion towards the cylinder axis is small, resulting in low levels of turbulence in the region of the valve wake.

At the late induction stroke (for $CA=90^\circ$ to 180°), the growth of the main vortex by the intake mass flow and stretching by piston continues until about 120° (not shown in Figures) and then starts weakening with the fall of the intake jet momentum. The center of main vortex is located towards the left compared with the that of the MM $k-\varepsilon$ model (**Figure VI.6** and **Figure VI.7**).

The distribution of turbulence intensity at $CA=135^\circ$ is similar to that at $CA=90^\circ$ (**Figure VI.7**). But, its magnitudes show lower levels than prediction of the $k-\varepsilon$ model. Turbulence intensity in the main vortex remains at the same level with the $CA=90^\circ$ and tends to decay towards the end of intake stroke. It means that the turbulence occurred in the main vortex is independent of the intake jet and is determined by the local turbulence generation.

Near the end of the induction, a rapid decay in the mean velocity field is observed at $CA=180^\circ$ in **Figure VI.5**. This decay is partly a consequence of the fall-off in the induction flow rate, and the retarding action of turbulent stresses, but it is probably also connected with the changes in the pressure field brought about by the reversal of the piston motion. However, vortex structure persists under its inertia to the end of induction in agreement with the measurements of Bicen [33], Arcoumanis [32] and results of the [35].

The turbulence intensity levels for late induction stroke show similar behavior of decaying to the mean flow (**Figure VI.7**).

VI.2.1.2. Compression Stroke ($\Theta=180^\circ$ CA to $\Theta=360^\circ$)

The velocity field during early compression stroke, $CA=180^\circ$ to 270° , shows continuous weakening of induction generated mean flow structure (**Figure VI.5**,

CA=180° to 270°). The piston induced pressure gradients and existence of a small amount of out-flow do not seem to influence the vortex structure.

The velocity field vectors at CA=234°, which is just after the inlet valve closure (IVC), show a weak and short-lived recirculation zone created in front of the piston (however, this kind vortex is observed behind the valve in [1]). It might be remains of the vortex at ‘the cylinder wall-piston corner’ at 180° CA. The observed vortex at previous crank angle, which is at ‘the cylinder head-wall corner’, has disappeared. Moreover, the center of the main vortex shifts towards the cylinder wall due to the piston motion (Figure VI.4 and Figure VI.5).

At late stage of compression stroke (for CA=270°), the velocity field shows considerable reduction in the size and strength of the main vortex. The center of the main vortex is closer to the cylinder head than prediction of the MM model. The remains of the third vortex at the ‘cylinder wall-piston corner’ can be still be distinguished.

The turbulence intensity levels continue to decrease and considerable homogeneity in the radial direction can be observed (Figure VI.6 and Figure VI.7). The implications are that the turbulence generation by the main vortex is rapidly falling and relaxing to a stage controlled by the cylinder walls.

The velocity field at 324° CA shows further reduction in the size of the main vortex and considerable weakening of the flow due to the reduction in the piston speed. The distribution of turbulence parameters shows a continuous relaxation to a structure controlled by the combustion chamber geometry.

Figure VI.7 indicates also that turbulence intensity levels are weaken more. Tendency towards homogeneity in overall flow structure is also observed.

The velocity field at CA=360° shows a weak mean flow due to the persisting main vortex. \bar{U}_{max} at this crank angle is higher in the predictions of the MM $k-\varepsilon$ model indicating a weaker damping of the flow field than the modified $k-\varepsilon-\tau$ model (Figure VI.4 and Figure VI.5). The distribution of turbulence intensity shows continuous tendency towards homogeneity (Figure VI.6 and Figure VI.7).

The velocity field at CA=380°, early expansion stroke, shows that the vortexes observed at previous crank angle have destructed and the establishment of almost one dimensional flow in the direction of the piston motion. The distribution of the turbulence intensity shows an increasing homogeneity and lower turbulence levels.

VI.2.1.3. Comparison of Results with The Experimental Data

Comparison of results with the experimental data will give more accurate assessment of suggested turbulence model. It was done by comparing the predictions of the normalized mean axial velocity and turbulence intensity values of the models, and $k-\varepsilon-\tau$ model, with the measurements. **Figures VI.8-VI.13** show these comparisons in which full lines represent the $k-\varepsilon-\tau$ model, dashed lines are the MM $k-\varepsilon$ model and symbols show measurements

The measured [32,33] and predicted radial profiles of the axial mean velocity and turbulence intensity at 36° are shown in **Figure VI. 8**. The position of the peak in the radial velocity is well predicted by the $k-\varepsilon$ model but cannot be captured by the $k-\varepsilon-\tau$ model.

The measurements for turbulence intensity indicate a double-peak profile. The second peak is captured by the $k-\varepsilon-\tau$ model whereas it cannot capture the peak near the cylinder wall. The $k-\varepsilon$ model gives better predictions at this crank angle.

The comparisons of corresponding profiles at 90° are shown in **Figure VI.9**. The stretching of the main vortex by the piston and an increase in its peak velocity together with an increase in the level of turbulence intensity are evident from **Figure VI.9**. The predictions of both models show similar trends. However, the positions of the peak velocities and their magnitude as well as the recirculation zone behind the valve are captured well by the $k-\varepsilon-\tau$ model than the $k-\varepsilon$ model. Turbulence intensities are also predicted better by the $k-\varepsilon-\tau$ model.

In **Figure VI.10**, the prediction of the mean velocity profiles at 270° shows that the strength of the main vortex persisting from the induction is grossly over-predicted by both turbulence models. According to data, the mean flow at the measurement location ($z=15mm$) is almost one dimensional, in the direction of the piston motion, except for a weak vortex near the cylinder wall and the turbulence intensity has decayed to the level 0.75 times of piston mean velocity and is virtually homogeneous. For the turbulence intensities, the $k-\varepsilon-\tau$ model and the MM $k-\varepsilon$ model show an over prediction, although the tendency towards homogeneity is well predicted.

Combustion process is affected from the turbulence structure of the flow. Therefore, the accurate prediction of the flow near end of the compression stroke,

which is just before the combustion stroke, has a particular importance. In figures the predictions of this period is presented for two crank angles of 324° and 360° .

The measurements at 324° CA express that the mean flow is dominated by the piston motion and is nearly one-dimensional although the remains of the main vortex near the ‘cylinder head-wall corner’ can still be observed. The apparent flow structure in the region near the ‘cylinder head-axis’ can either be remains of a vortex generated behind the valve by the outgoing flow during early compression or a weak recirculation generated near the end of compression. It will probably be due to measurement errors in a strongly turbulent flow with small mean velocity. Turbulence intensity measurements show a homogeneous flow structure.

The figure, **Figure VI.11**, at this crank angle shows that the $k-\varepsilon-\tau$ model predicts better profiles and magnitudes than does the $k-\varepsilon$ model at the axial measurement locations near the piston surface. Differences in predictions of both models are small at the other measurement locations. Turbulence intensity levels are in rather good agreement with the data, with the level of agreement depending on the axial position.

The measurements at 360° in **Figure VI.12** show an almost quiescent flow and homogeneous turbulence level of 0.6 times of piston mean velocity. The $k-\varepsilon-\tau$ model predicts the mean velocity relatively better than the MM $k-\varepsilon$ model, particularly at the closer measurement station to the cylinder head. At the station of $z=32\text{ mm}$ the $k-\varepsilon-\tau$ model predicts better profile but overestimates magnitude. The turbulence intensity level predictions are also in agreement with the measurements but the MM $k-\varepsilon$ model underestimates.

The agreement with the axial velocity measurements is impaired by the under-prediction of the decay of the main vortex throughout the compression stroke. In aforementioned results, it is observed that turbulence intensities are better predicted than axial mean velocities during late compression. Since the shear stress contribution to the main vortex, to the turbulence generation, is small during compression. Furthermore, the compressive influence of the cylinder walls on the turbulence structure is significant for which the $k-\varepsilon-\tau$ model is modified.

The measurements at 380° CA, representing the early expansion, show a one-dimensional mean flow in the direction of the piston motion and homogeneous turbulence level. The $k-\varepsilon-\tau$ model captures better the mean axial velocity profiles and

magnitudes for all measurement locations. The predicted turbulence intensities are still in very good agreement with measurements. The $k-\varepsilon-\tau$ model predictions are better than the MM $k-\varepsilon$ model **Figure VI.13**.

VI.2.2. The Predictions and Comparisons for Case II

VI.2.2.1. Induction Stroke (TDC to $\Theta=180^\circ$ CA)

The results show that during early induction stroke (for TDC to 90° CA), intake jet impinges on the piston and produces a different flow structure than Case I in agreement with the measurements of the Arcoumanis et. al[32] and Bicen [33] and predictions of [35]. Later in the induction stroke, the growth of the main vortex and its stretching by the descending piston causes outward deflection and impingement of the intake jet on the cylinder wall. The third vortex appears in the ‘cylinder wall-piston corner’ by 90° CA. A similar flow structure to that of Case I is produced until the end of the induction stroke (**Figure VI.14** and **Figure VI.15**).

The distribution of turbulence intensity at 36° CA shows the generation of large turbulence levels within the shear layers and impingement location. The levels in the intake jet region are similar to those in Case I. However, the $k-\varepsilon-\tau$ model (**Figure VI.17**) predicts higher magnitudes than the $k-\varepsilon$ model (**Figure VI.16**) in this region. The evolution of the turbulence is similar to that of the Case I except for higher levels in the main vortex.

At 90° CA, the turbulence level predictions of the $k-\varepsilon-\tau$ model are higher in magnitudes than the $k-\varepsilon$ model and differences in predictions reduce even more near end of the induction stroke. The predicted higher turbulence levels decay at faster rates during the late induction than in Case I, which is in accord with the measurements, due to weakening of the mean flow.

VI.2.2.2. Compression Stroke ($\Theta=180^\circ$ CA to $\Theta=360^\circ$)

The evolution of the mean flow during the compression stroke is similar to that of Case I can be seen in (**Figure VI.14** and **Figure VI.15**). Attenuation occurs over the entire cylinder volume and results in greatly diminished velocities around IVC. Also observed at higher crank angles (CA= 234°) is a weak recirculation zone behind the valve created by the outgoing flow during early compression that disappears quickly. The ring vortex near the ‘cylinder head-wall corner’ breaks up by the time

of inlet valve closure and the third vortex near the piston, which is stronger in this case, disintegrate before the mid-compression (CA=270°). Unlike Case I, the mean vortex decays to a lingering weak motion at the TDC of compression ratio and in the early expansion the flow is almost one-dimensional and no structure is observed.

The distributions of the turbulence intensity during compression are similar for the case of compression ratio of 3.5 and show decay and tendency of turbulence towards homogeneity, except the decay rate which is faster during early compression than in Case I, due to the more rapid weakening of the mean flow. The levels of turbulence intensity predicted by the $k-\varepsilon-\tau$ model (Figure VI.17) is somewhat higher than those of the $k-\varepsilon$ model (Figure VI. 16) at the beginning of the compression stroke. After IVC the $k-\varepsilon-\tau$ model predicts slower reduction than the MM $k-\varepsilon$ model.

At 380° CA, the turbulence levels predicted by the $k-\varepsilon-\tau$ model are higher than the MM model. (Figure VI. 16 and VI.17)

VI.2.2.3. Comparison of Results with The Experimental Data

The comparisons between the measurements and the predictions of the normalized mean axial velocity ($\overline{U}/\overline{V}_p$) and turbulence intensity (u'/\overline{V}_p), obtained by the $k-\varepsilon-\tau$ model and the MM $k-\varepsilon$ model are presented in (Figure VI.18- VI.20) corresponding to CA=324°, 360° and 380° respectively.

The measurements at CA=324° show a mean flow in the direction of the piston motion and nearly homogeneous turbulence intensity of about $u' \approx 0.5$ to 0.6 of piston mean velocity (Figure VI.18). At the station $z=10mm$ the mean axial velocity profile exhibits a peak near the cylinder wall, opposite to the predictions, implying non-existence of the main vortex as opposed to Case I. However, these predicted profiles are consistent with the discussed velocity field results.

The modified $k-\varepsilon-\tau$ model predicts larger decay of the intake generated main vortex and higher levels of turbulence intensity than does the MM model. Therefore, the agreement between data and the $k-\varepsilon-\tau$ model, in respect of the mean velocity, is better than that of the MM model especially at the measurement location of $z=21mm$.

The measurements at CA=360° show an almost quiescent flow which indicates the dependence of the mean flow on the piston-induced pressure gradients. The turbulence intensity at TDC is still almost homogeneous with a level of $u' \approx 0.45$ to

0.5 times of mean piston velocity. That is to say, the effect of the increase in compression ratio between Case I and Case II is to slightly reduce the turbulence intensity at TDC. The $k-\varepsilon-\tau$ model predicts the essentially quiescent flow at TDC reasonably well while the $k-\varepsilon$ model returns rather higher levels for the mean velocities. The measurements show a peak velocity near the cylinder wall opposite to the both models predictions. However, both models predictions are consistent with the velocity field results in which a recirculation zone was observed near the cylinder wall. Turbulence intensity profiles, on the other hand, are predicted better by the $k-\varepsilon-\tau$ model than the MM $k-\varepsilon$ model that suffers from nearly 50% lower levels (Figure VI. 19).

The experiment indicates a jet near the cylinder wall during early expansion stroke (CA=380°, Figure VI.20), due to the rapid expansion of the entrapped air in the ‘cylinder wall-piston crevice’ [1], resulting in considerably large velocity and high levels of turbulence intensity. This wall-jet cannot be predicted since the clearance between the piston and the cylinder wall has not been represented in the computations. However the agreement with the measurements in the bulk flow of the flow is reasonably good since the influence of the jet is confined to the region near the wall and the rest of the flow is still almost one-dimensional. The turbulence intensity also remains almost homogeneous except the ‘cylinder wall-piston corner’ which is captured well by the $k-\varepsilon-\tau$ model whereas the $k-\varepsilon$ model under-estimates it at both measurement locations.

PART VII

DISCUSSION AND EVALUATION

In this study, three-equation model was tested for in-cylinder engine flows to compare the general performance during induction and compression stroke of the engine simulator. Both the $k-\varepsilon-\tau$ and the MM $k-\varepsilon$ -models yield qualitatively similar behavior of the in-cylinder flow, however, the $k-\varepsilon-\tau$ model produces better profiles in most of the locations where comparisons are made with the experimental data.

The $k-\varepsilon-\tau$ model damps main vortex more, giving better agreement for the mean velocities than the MM model during late compression stroke. Predicted turbulence intensities by the $k-\varepsilon-\tau$ model during this stage are in good agreement with the data.

The increase in compression ratio between Case I and Case II produces stronger mean flow and higher turbulence levels, due to the impingement of the intake jet on the piston during early induction. This decays faster during late induction in the $k-\varepsilon-\tau$ model than the MM $k-\varepsilon$ model. The influence on compression stroke is to produce weaker mean flow but similar turbulence levels near TDC in accord with the measurements.

The center of the main vortex and the stagnation point of the impingement jet on the cylinder wall was predicted to be slightly to the left in the $k-\varepsilon-\tau$ model than did in the $k-\varepsilon$ model

Finally, there are short-lived vortexes detected by the $k-\varepsilon-\tau$ model that requires measurements at these locations to confirm these predictions. Moreover, there are needs for modifications to obtain more consistent predictions of the profiles and turbulence levels with the measurements.

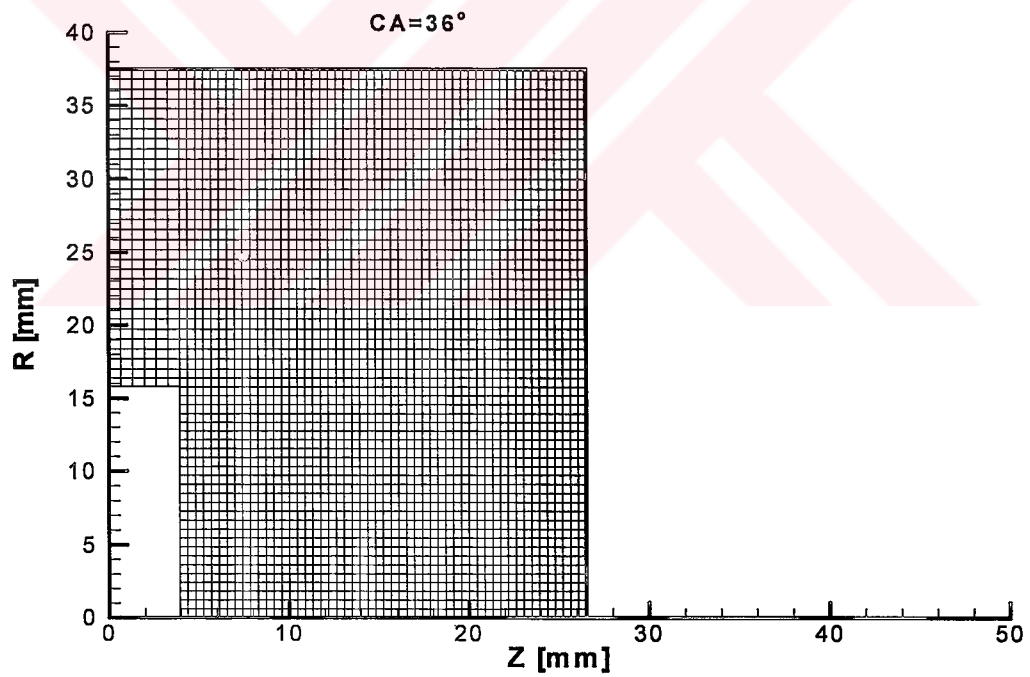
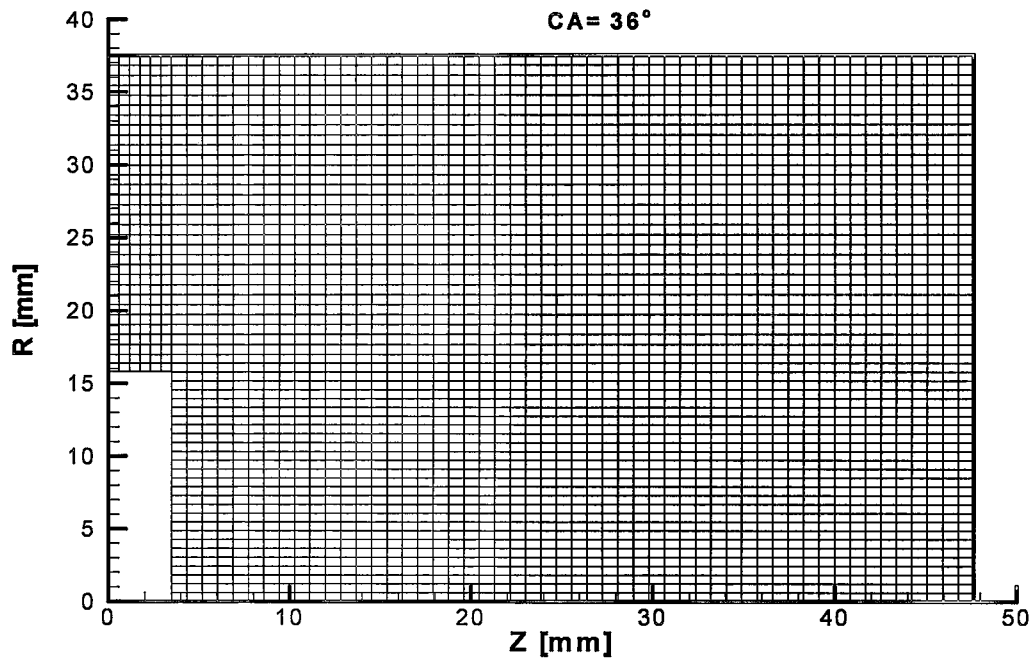


Figure VI.3 Computational grid arrangements; for test Case I (CR= 3.5) and Case II (CR=6.7) .

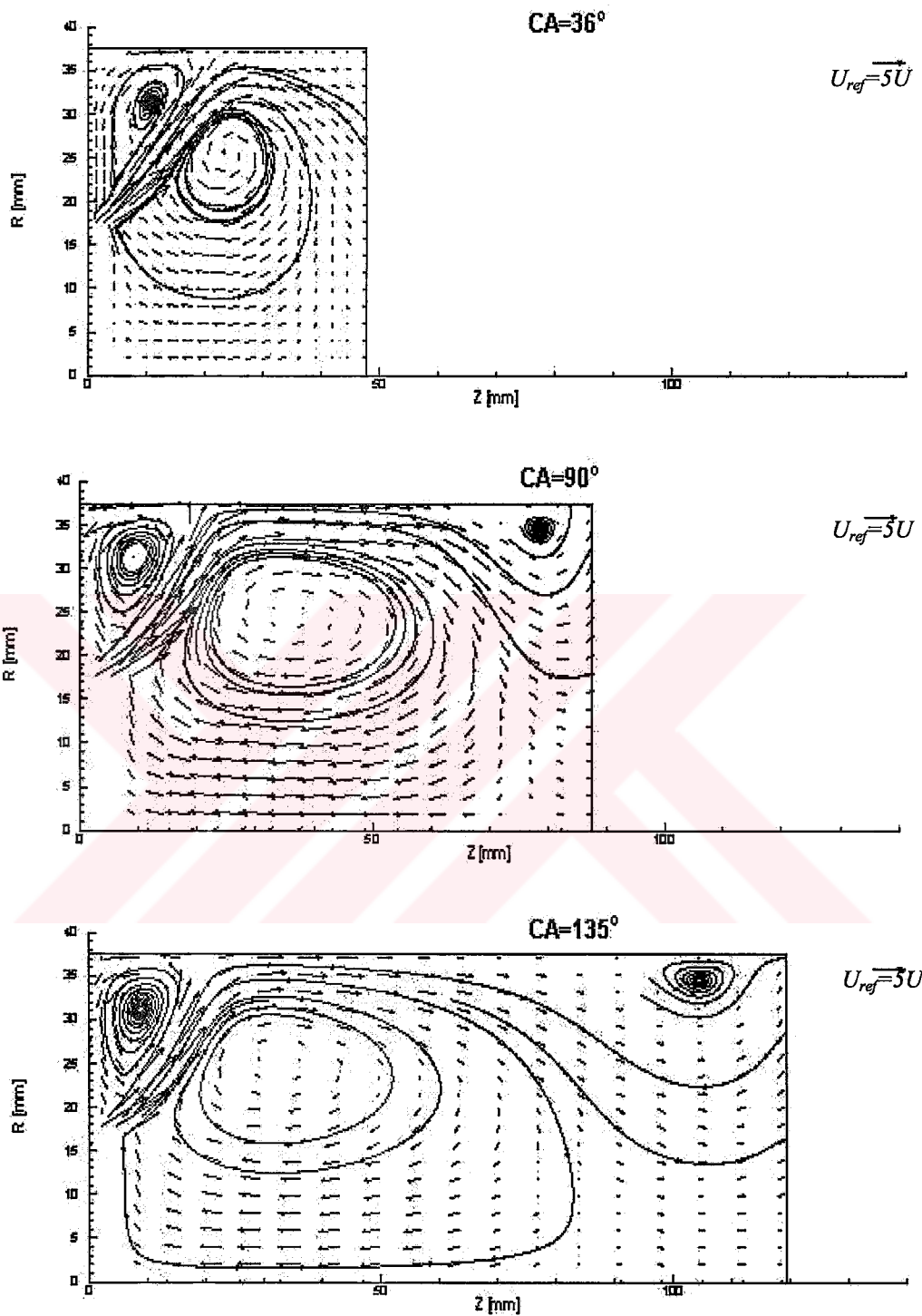


Figure VI.4 Velocity field predictions of the *MM k-ε* model for test Case I at various crank angles in particle tracking and vector plots

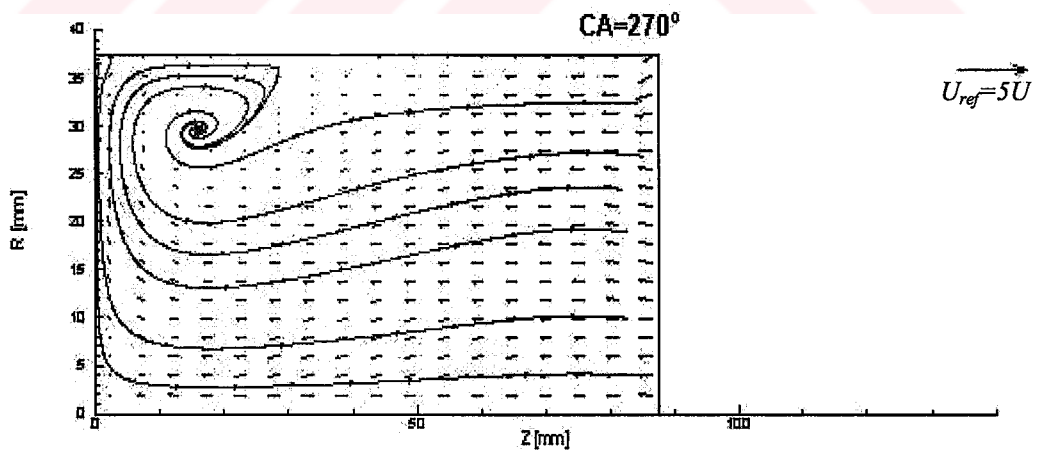
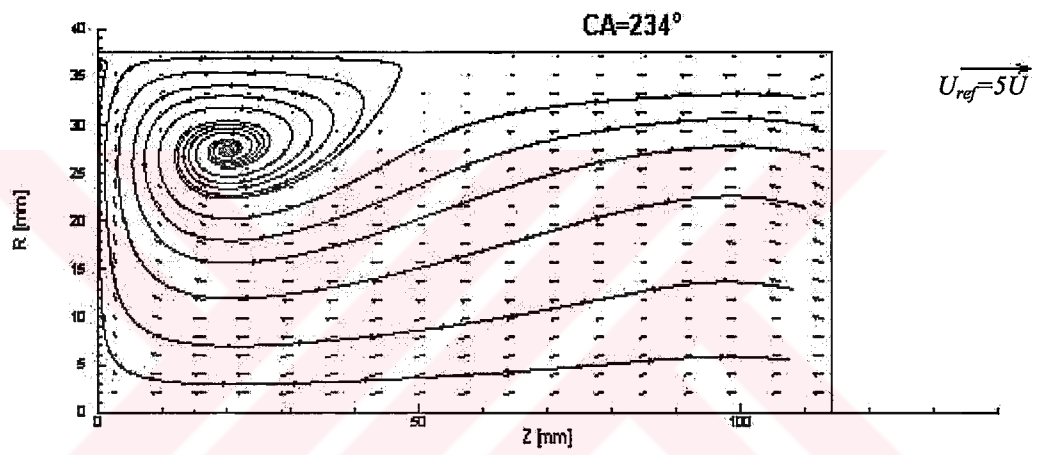
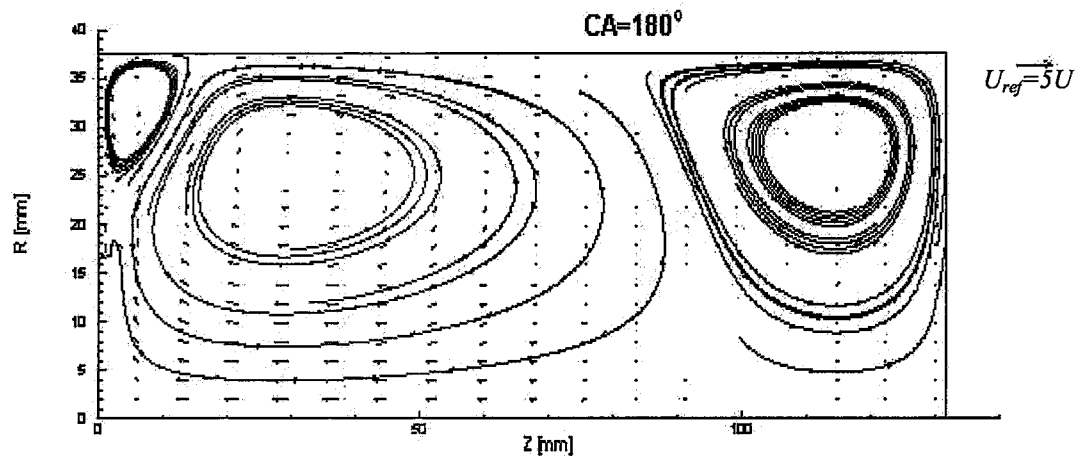


Figure VI.4 Continued

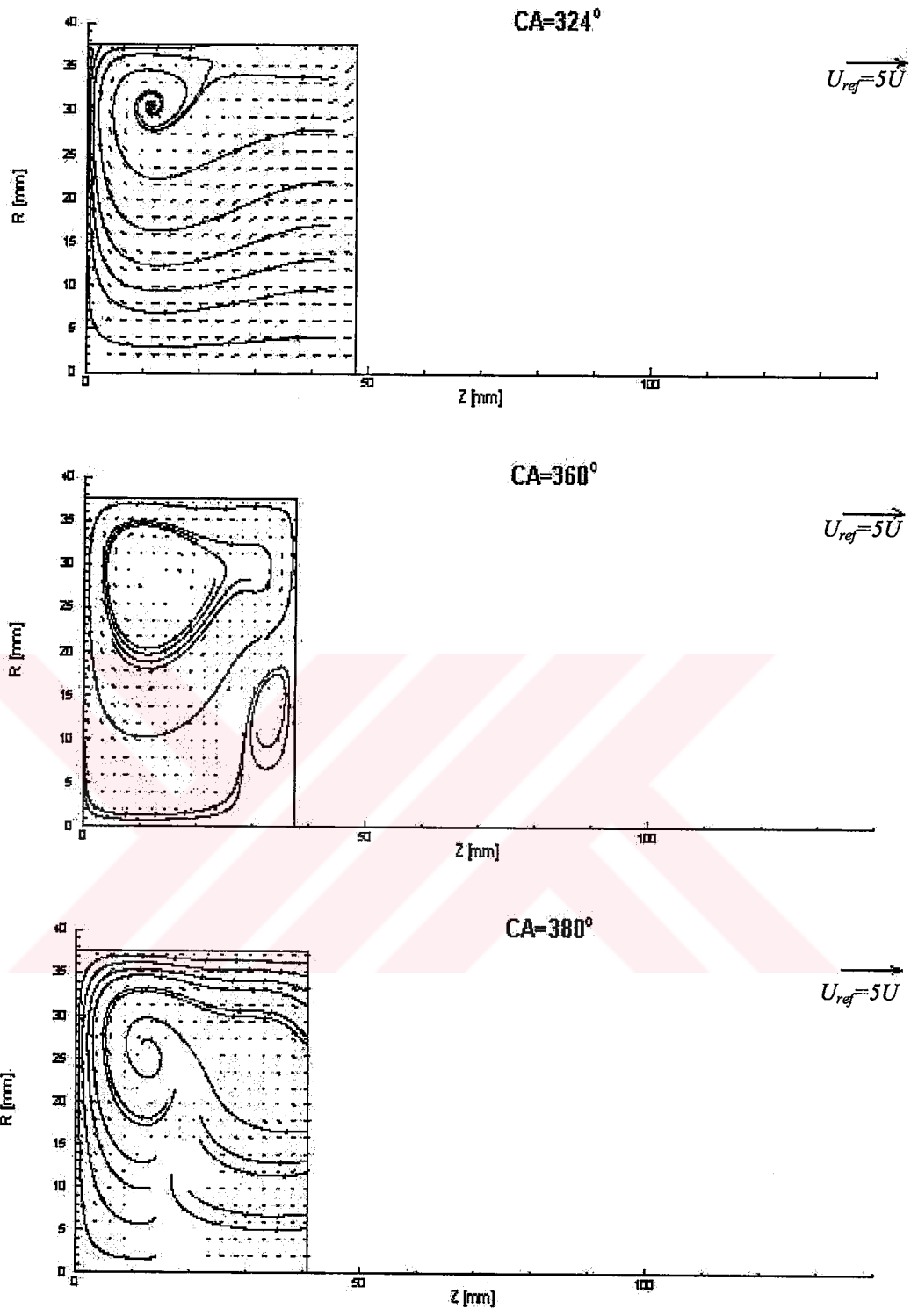


Figure VI.4 Continued

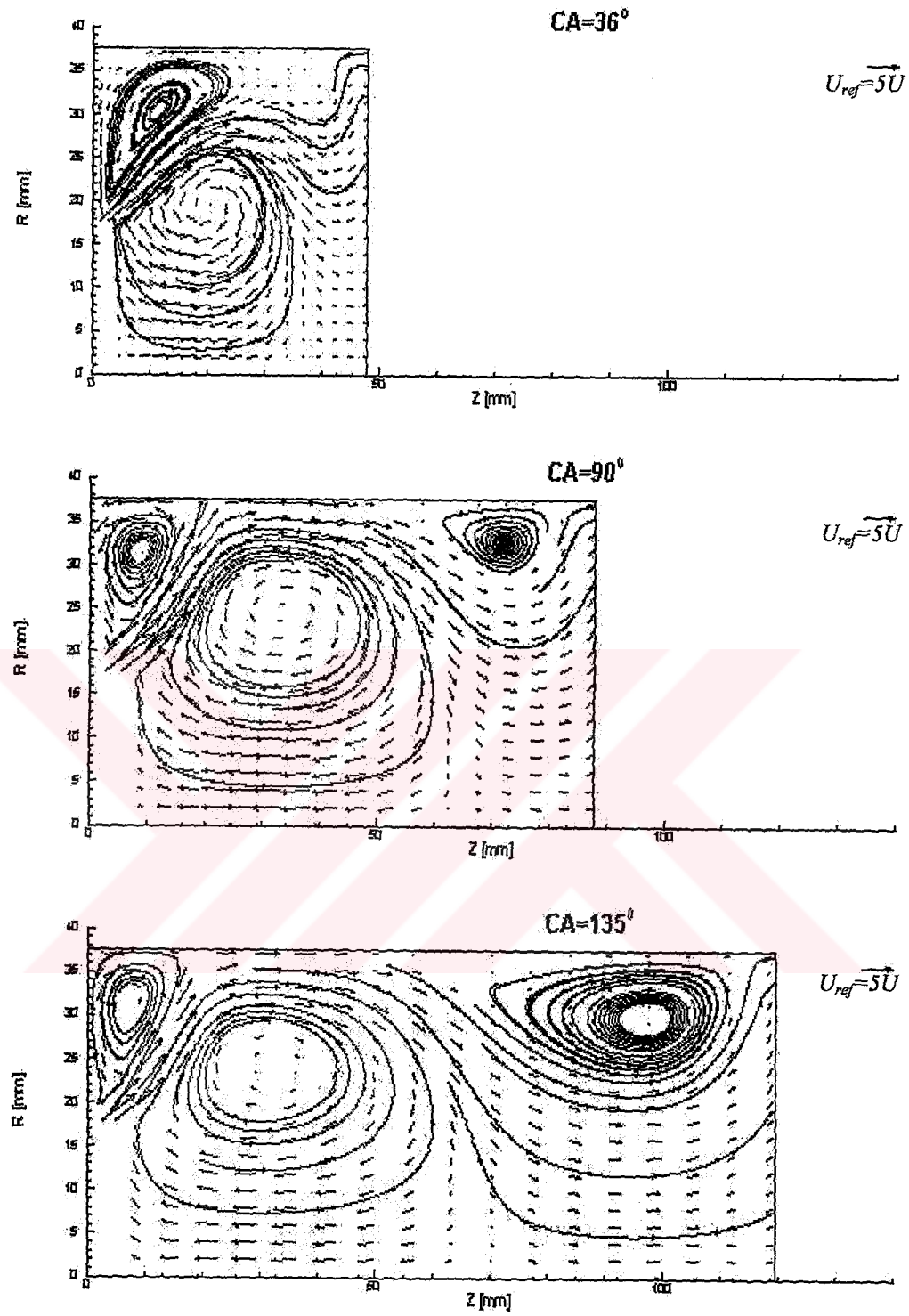


Figure VI.5 Velocity field predictions of the $k-\epsilon-\tau$ model for test Case I at various crank angles in particle tracking and vector plots

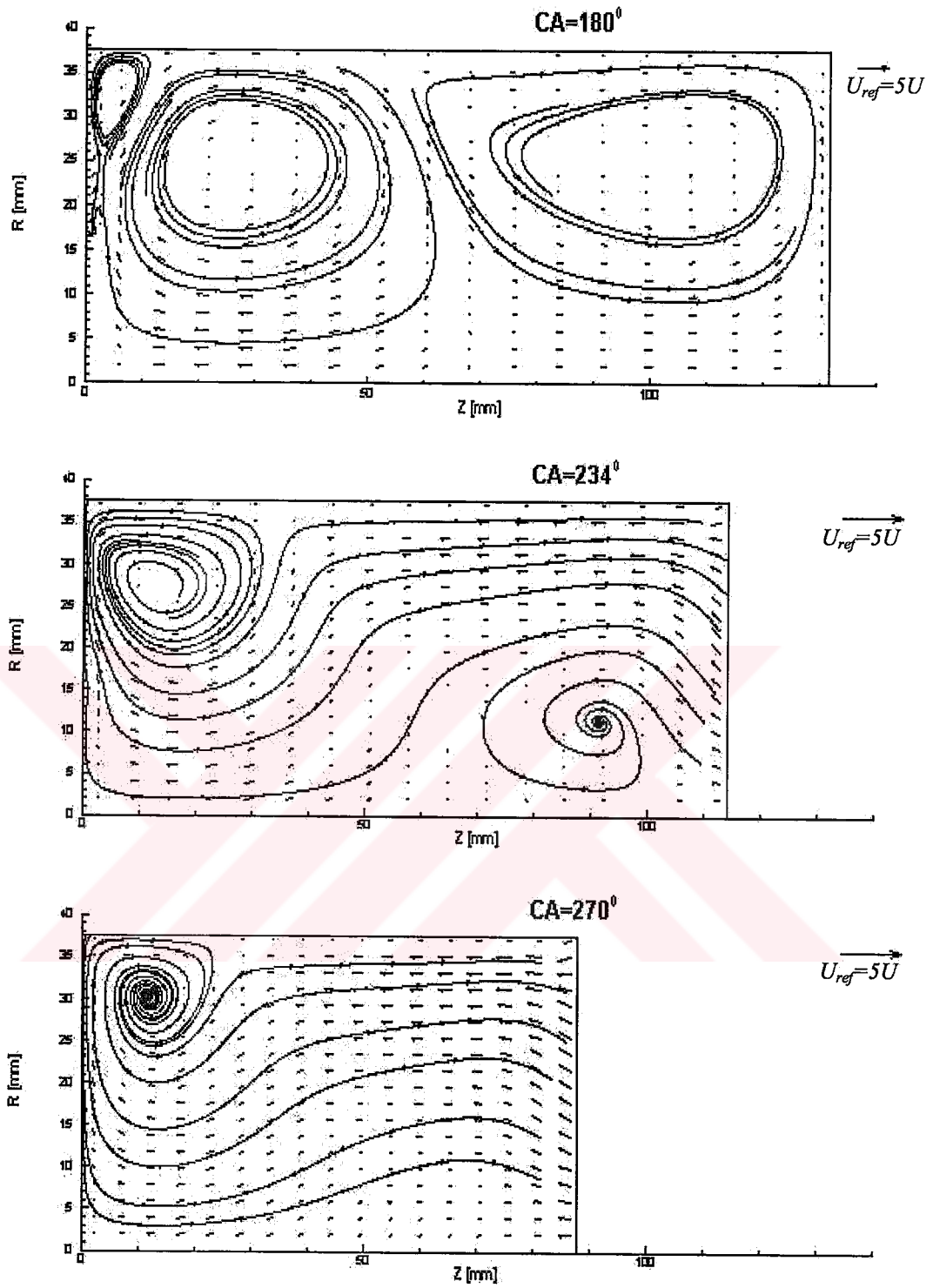


Figure VI.5 Continued

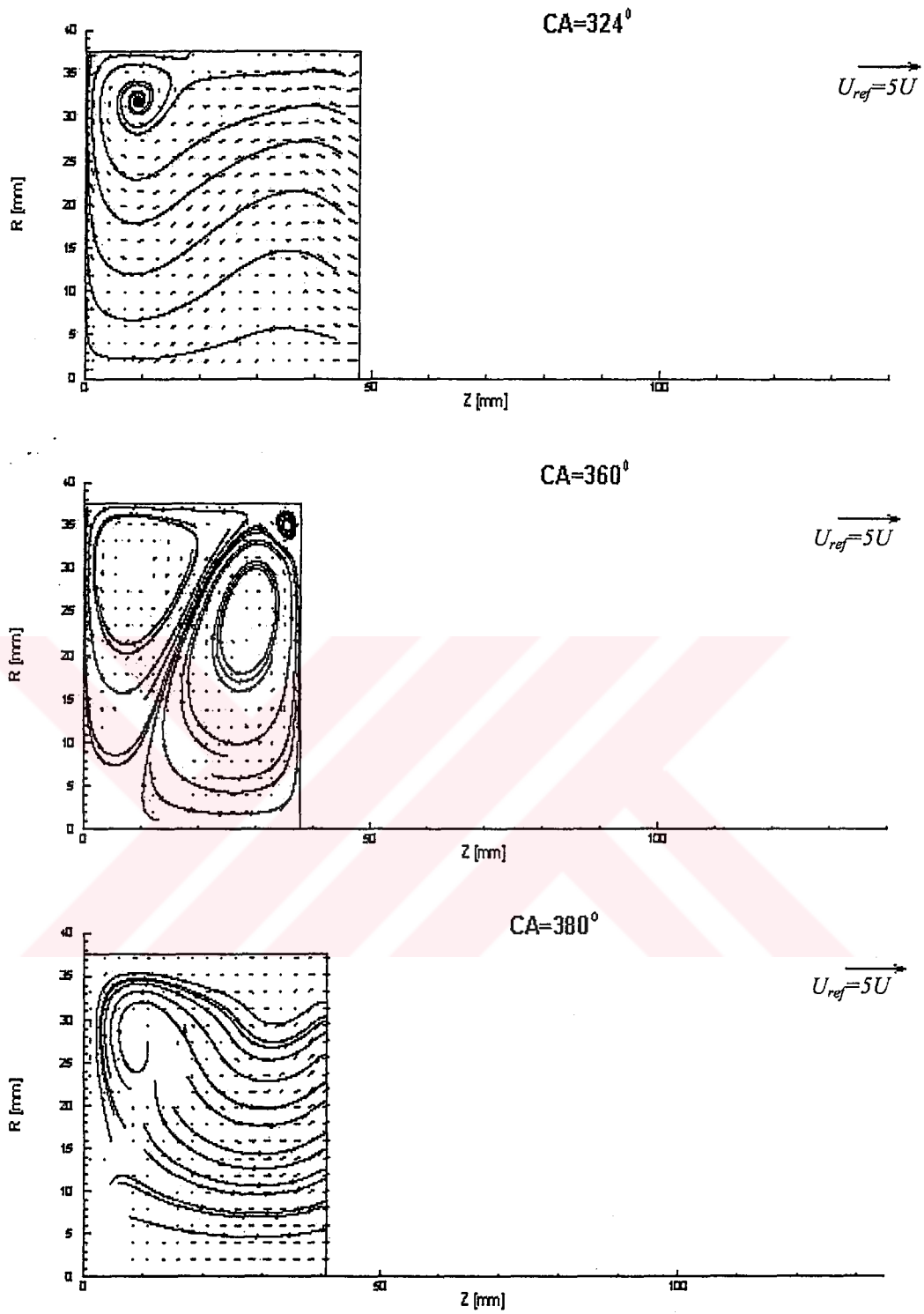


Figure VI.5 Continued

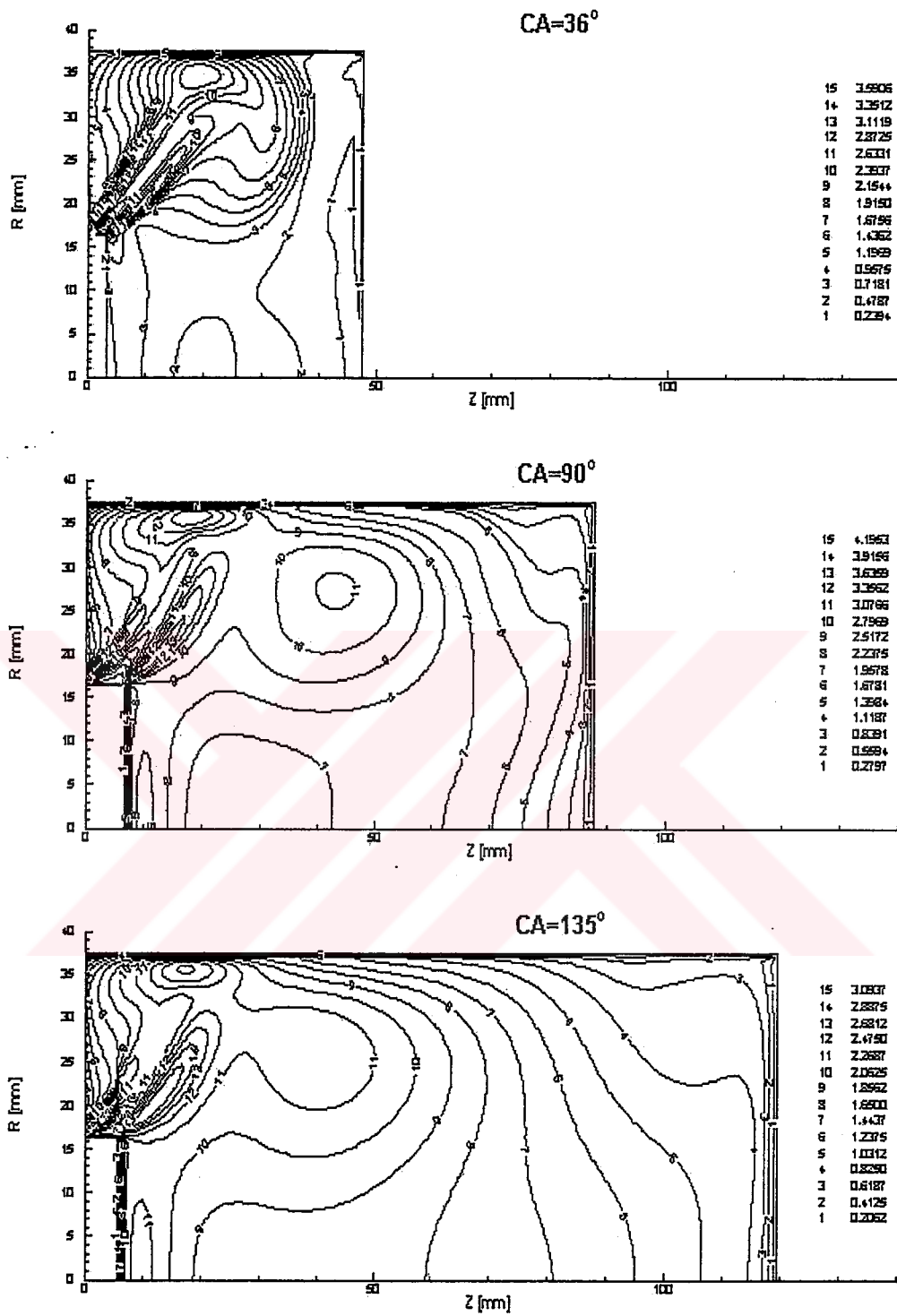


Figure VI.6 Turbulence intensity distributions, predicted by the *MM k-ε* model for test Case I at various crank angles in contour plots

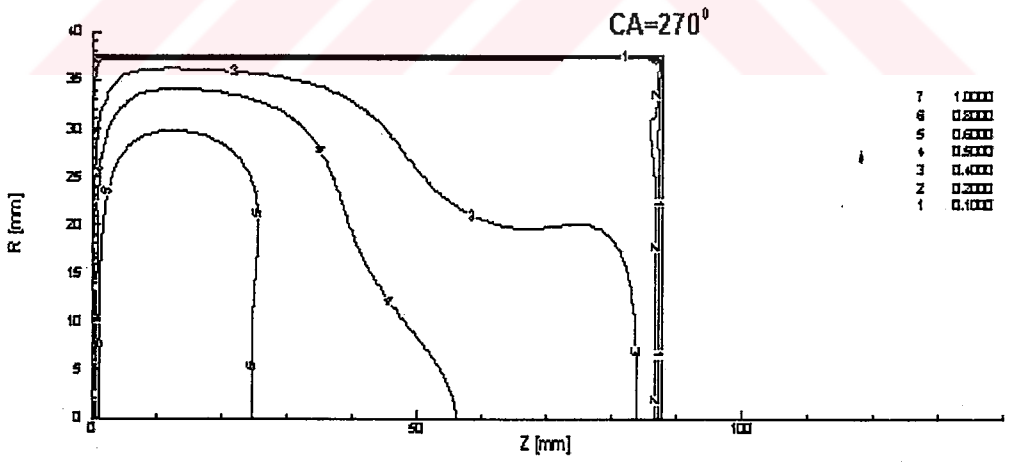
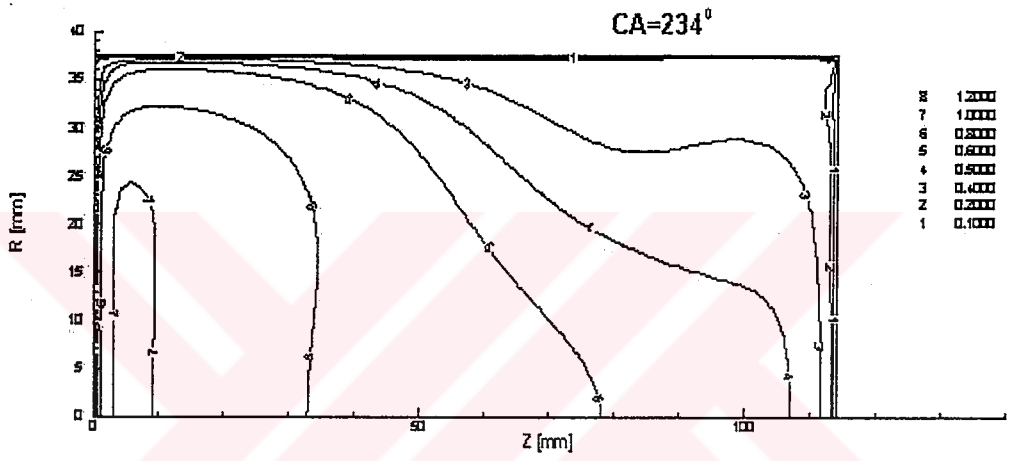
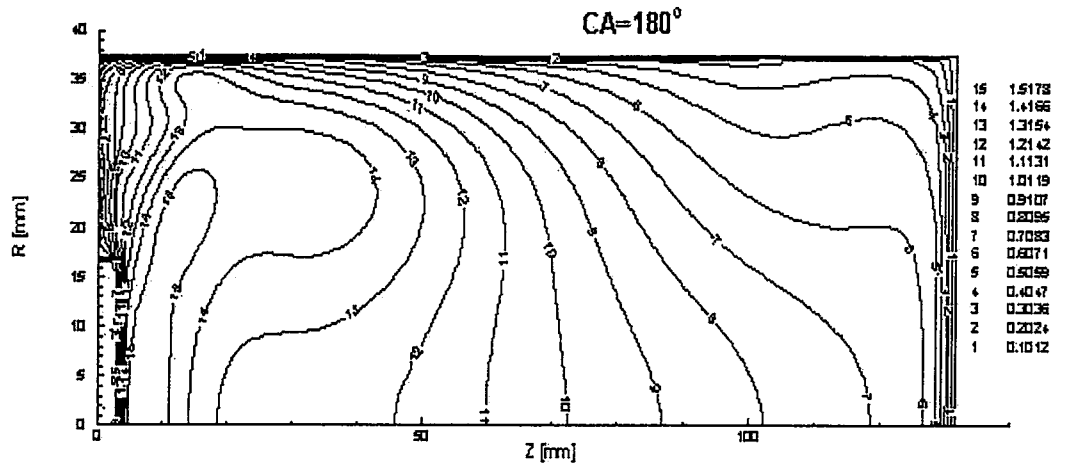


Figure VI.6 Continued

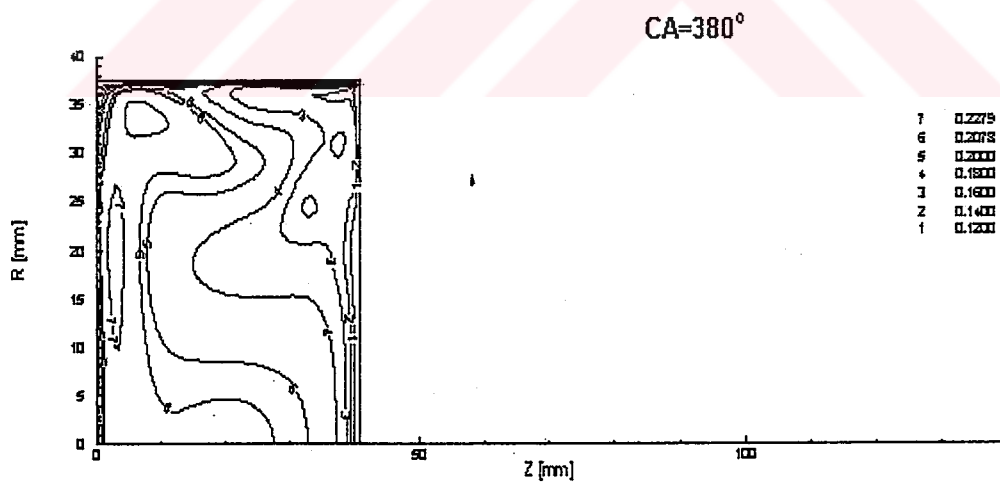
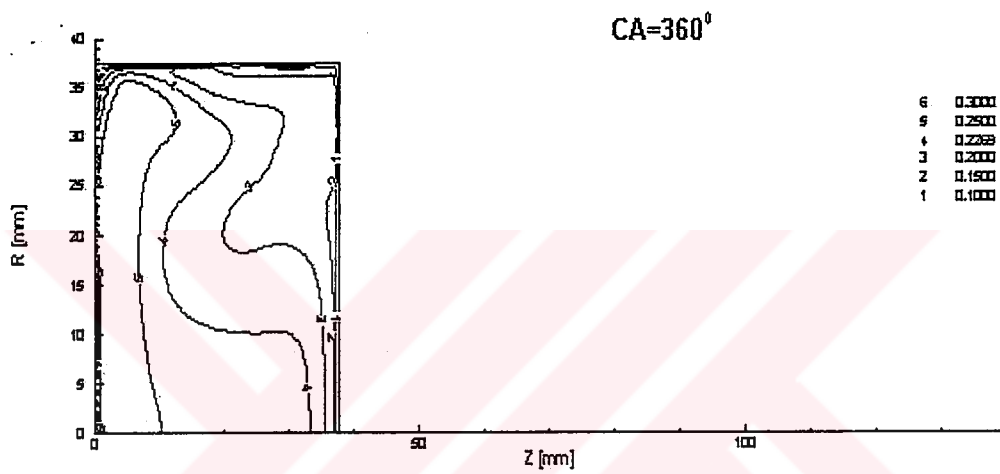
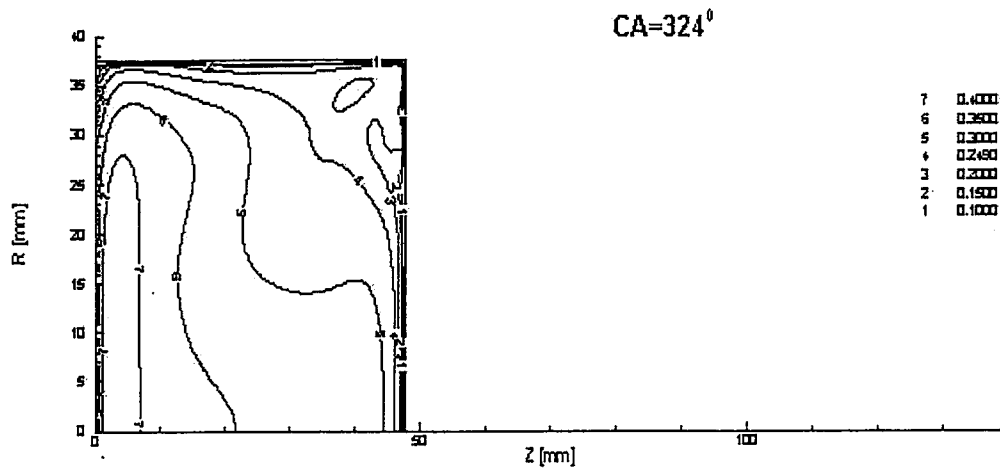


Figure VI.6 Continued

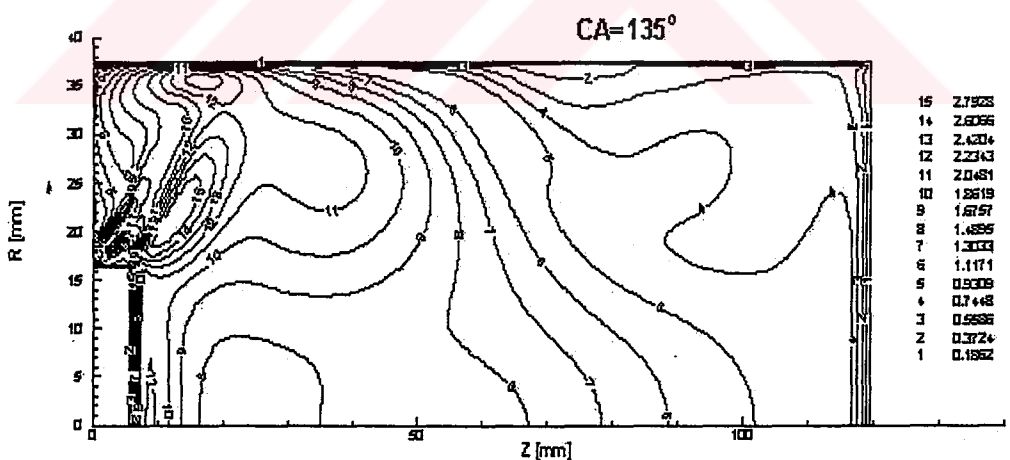
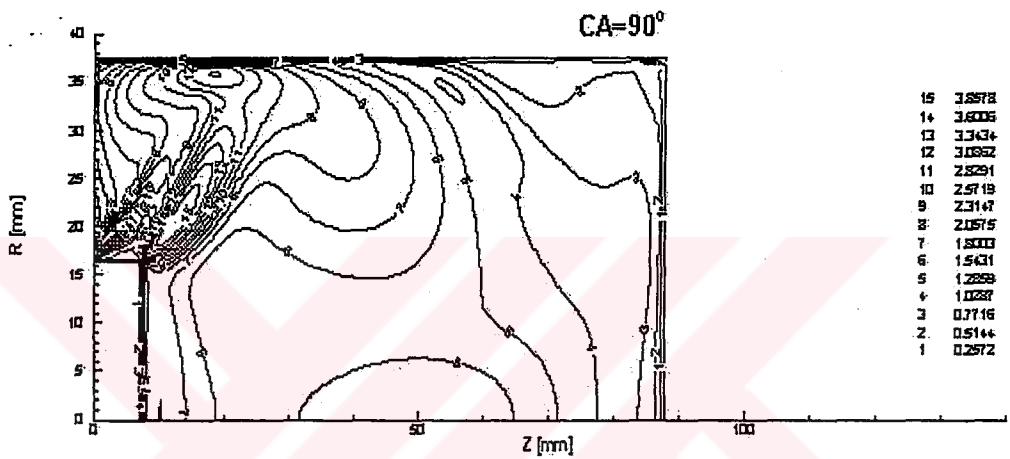
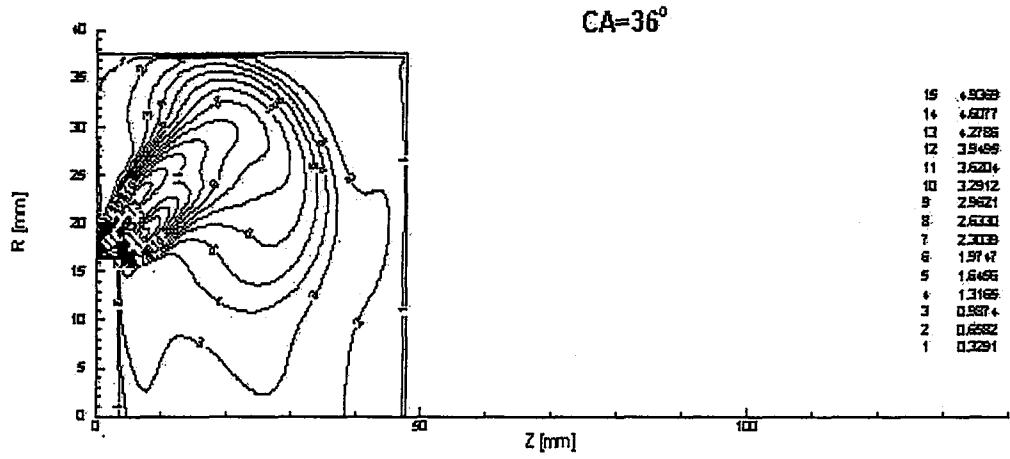


Figure VI.7 Turbulence intensity distributions, predicted by the $k-\epsilon-\tau$ model for test Case I at various crank angles in contour plots

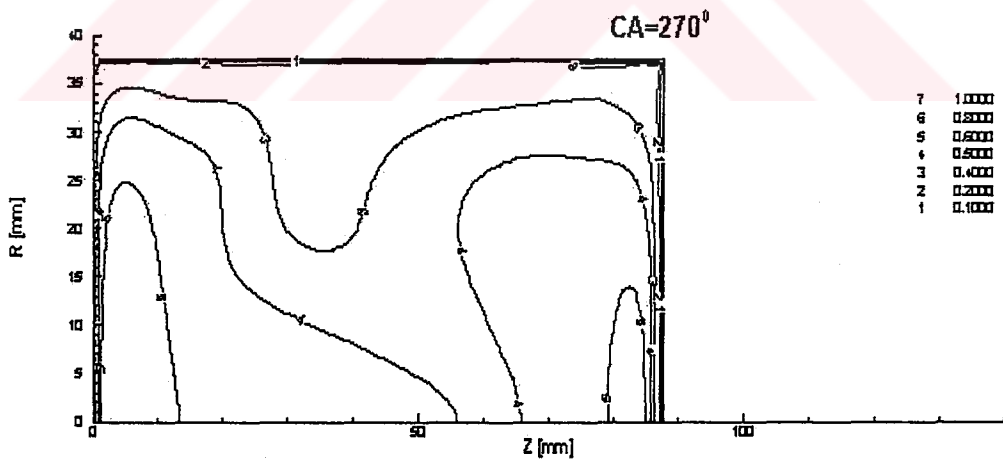
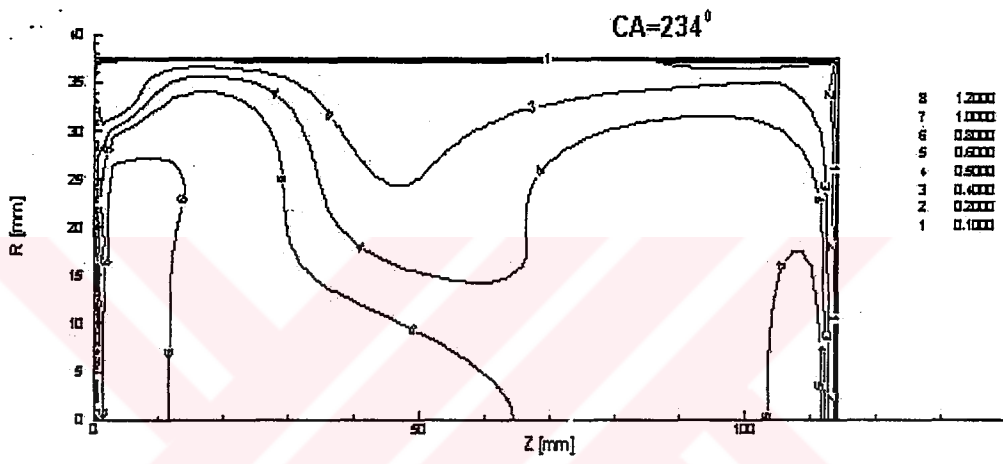
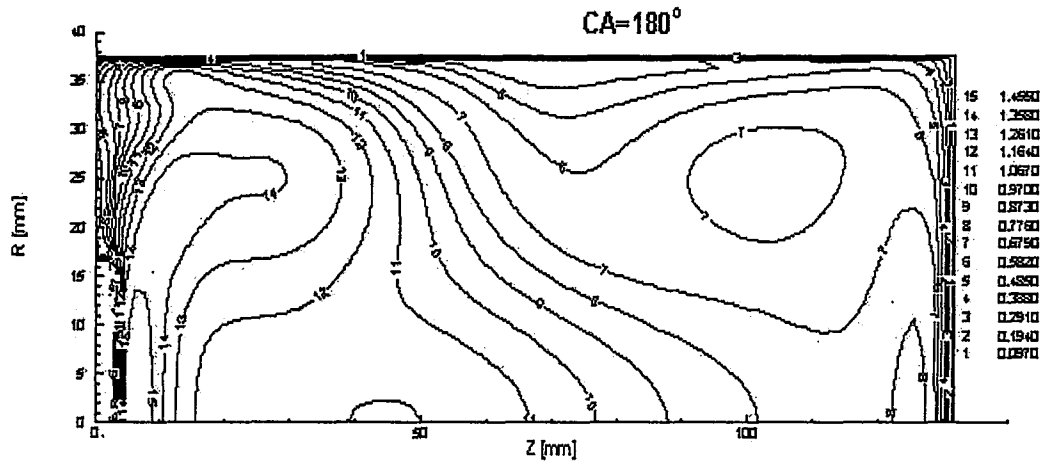


Figure VI.7 Continued

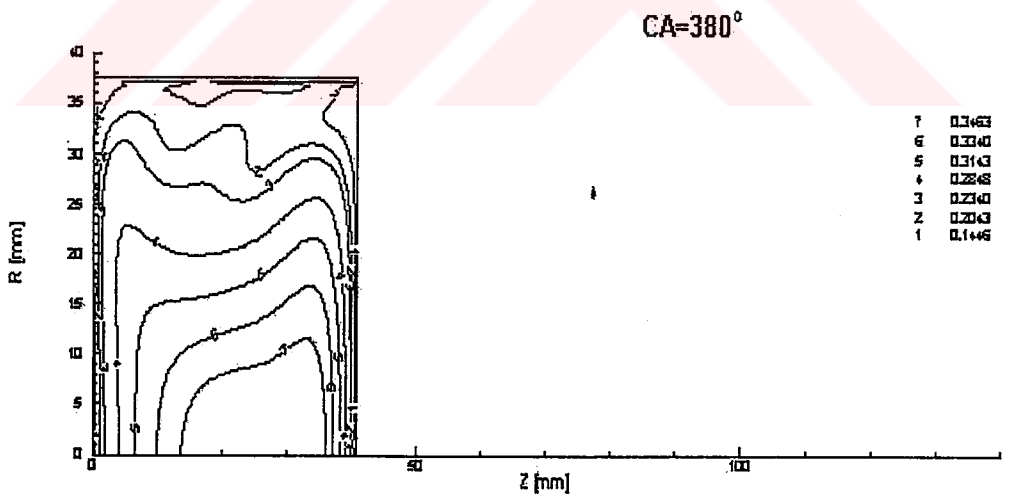
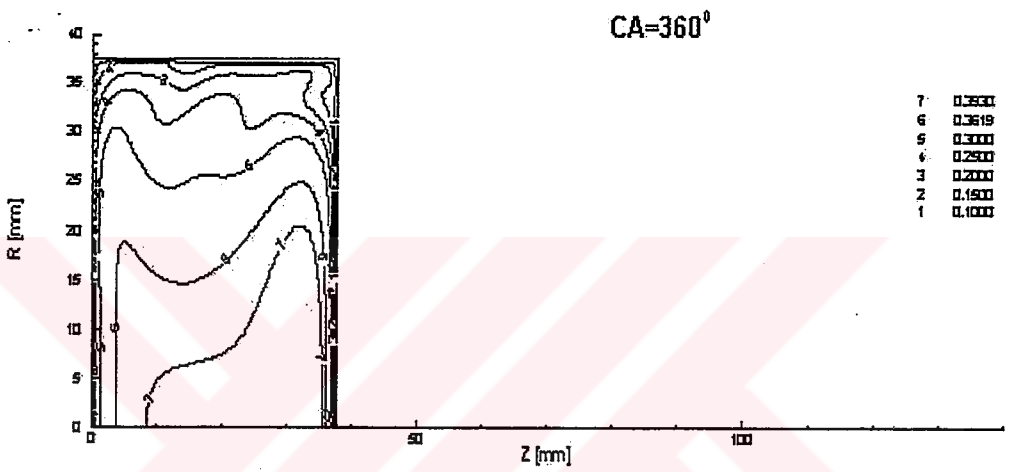
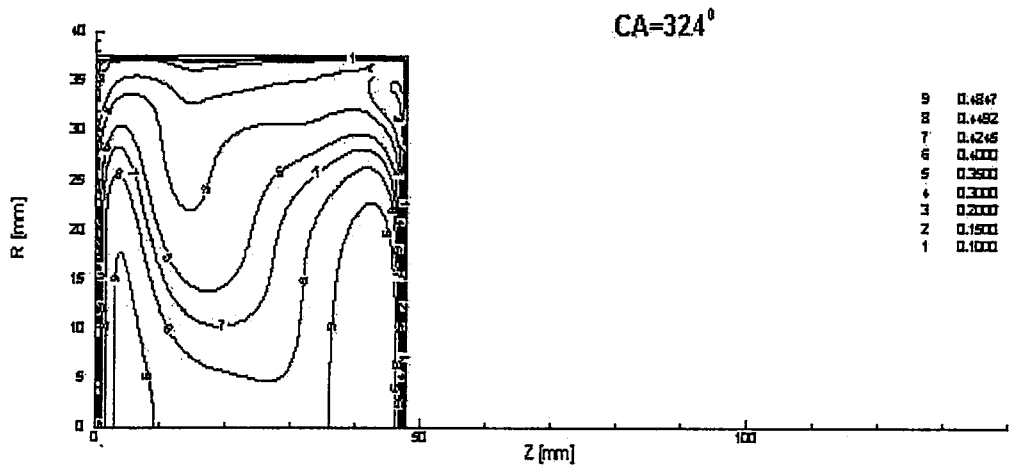


Figure VI.7 Continued

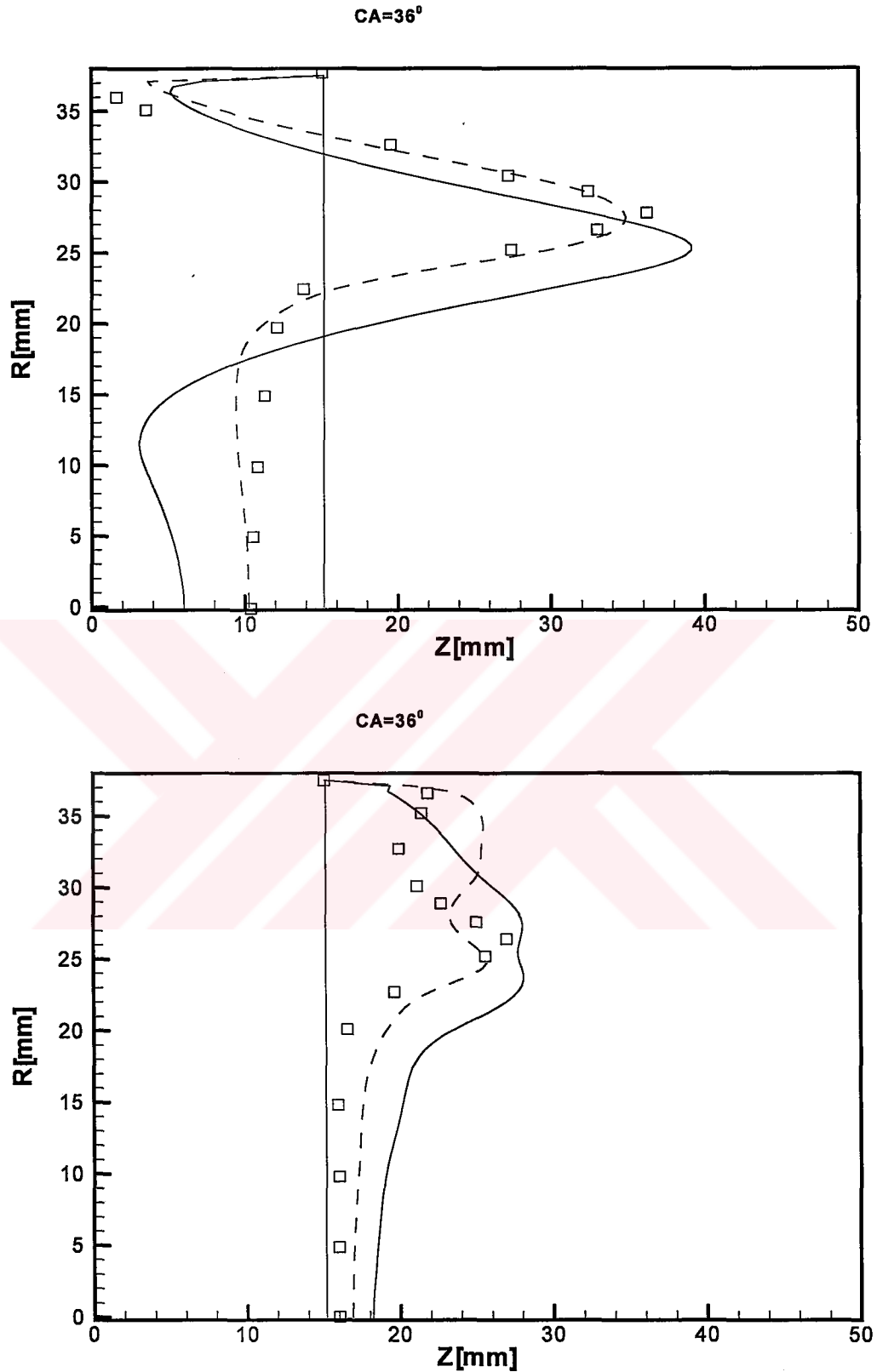


Figure VI.8 The comparison of measured and predicted profiles of axial mean velocity and turbulence intensity for axial location of $z=15$ mm at $CA=36^\circ$; test Case I. (Full line: $k-\epsilon-\tau$ model dashed line: $k-\epsilon$ model symbols: measurements.)

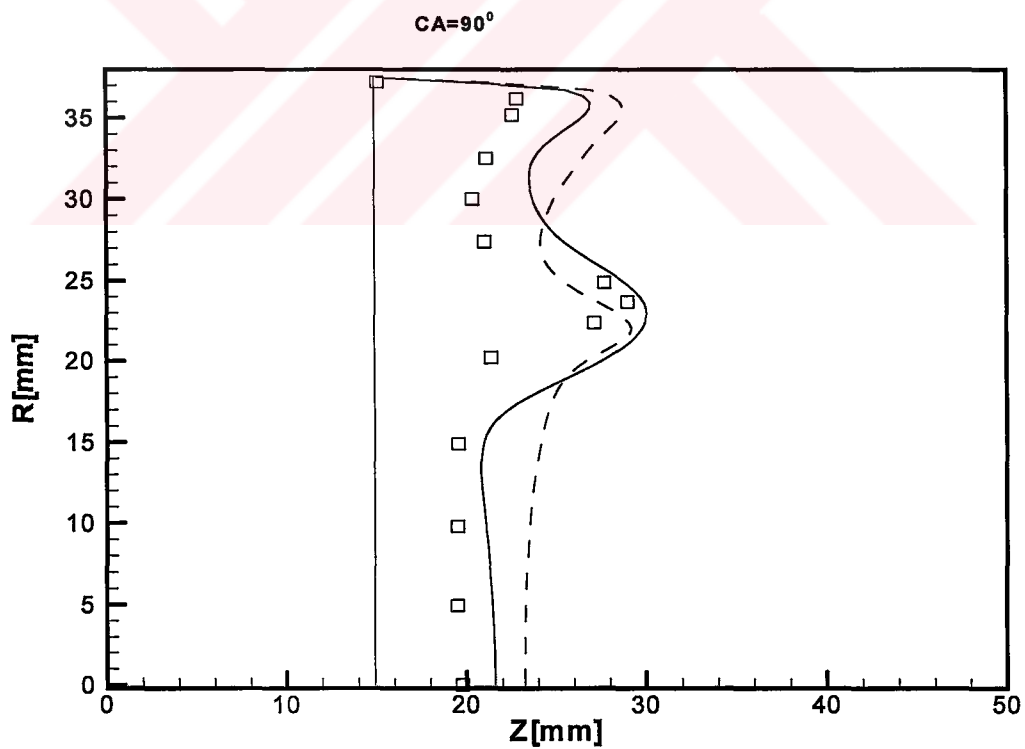
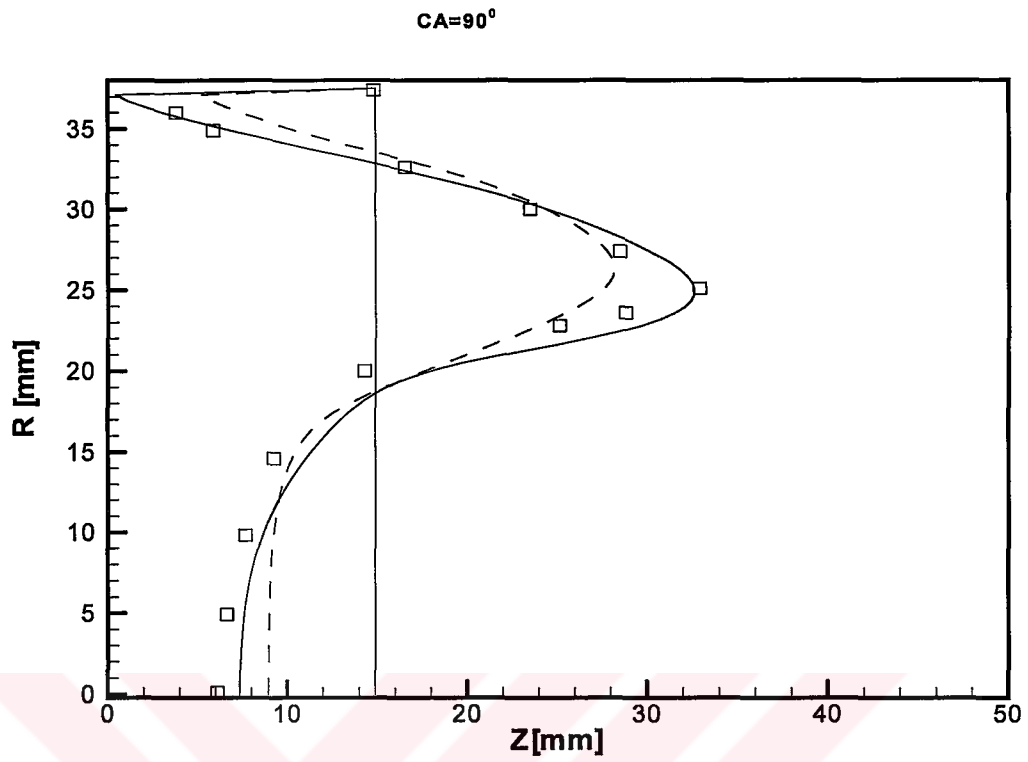


Figure VI.9 The comparison of measured and predicted profiles of axial mean velocity and turbulence intensity for axial location of $z=15$ mm at $CA=90^\circ$; test Case I. (Full line: $k-\epsilon-\tau$ model dashed line: $k-\epsilon$ model symbols: measurements.)

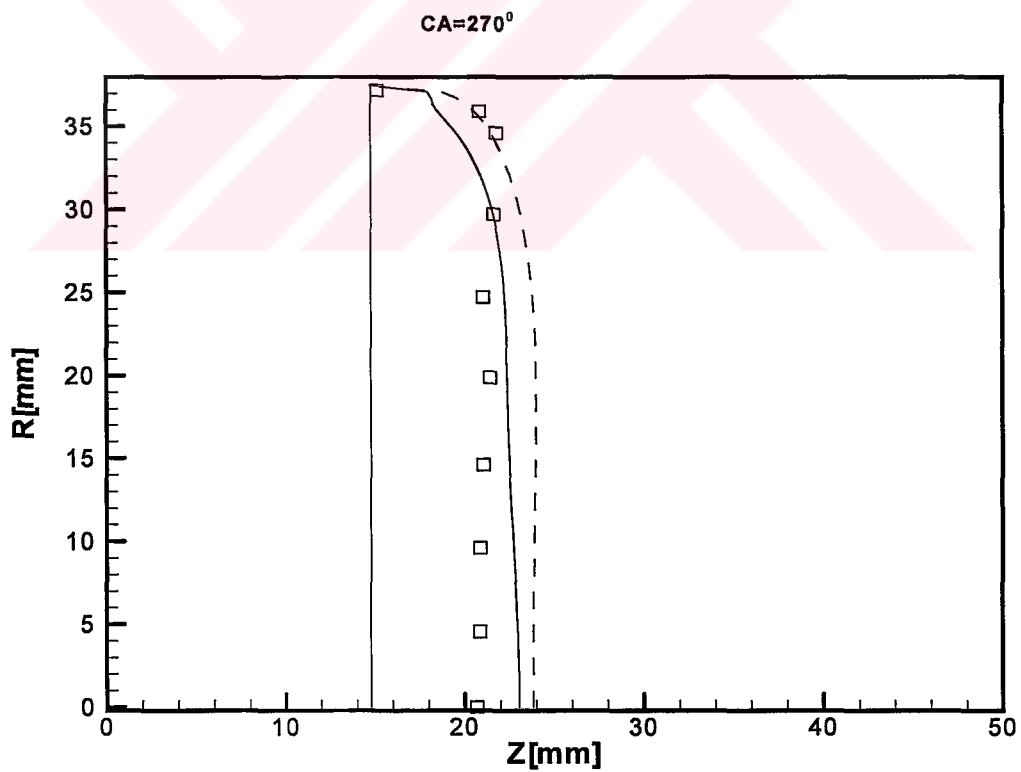
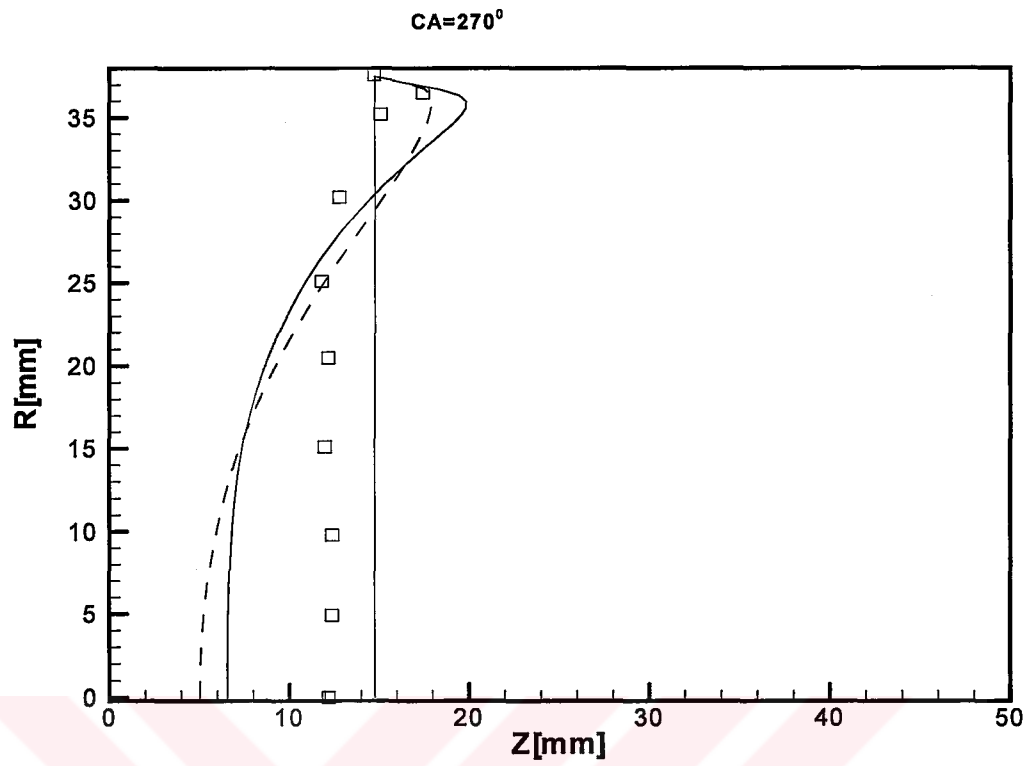
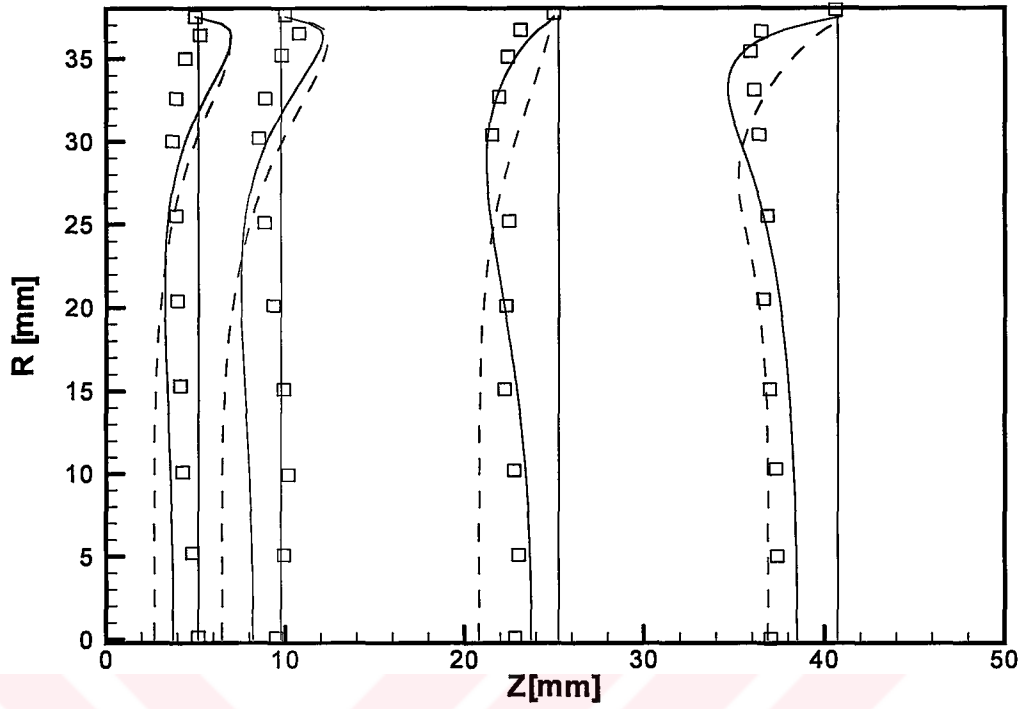


Figure VI.10 The comparison of measured and predicted profiles of axial mean velocity and turbulence intensity for axial location of $z=15$ mm at $CA=270^\circ$; test Case I. (Full line: $k-\epsilon-\tau$ model dashed line: $k-\epsilon$ model symbols: measurements.)

CA=324°



CA=324°

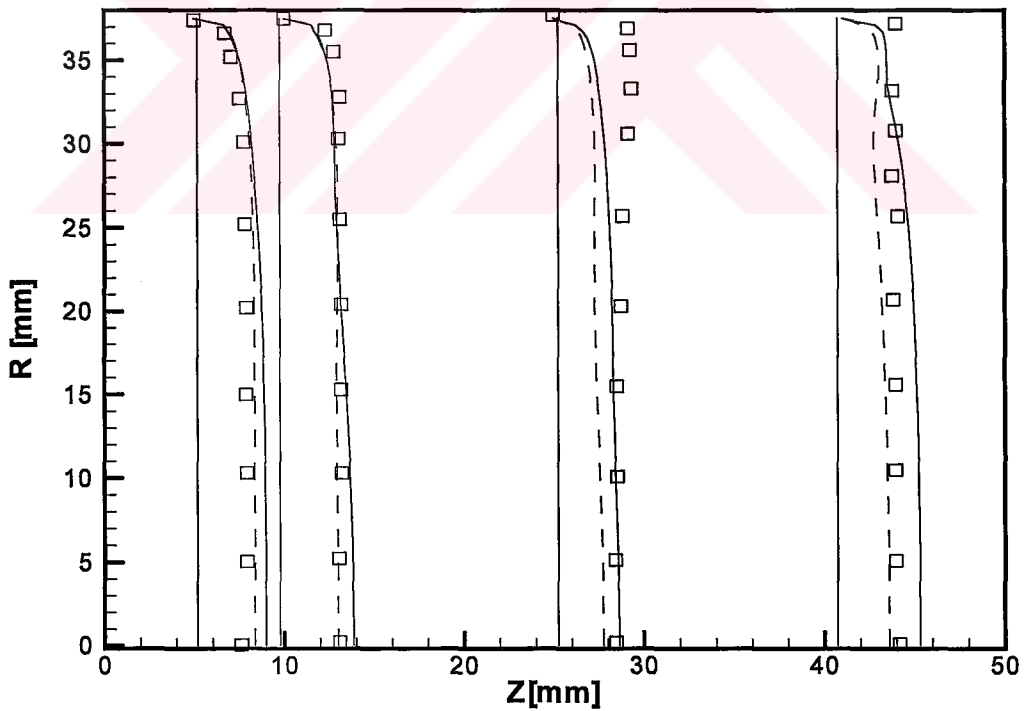


Figure VI.11 The comparison of measured and predicted profiles of axial mean velocity and turbulence intensity for axial location of $z=5, 10, 25$ and 41 mm at $CA=324^\circ$; test Case I. (Full line: $k-\epsilon-\tau$ model dashed line: $k-\epsilon$ model symbols: measurements.)

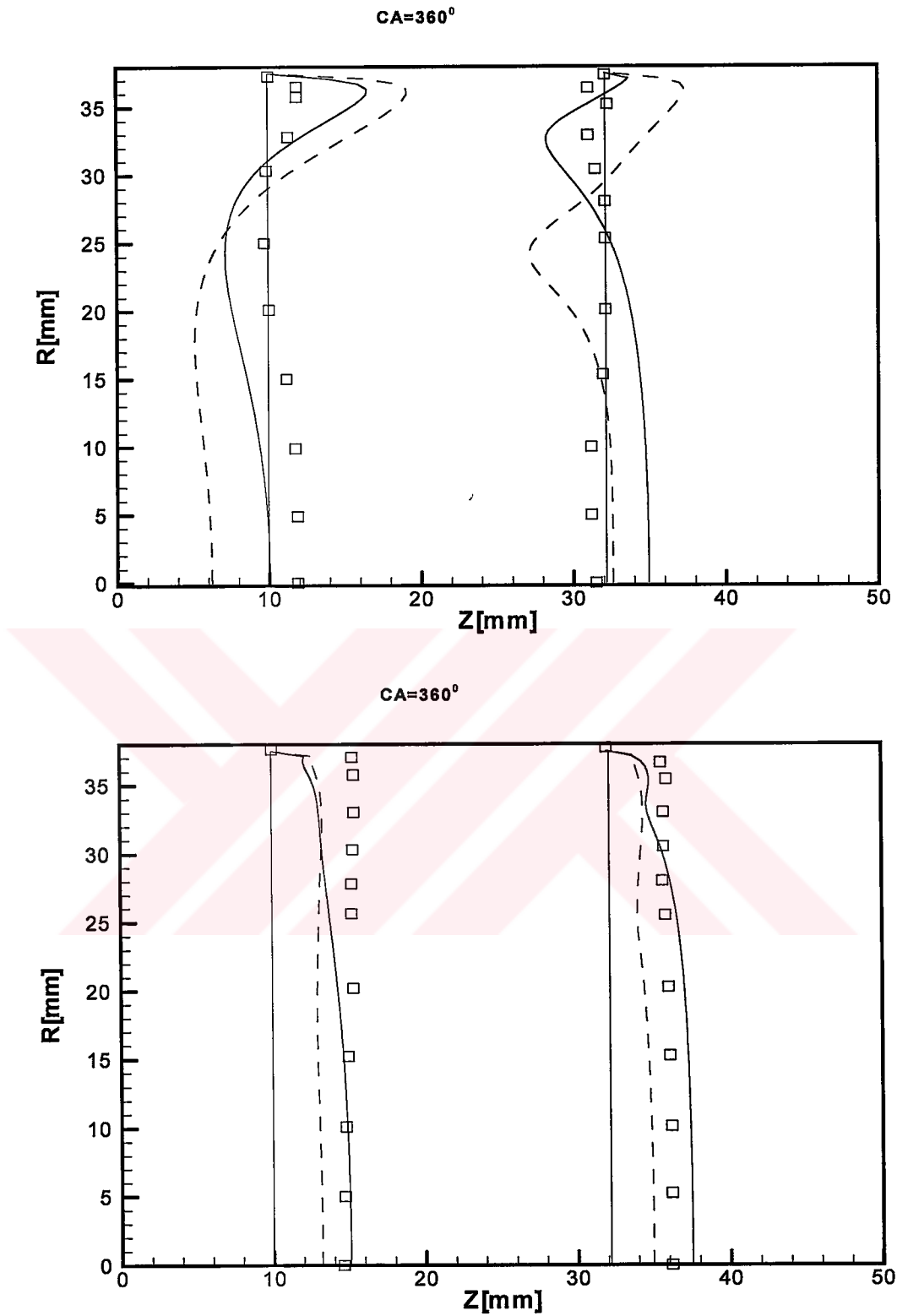


Figure VI.12 The comparison of measured and predicted profiles of axial mean velocity and turbulence intensity for axial location of $z=10$ and 32 mm at $CA=360^\circ$; test Case I. (Full line: $k-\epsilon-\tau$ model dashed line: $k-\epsilon$ model symbols: measurements.)

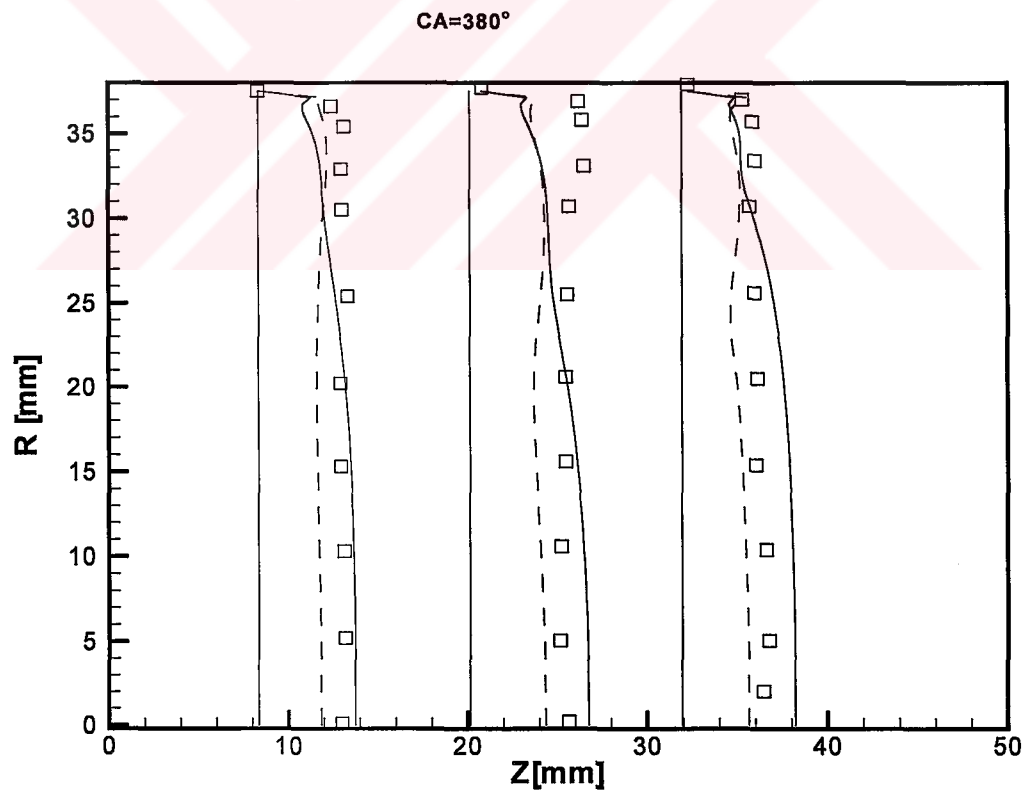
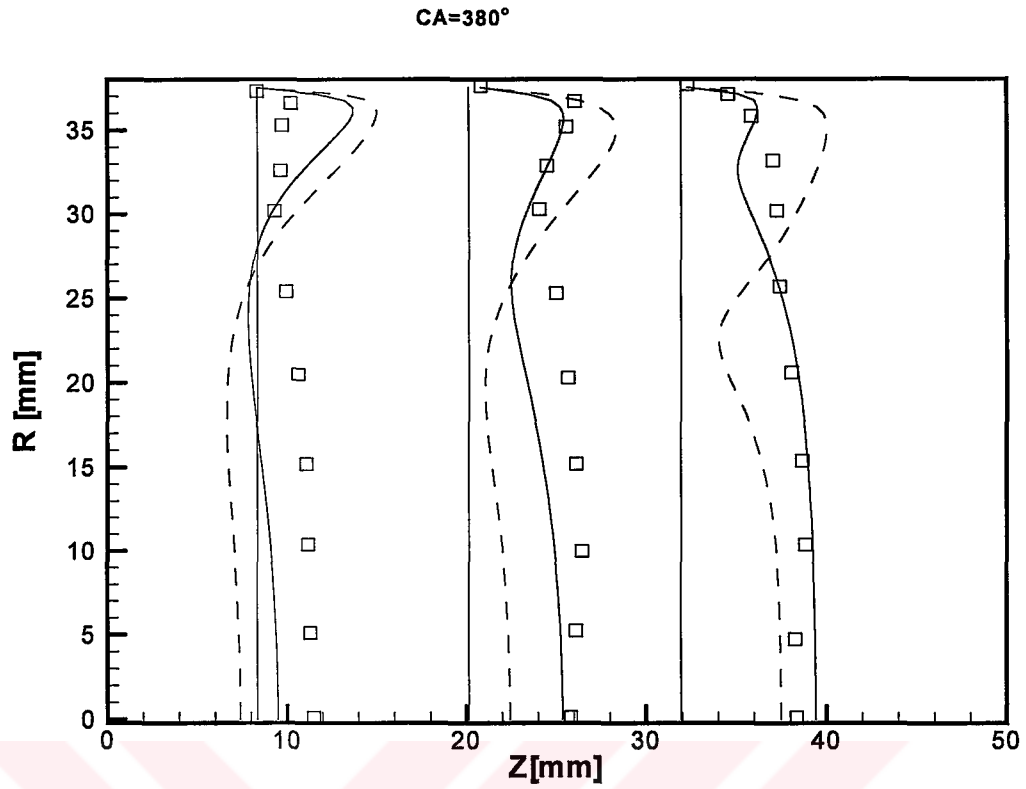


Figure VI.13 The comparison of measured and predicted profiles of axial mean velocity and turbulence intensity for axial location of $z=10$, 20 and 32 mm at $CA=380^\circ$; test Case I. (Full line: $k-\epsilon-\tau$ model dashed line: $k-\epsilon$ model symbols: measurements.)

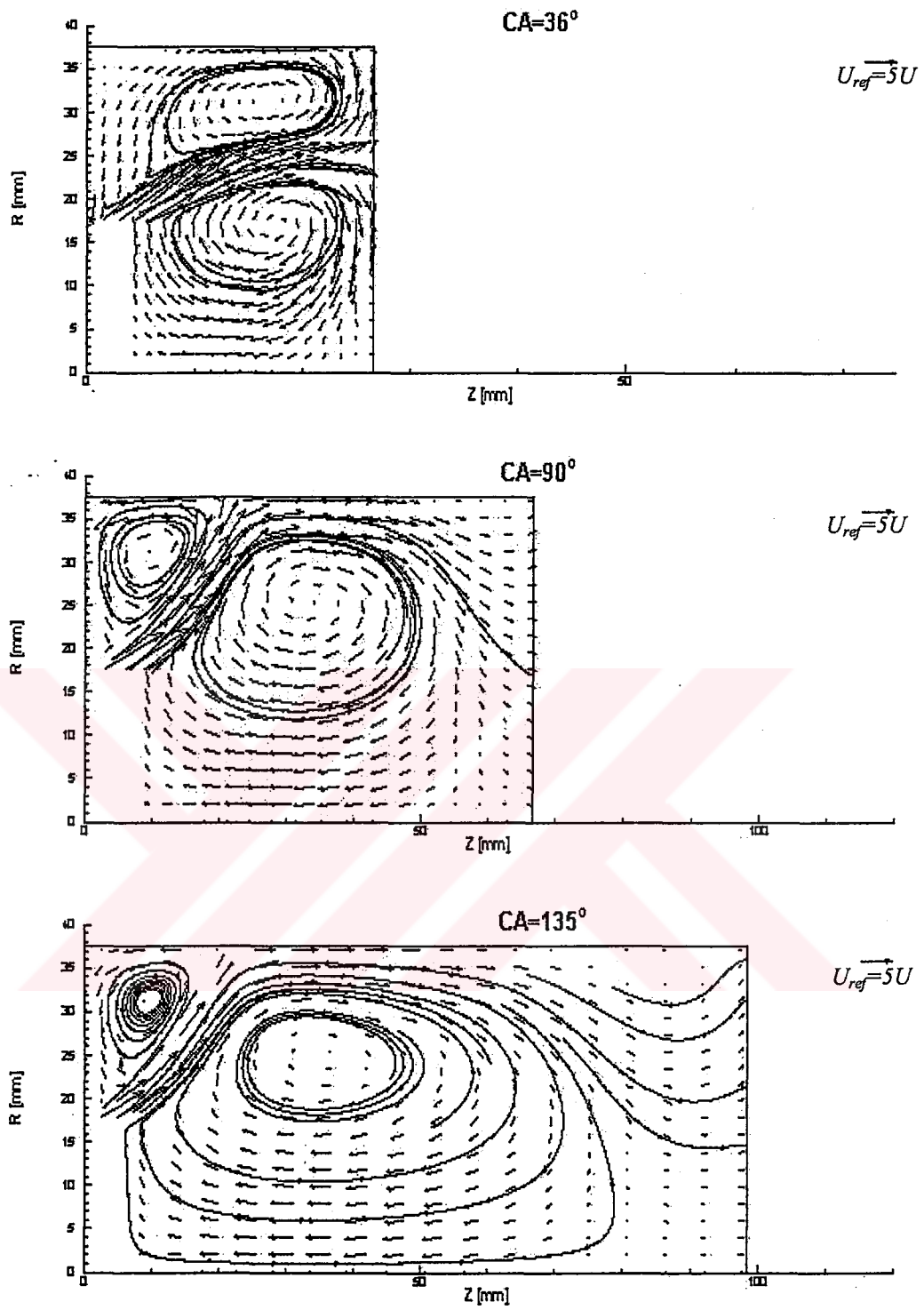


Figure VI.14 Velocity field predictions of the *MM k-ε* model for test Case II at various crank angles in particle tracking and vector plots

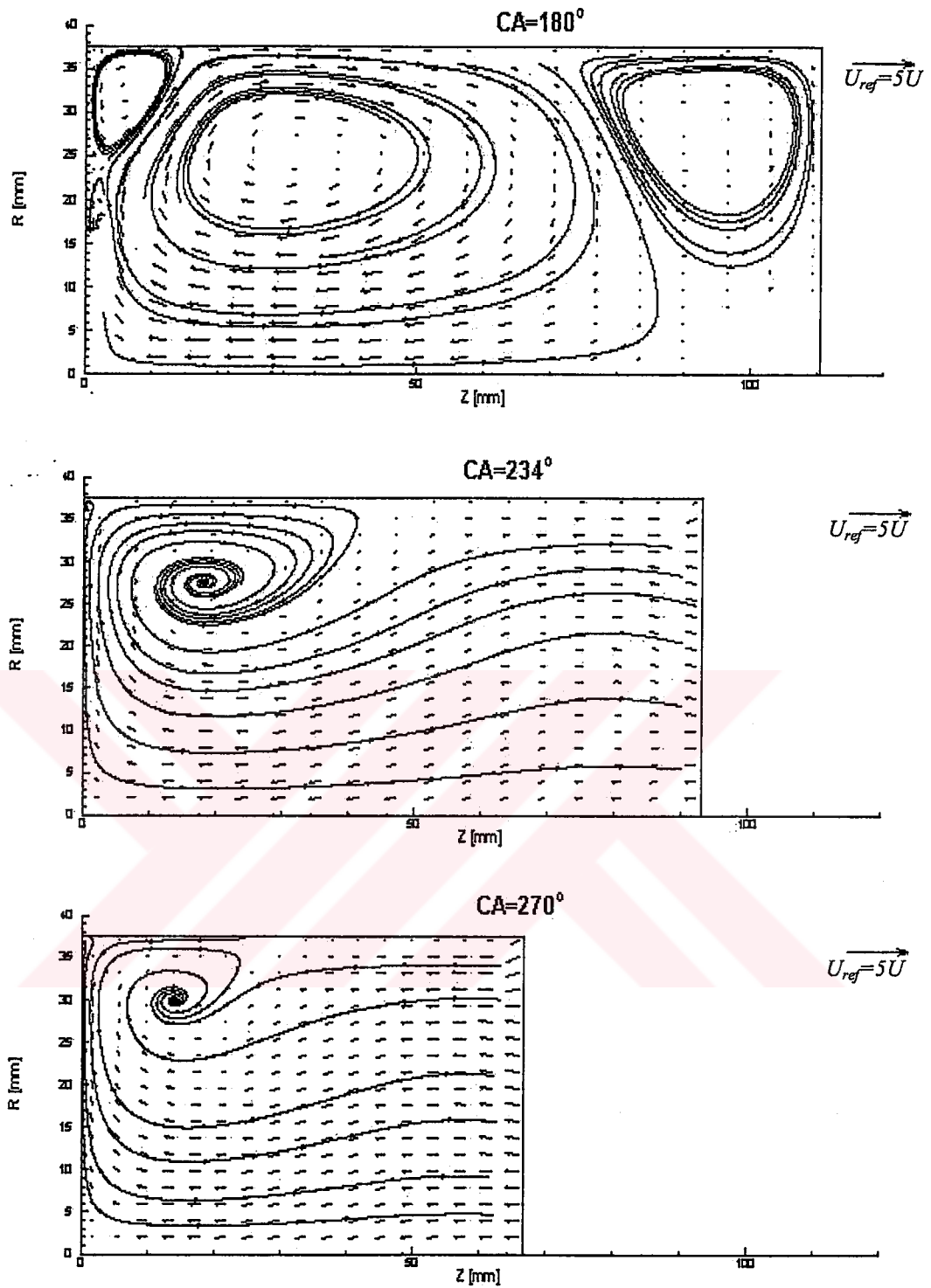


Figure VI.14 Continued

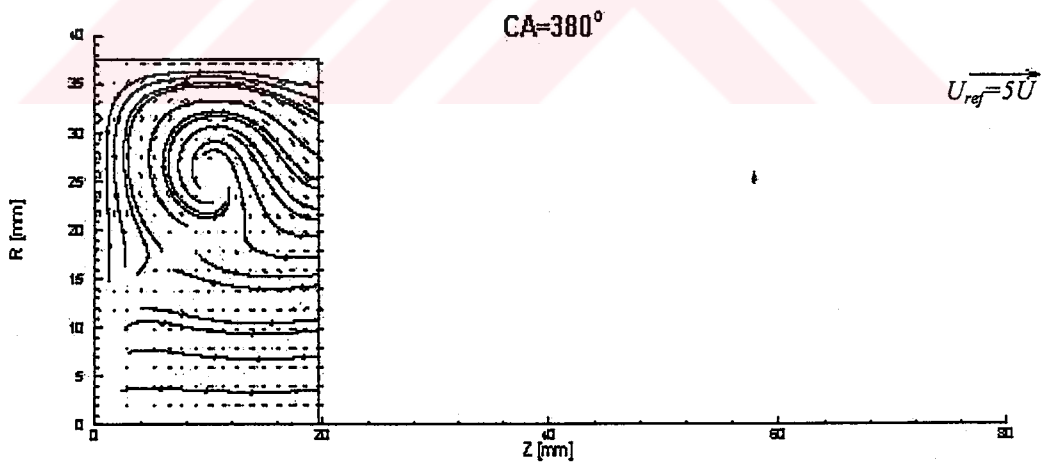
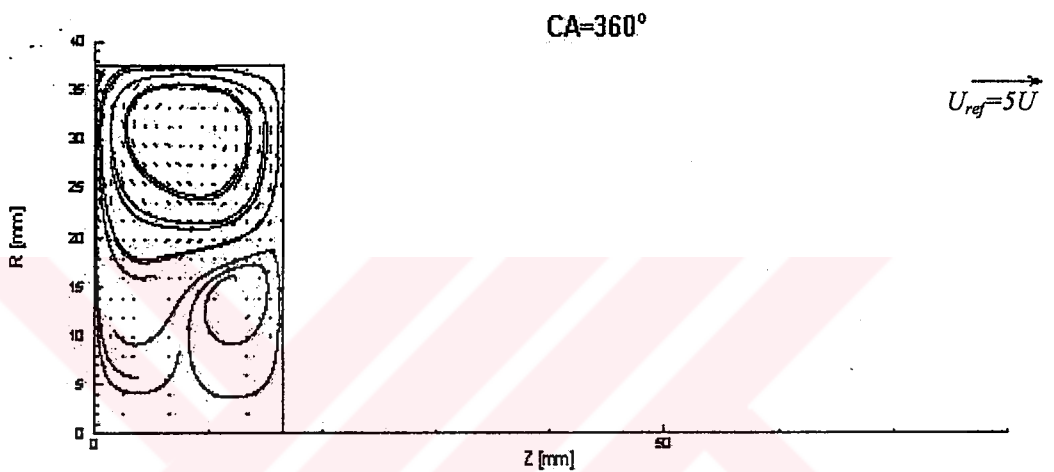
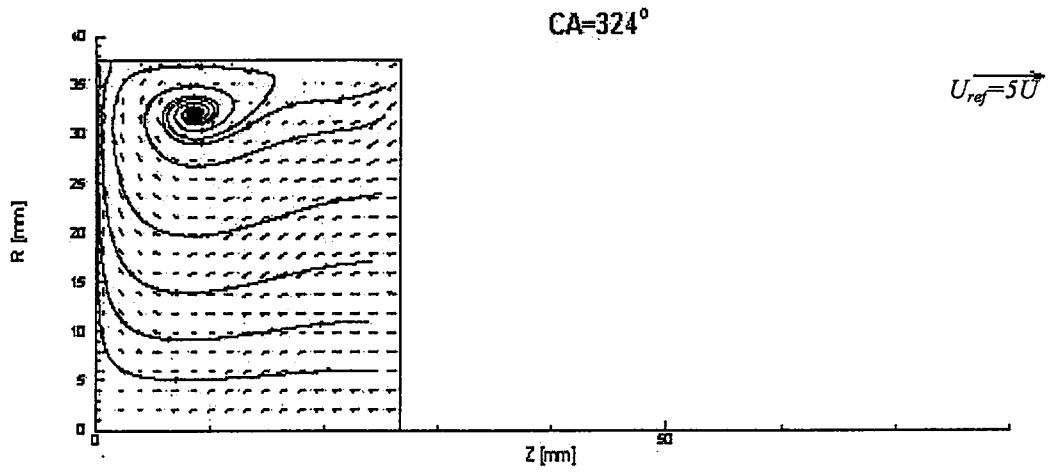


Figure VI.14 Continued

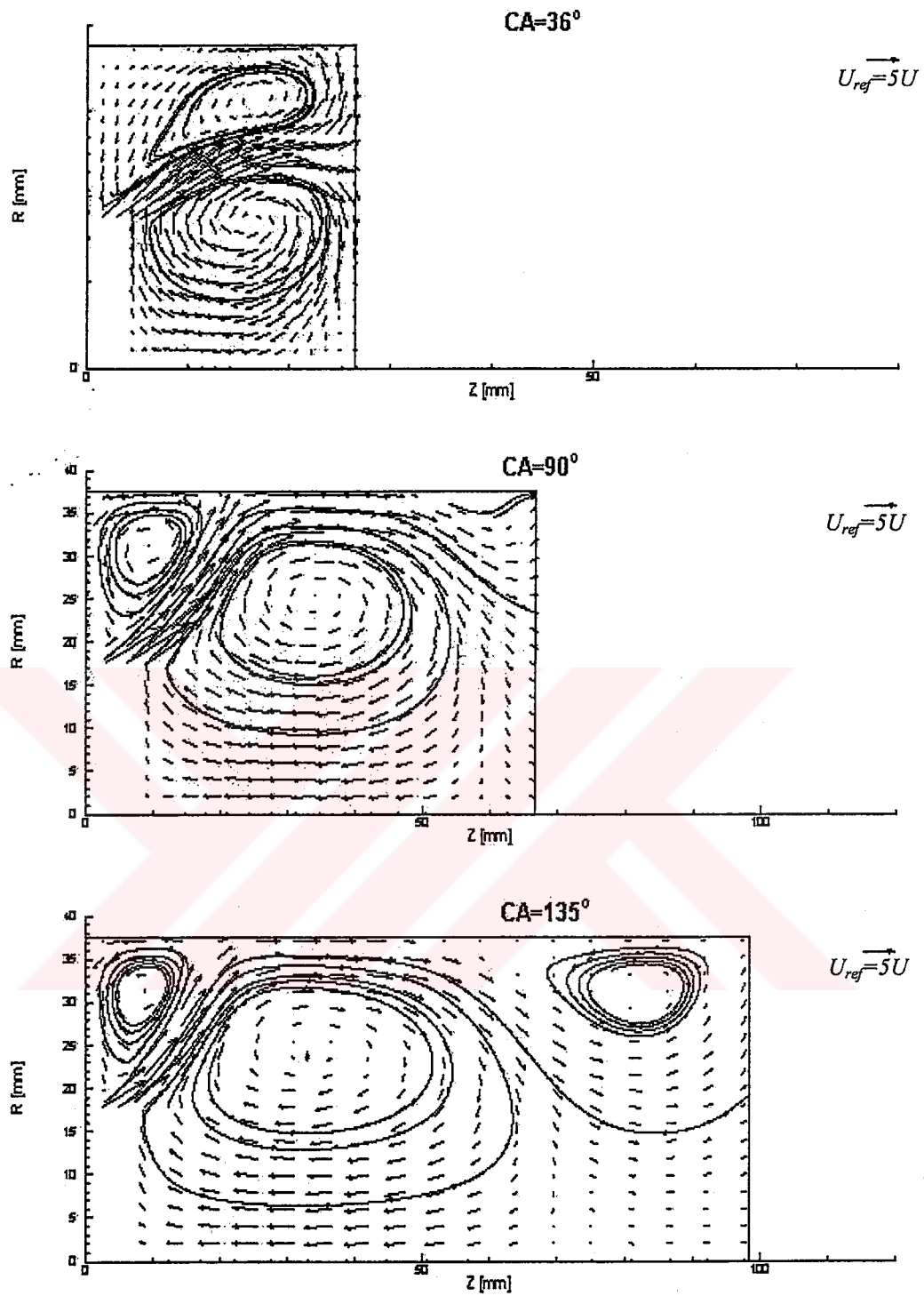


Figure VI.15 Velocity field predictions of the $k-\varepsilon-\tau$ model for test Case II at various crank angles in particle tracking and vector plots

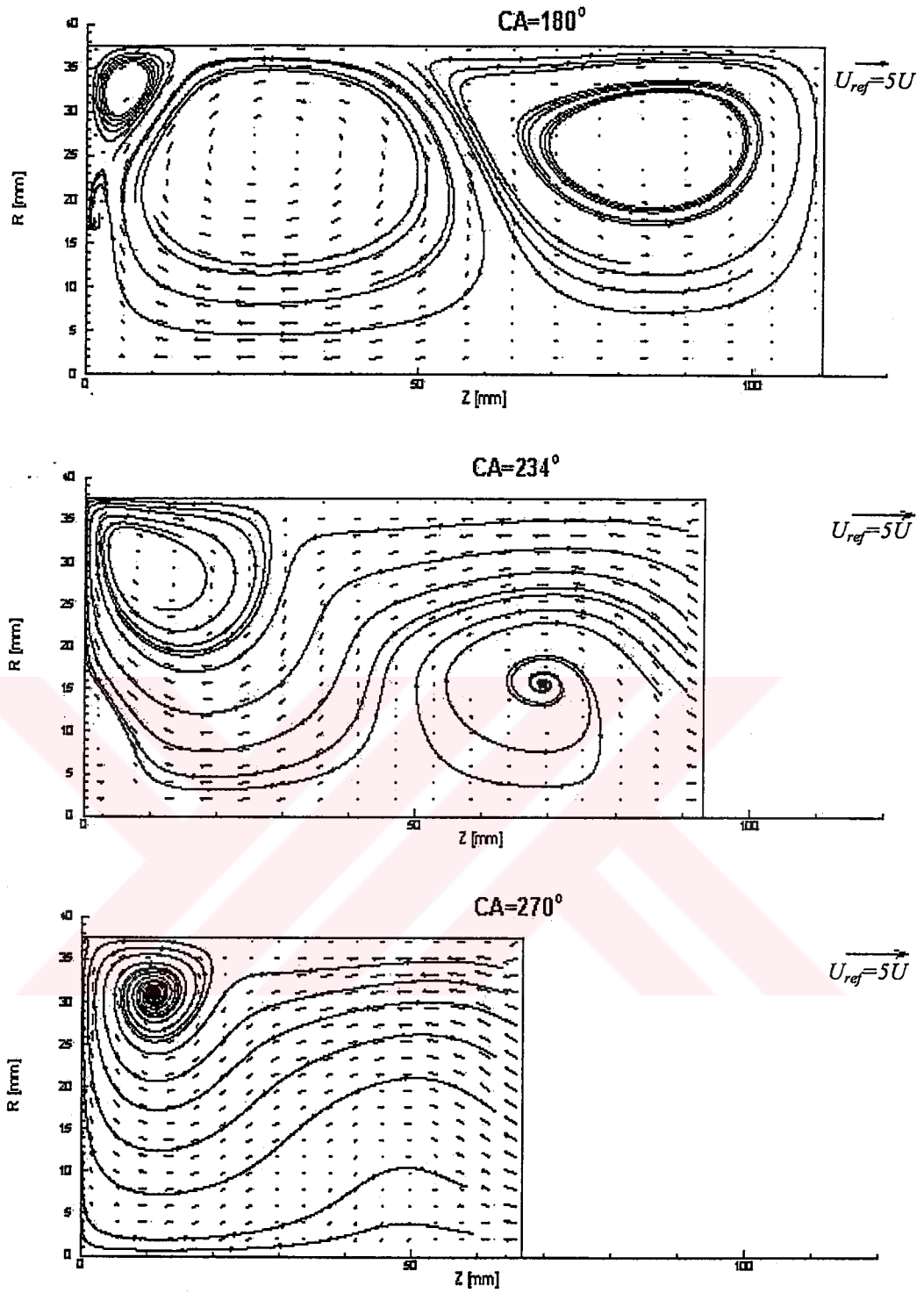


Figure VI.15 Continued

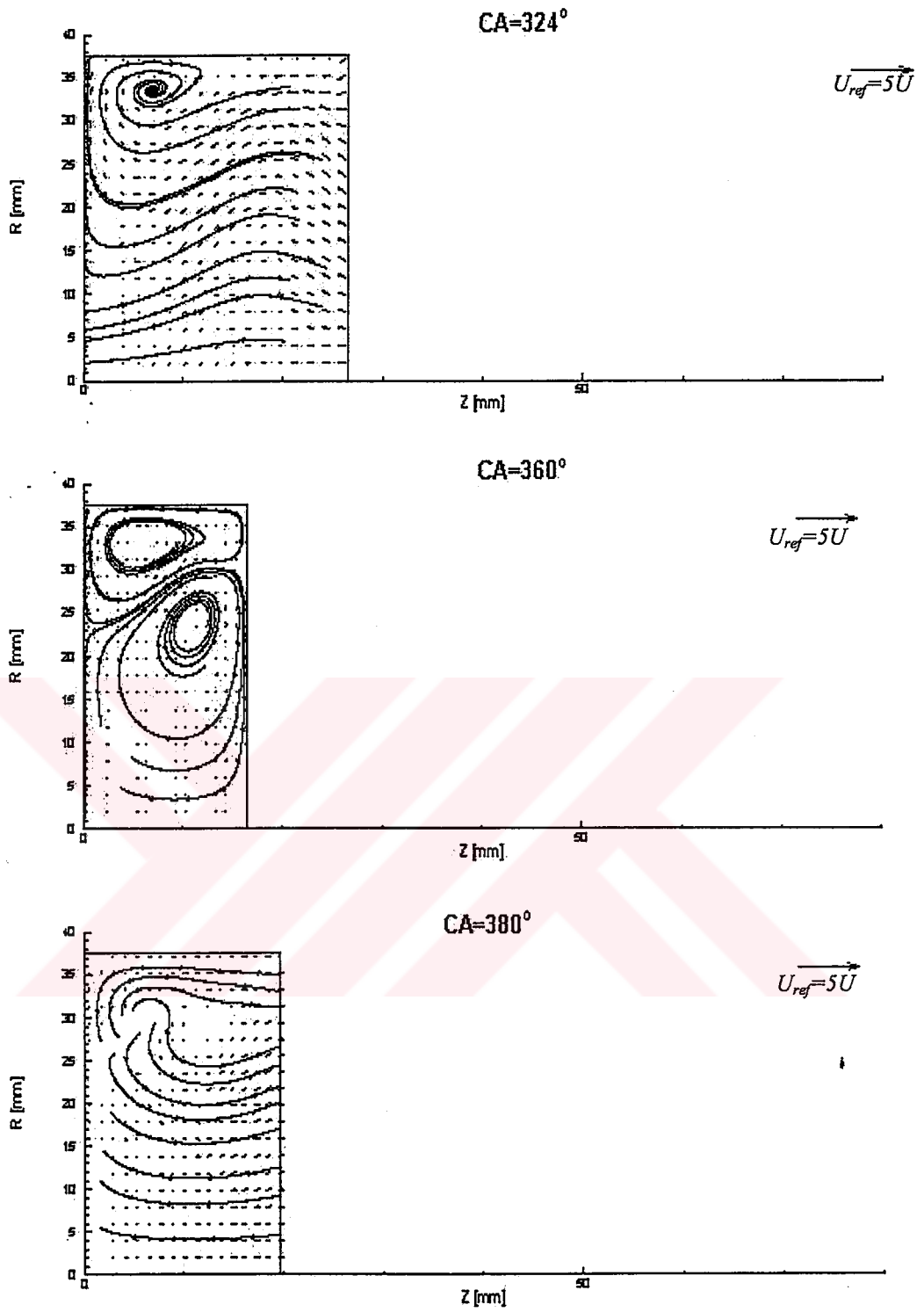


Figure VI.15 Continued

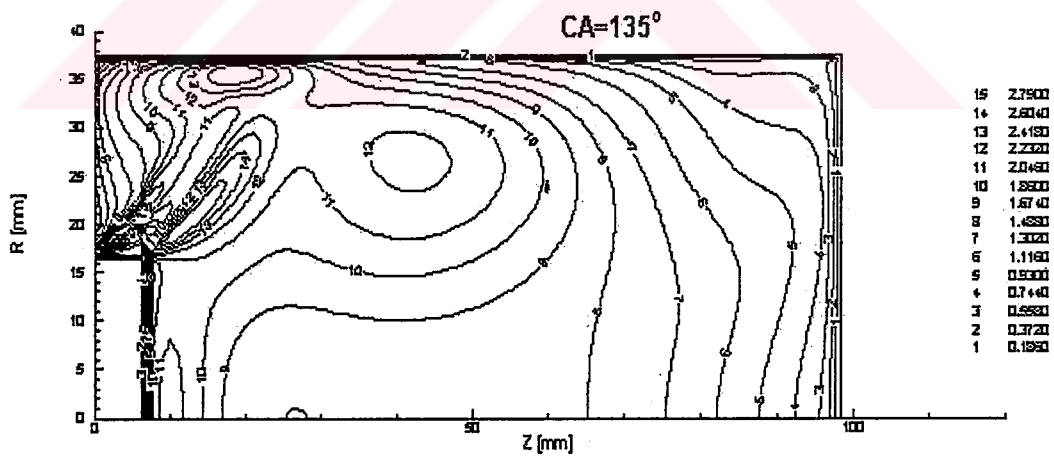
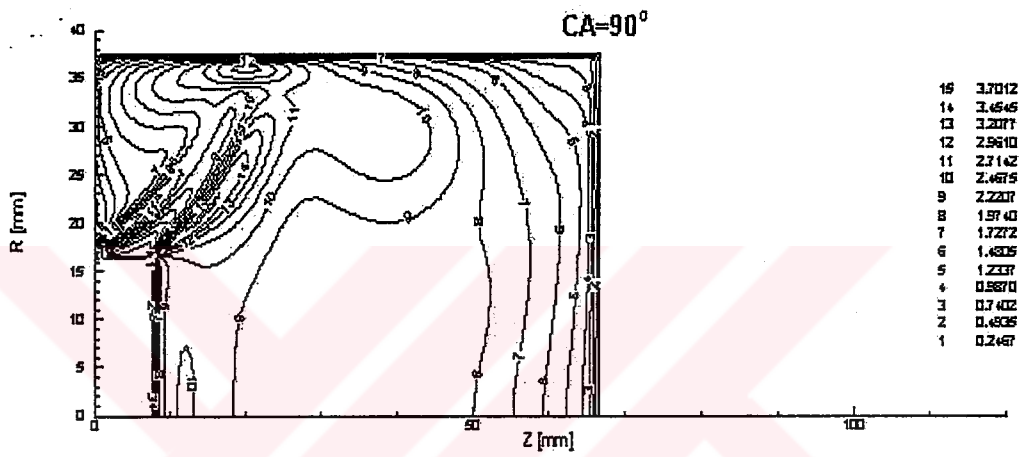
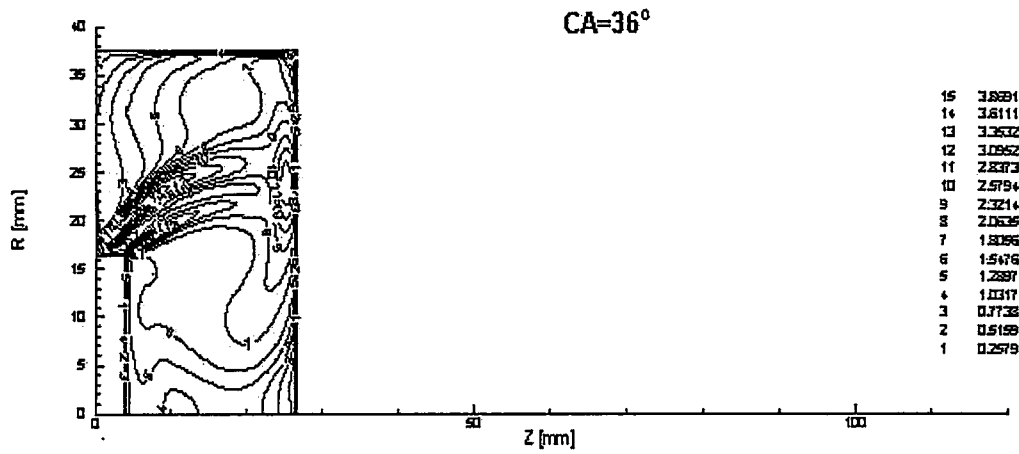


Figure VI.16 Turbulence intensity distributions, predicted by the *MM k-ε model* for test Case II at various crank angles in contour plots

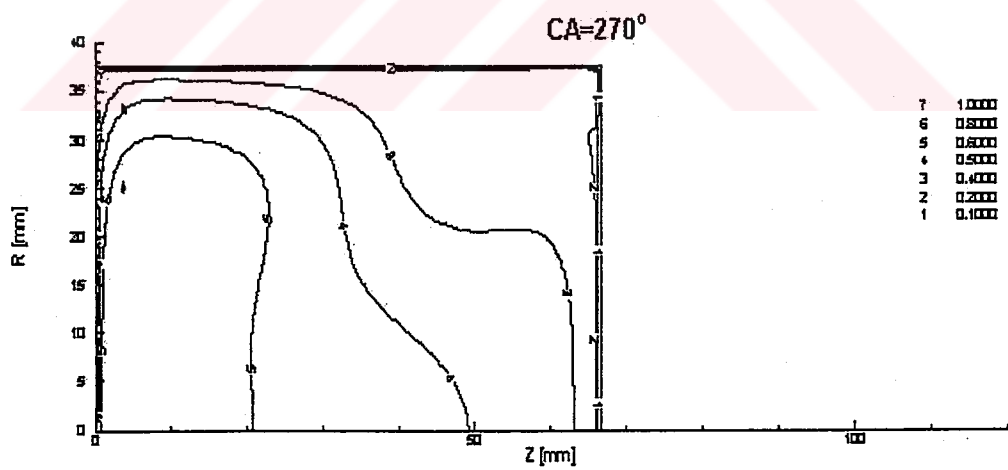
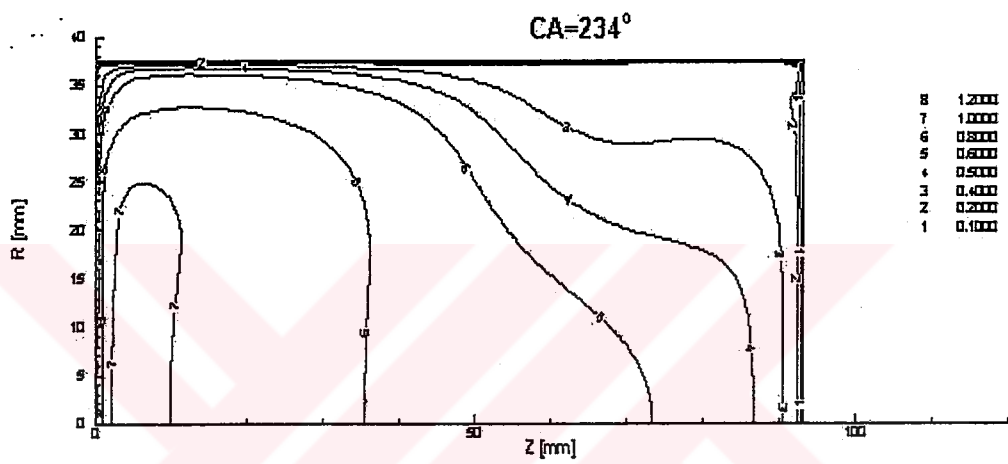
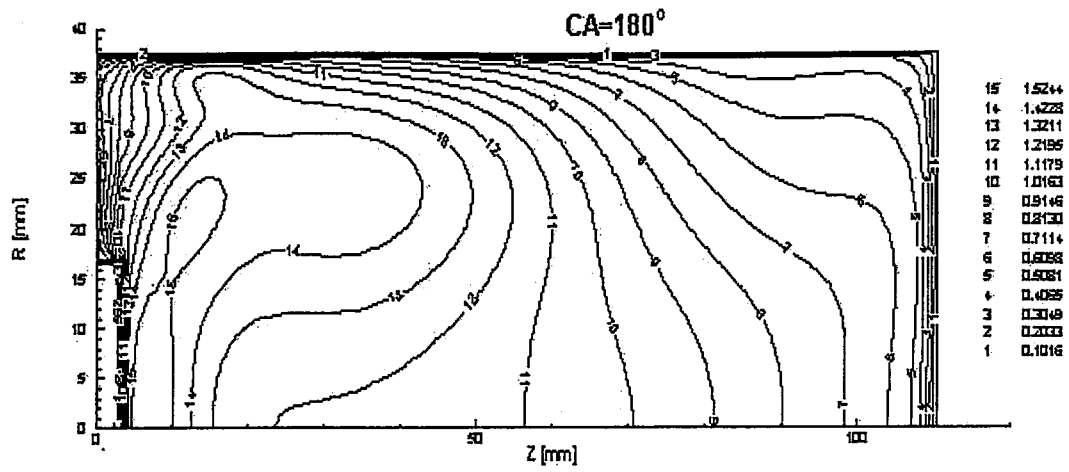


Figure VI.16 Continued

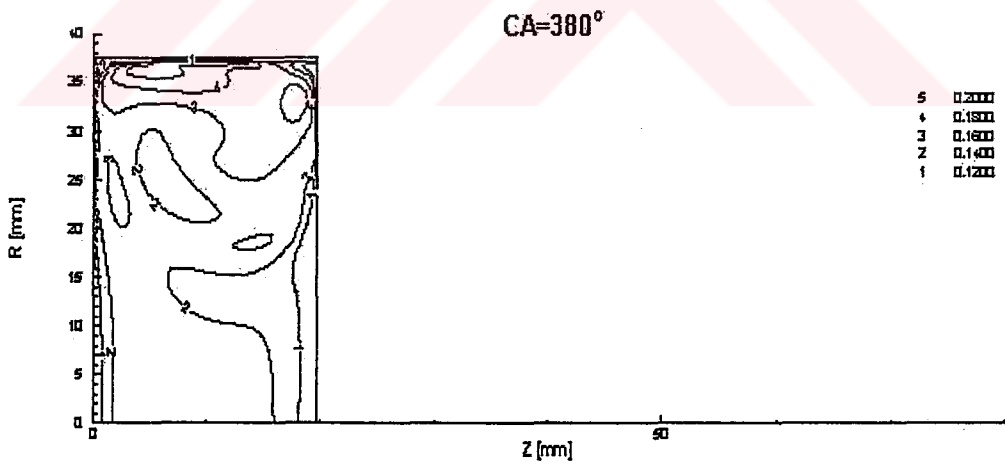
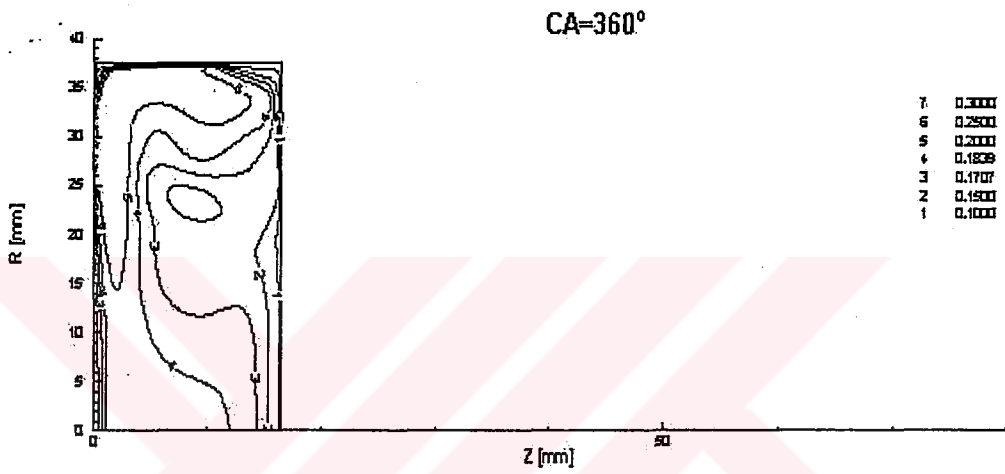
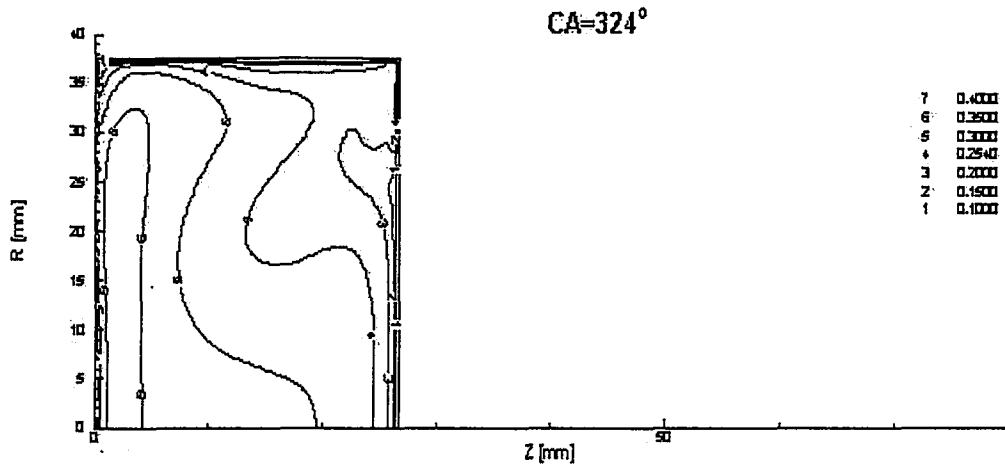


Figure VI.16 Continued

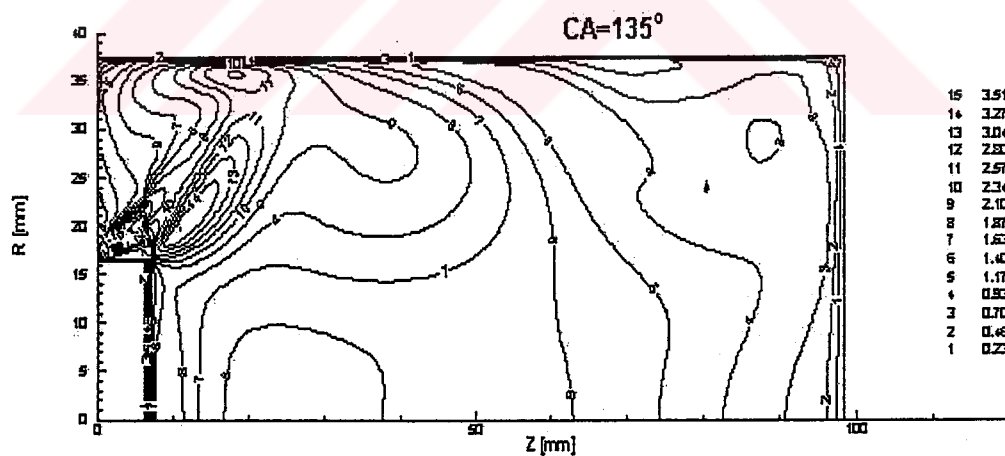
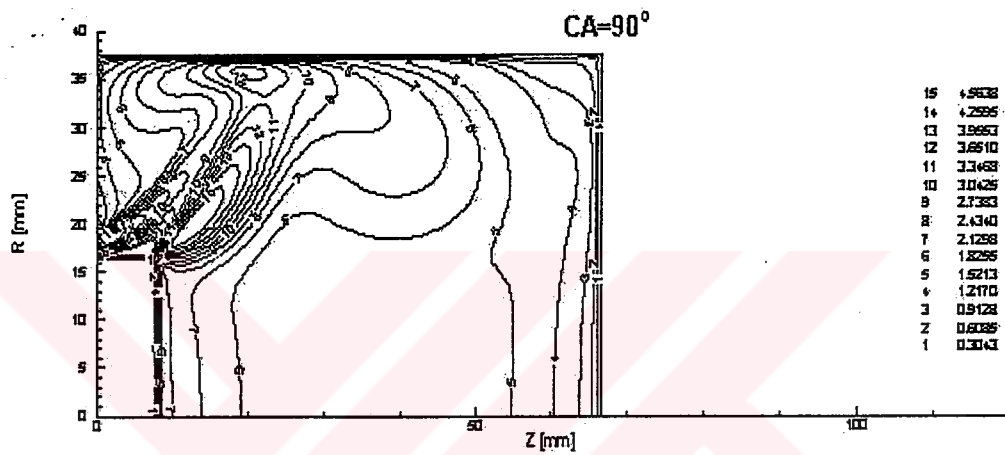
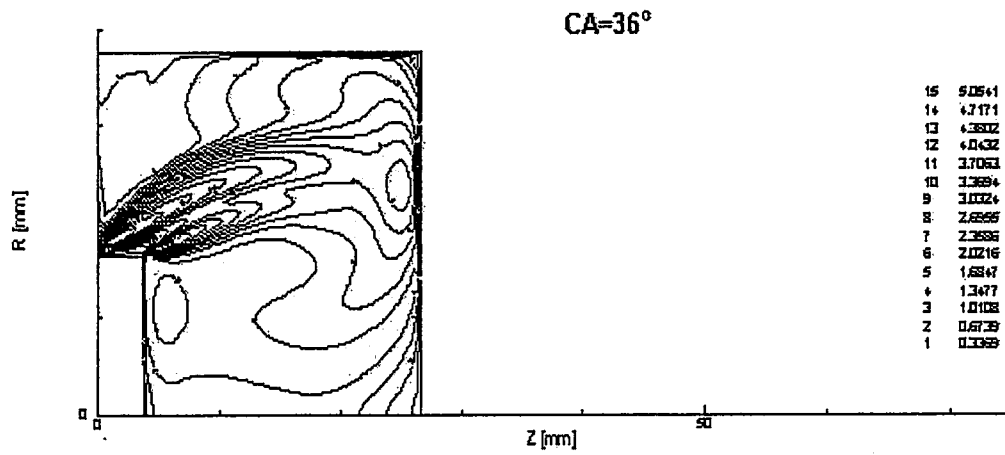


Figure VI.17 Turbulence intensity distributions, predicted by the $k-\epsilon-\tau$ model for test Case II at various crank angles in contour plots

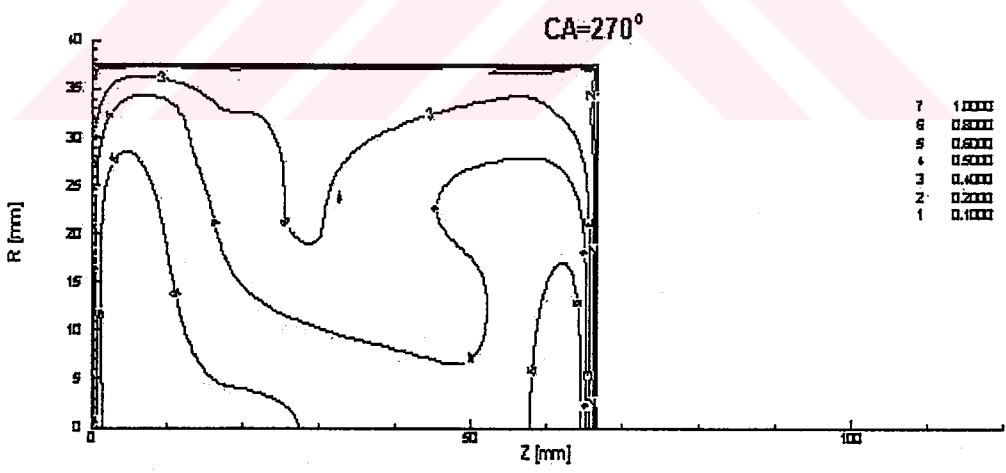
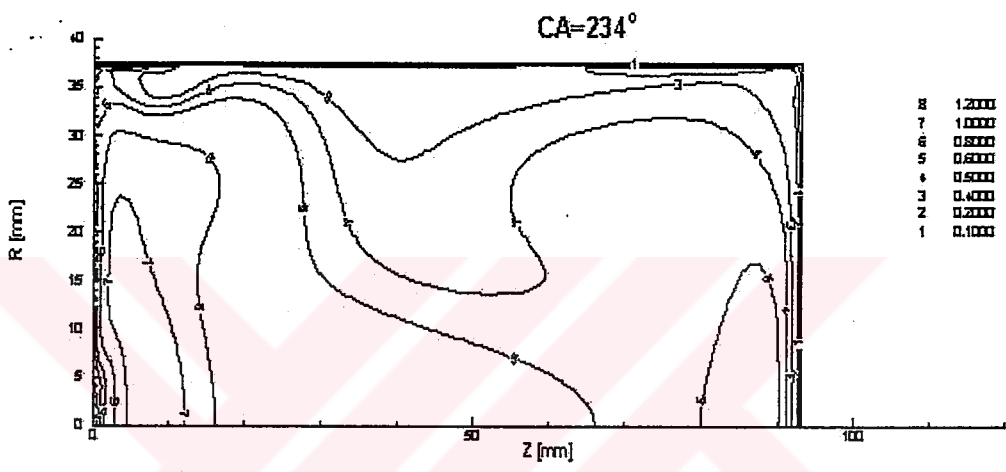
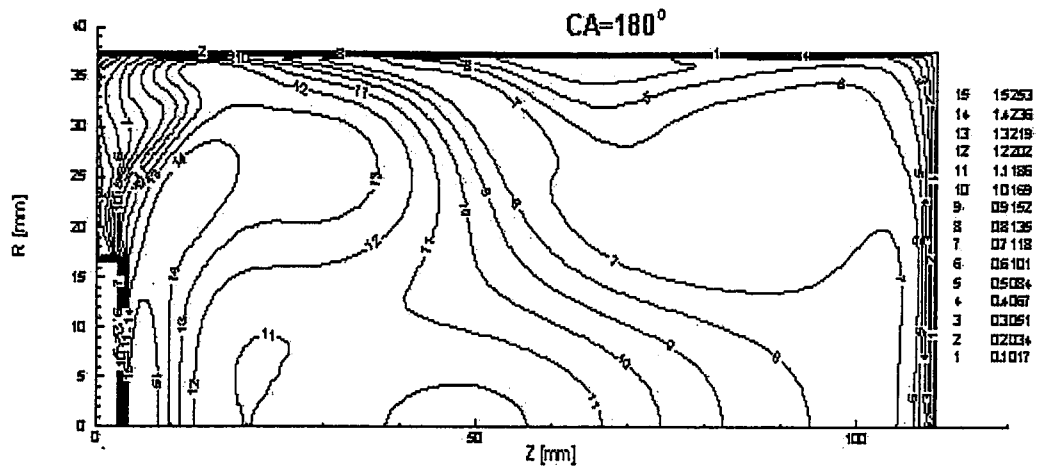


Figure VI.17 Continued

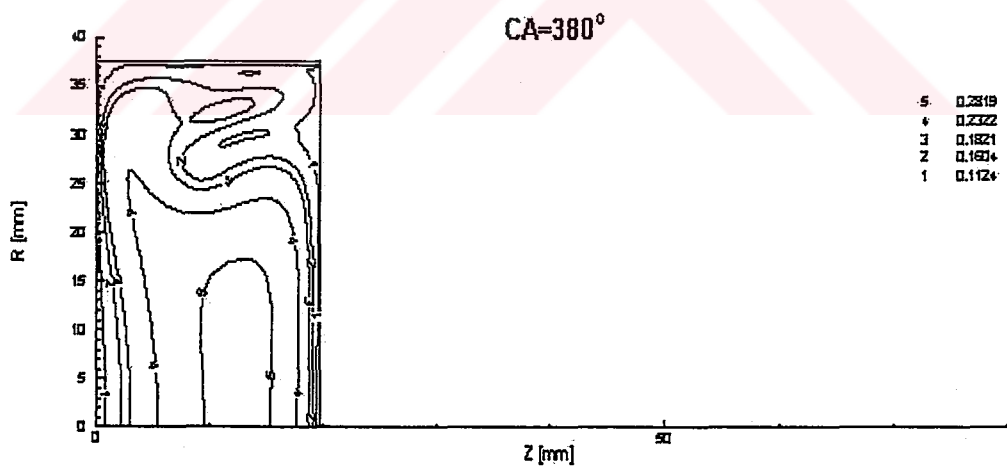
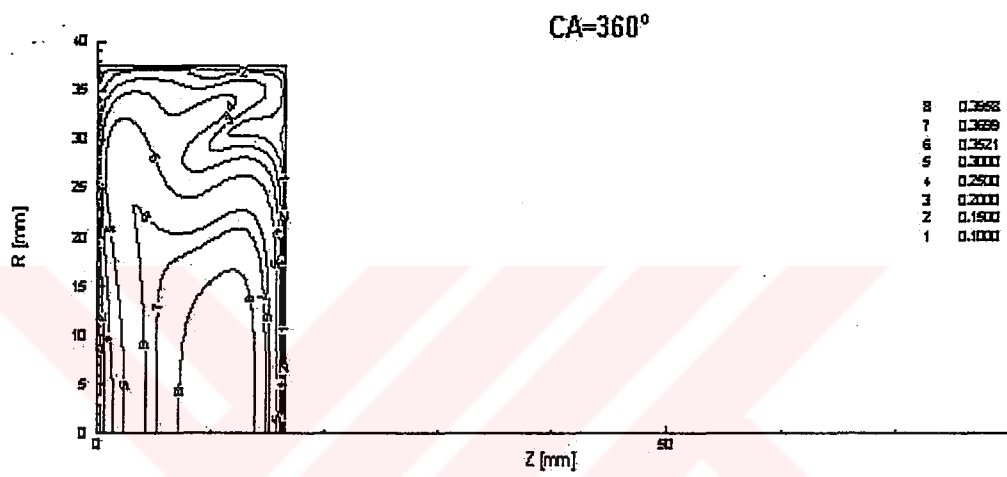
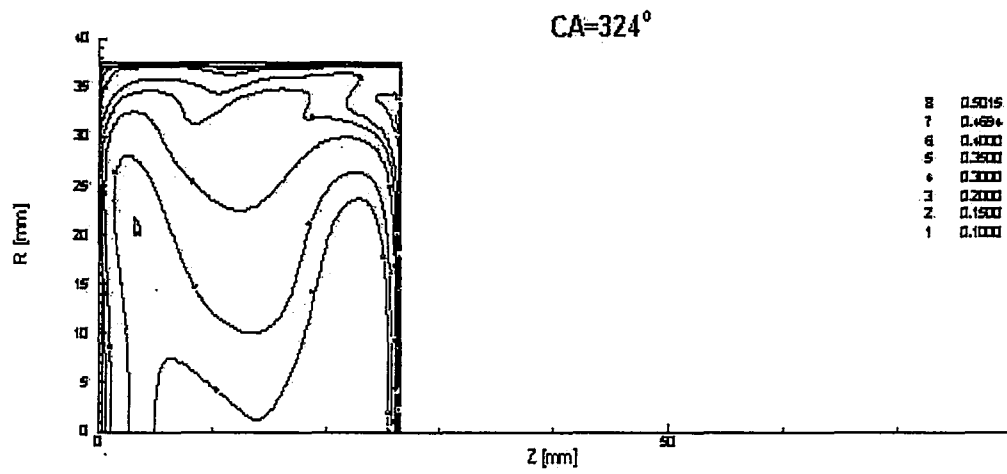


Figure VI.17 Continued

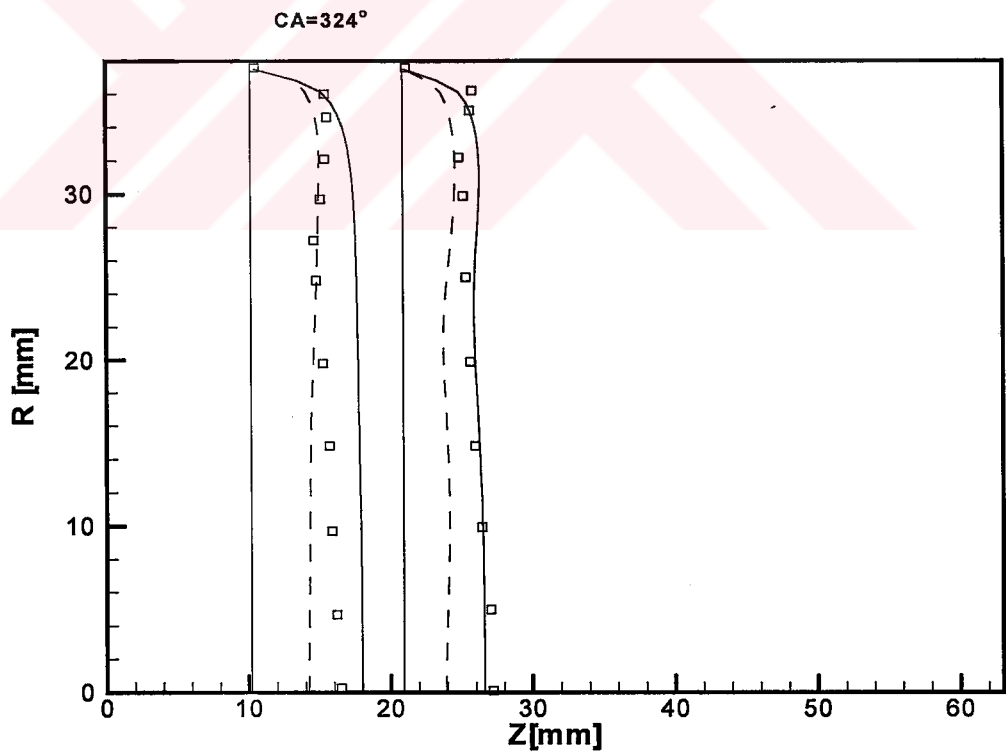
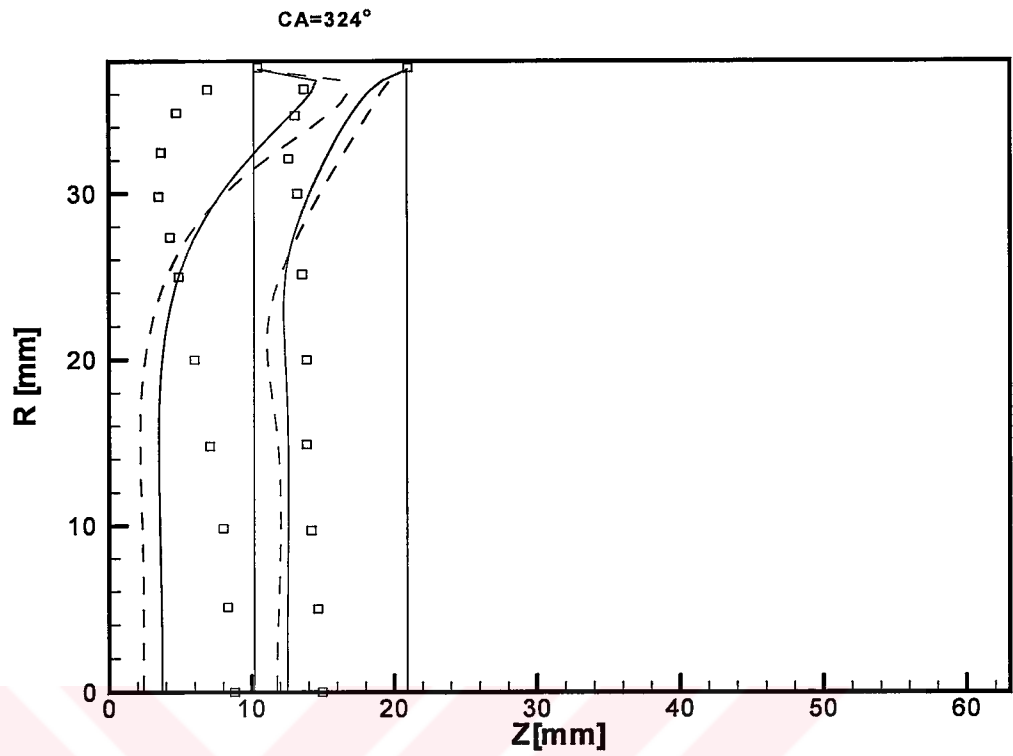


Figure VI.18 The comparison of measured and predicted profiles of axial mean velocity and turbulence intensity for axial location of $z=10$ and 21 mm at $CA=324^\circ$; test Case II. (Full line: $k-\epsilon-\tau$ model dashed line: $k-\epsilon$ model symbols: measurements.)

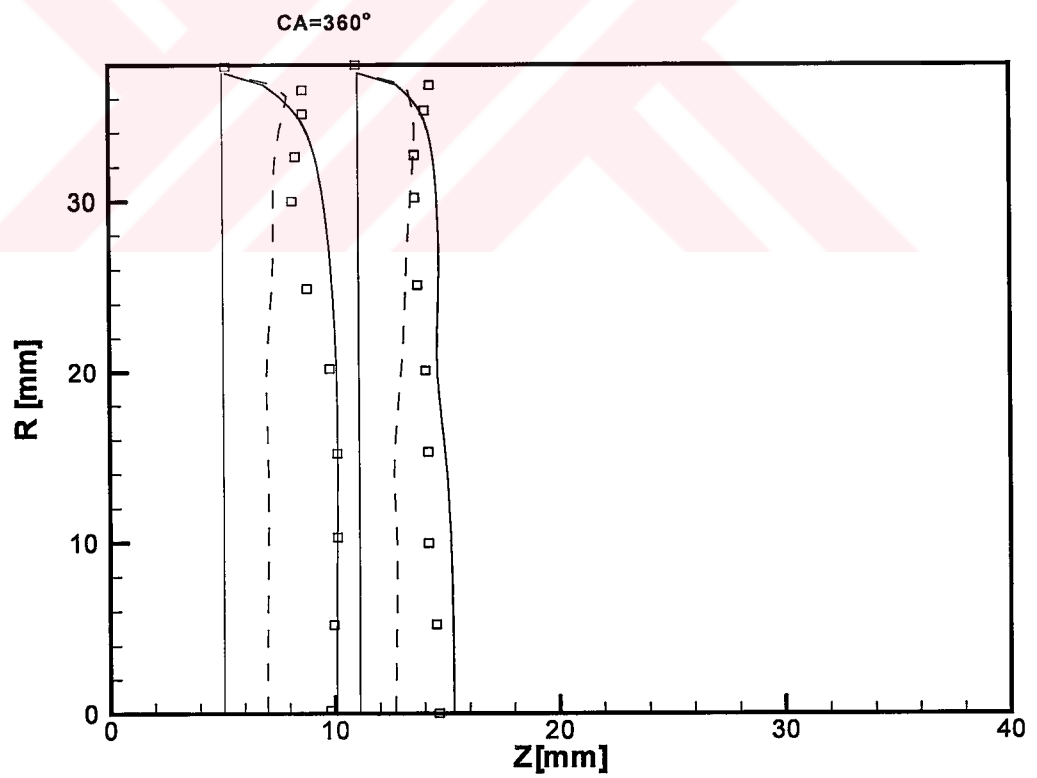
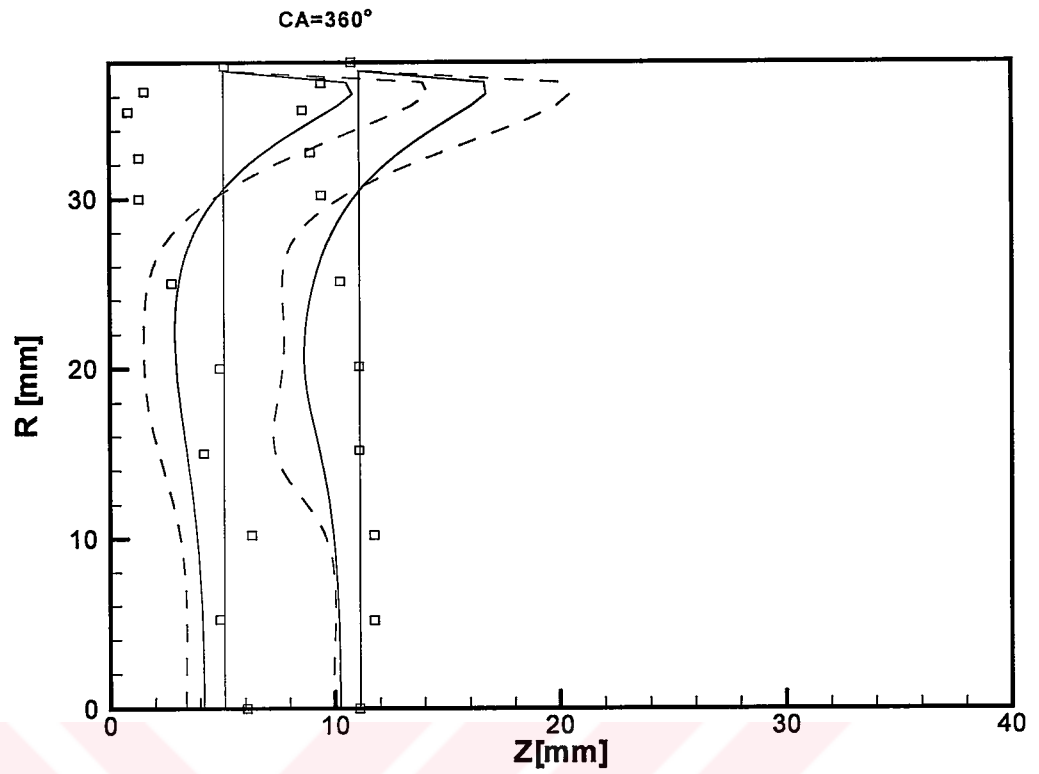


Figure VI.19 The comparison of measured and predicted profiles of axial mean velocity and turbulence intensity for axial location of $z=5$ and 11 mm at $CA=360^\circ$; test Case II. (Full line: $k-\epsilon-\tau$ model dashed line: $k-\epsilon$ model symbols: measurements.)

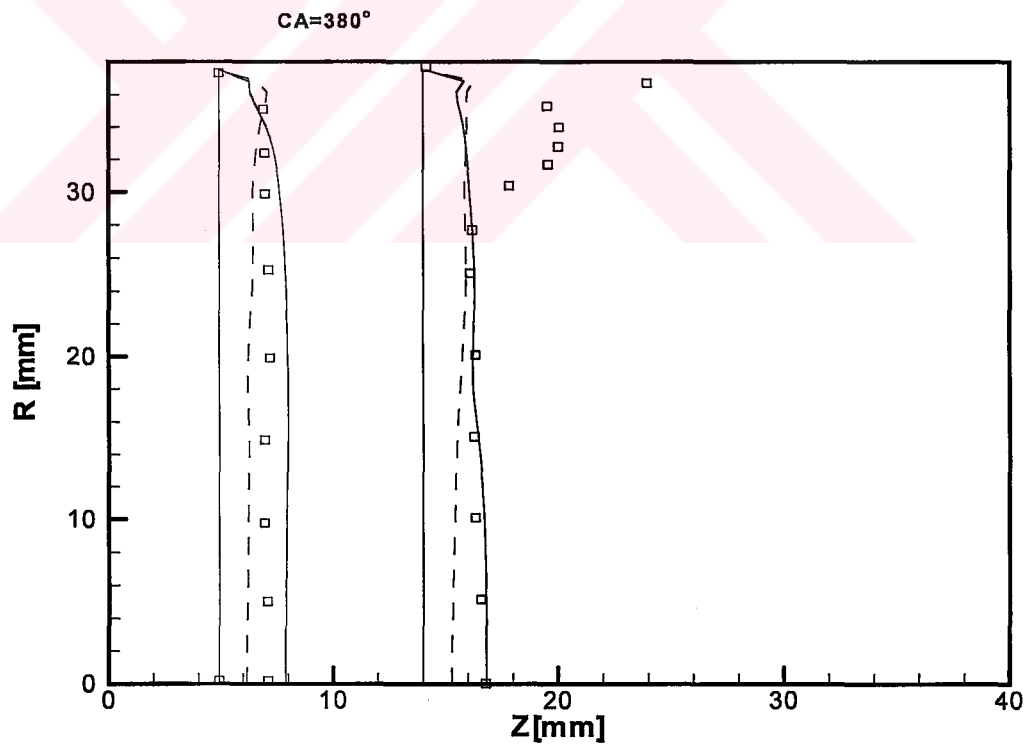
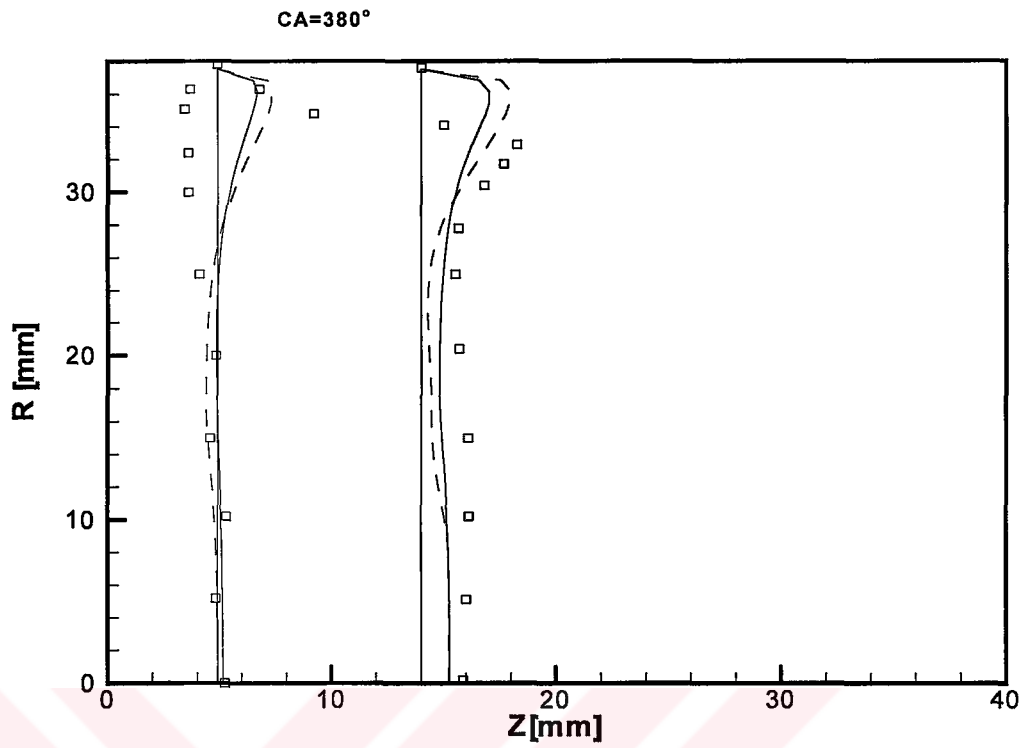


Figure VI.20 The comparison of measured and predicted profiles of axial mean velocity and turbulence intensity for axial location of $z=5$ and 14 mm at $CA=380^\circ$; test Case II. (Full line: $k-\epsilon-\tau$ model dashed line: $k-\epsilon$ model symbols: measurements.)

REFERENCES

- [1] Gul, M.Z.: "Prediction of In-Cylinder Flow by Use of a Multiple-Time-Scale Turbulence Model". *PhD Thesis*, Victory University of Manchester, (1994).
- [2] Wu, C.T.; Ferziger, J.H.; Chapman, D.R.: "Simulation and modeling of homogeneous, compressed turbulence" Fifth Symp. of Turbulent Shear Flows, Cornell Univ, (1985), 17.13-17.20.
- [3] Brun G.; Buffat M.; Jeandel D.: "Flow characteristics in a port-cylinder assembly predicted by a finite-element method with turbulence modeling. ", In *Refined flow Modeling and Turbulence Measurement*, Proceeding of The 3rd Int. Symp., Tokyo (IAHR), (1988).
- [4] Aita S.; Tabbal A.; Munck G.; Fujiwara K.; Hongoh H.; Tamura E.; Obana S.: "Numerical simulation of port-valve-cylinder flow in reciprocating engines", SAE paper 900820, (1990)
- [5] Butler T.D.; Amsden A.A. O'Rourke P.J.; Ramshaw J.D.: " KIVA: A comprehensive model for 2D and 3D engine simulations", SAE paper 850554, (1985)
- [6] Gosman A.D.: " Computational fluid dynamics in the automobile industry", In *Numerical Methods for Fluid Dynamics*, Vol. 2, OUP, (1986)
- [7] Ahmadi-Befrui B.: " Analysis of flow evolution in the cylinders of motored reciprocating engines", *PhD Thesis*, University of London, (1985)
- [8] Watkins A. P.: " Flow an heat transfer in piston-cylinder assemblies" *PhD thesis*, University of London, (1977)
- [9] Morel T.; Mansour N.N.: " Modelling of turbulence in internal combustion engines", *SAE paper* 820040,(1982)
- [10] El-Tahry S:H: "k- ϵ equation for compressible reciprocating engine flows", *AIAA Journal of Energy* , Vol. 7, no 4, (1983)345-353,
- [11] Jahanbakhsh A.: "Prediction of air flow in diesel combustion chambers" *PhD thesis*, University of London, (1985)
- [12] Shah P.; Markatos N.C.: " on the 2D and 3D computer analysis of turbulence in internal combustion engines" *Trans. of ASME*, (87-FE-12), (1987)
- [13] Launder B.E.: "Second moment closure and its use in modeling turbulent industrial flows" In *Int. J. of Num. Methods in Fluids*, 9, (1989) 963-985.
- [14] Reynolds W. C.: "Modeling of fluid motions in engines" In *Combustion modeling in reciprocating engines* Plenum Press, New York, (1980).
- [15] Ahmadi-Befrui B.; Gosman A. D.; Lockwood F.C.; Watkins A,P.: "Multi-dimensional calculation of combustion in an idealized homogeneous charge engine: A progress report" *Trans. of SAE*, (810151), (1981)
- [16] Coleman G.N.; Mansour N.N.: " Simulation and modeling of homogeneous compressible turbulence under isotropic mean compression" In *8th Sym. On turbulence Shear Flows*. (1991)

- [17] Favre A.: "Statistical equations of turbulent gases in problems of hydrodynamics and continuum mechanics", *Soc. Indust. Appl. Math.*, (1969), 231-266
- [18] Woods W. A.; Khan S. R.: "An experimental study of flow through poppet valves" *Proc. ImechE.*, (1965-1966), 180.
- [19] Johns R.J.R.: "Prediction of flow in diesel engine cylinders" *PhD thesis*, University of London, (1980)
- [20] Rodi W.: "Turbulence models and their applications in hydraulics- A state of art review", University of Karlsruhe, Report SFB 80/T/127, (1978).
- [21] Jones W.P.; Launder B.E.: "The prediction of laminarisation with a two equation model of turbulence" In *Int. Heat and Mass Transfer*, 15, (1972), 301-314.
- [22] Versteeg H.K.; Malalasekera W.: "An Introduction to Computational Fluid Dynamics- The Finite Volume Method" Longman Group Ltd, England (1995).
- [23] Jones W.P.; "Models for turbulent flows with variable density and combustion" In *Lecture Series, 1979-2*, Von Karman Inst. For Fluid Dynamics, (1979)
- [24] Launder B.E.; Spalding D.B.: "The Numerical Computation of Turbulent Flows" *Comput. Methods Appl. Mech. Eng.*, vol 3, (1974), 269-289.
- [25] Hoult D.P.; Wong V.W.: "The generation of turbulence in an internal combustion engine" *Symp. On combustion modeling in reciprocating engines*, GM Research Laboratories, Warren-Michigan, (1978)
- [26] B.E. Launder.: "Second moment closure and its use in modelling turbulent industrial flows" *Int. J. Num. Methods in Fluids*, 9, (1989), 963-985.
- [27] Patankar S.V.: "Numerical Heat Transfer and Fluid Flow" McGraw-Hill, New York, (1980).
- [28] Spalding D.B.: "A novel finite difference formulation for differential expressions involving both first and second derivatives" *Int. J. Num. Meth. In Engrg*, 4, (1972)
- [29] Issa, R.I.: "Solution of the implicitly discretised fluid flow equations by operator splitting" *J. Comput. Phys.*, 62, No 1, (1986), 40-65.
- [30] Ahmadi-Befrui B.; Gosman A. D.; Issa R.I.; Watkins A, P.: "An implicit Non-iterative Solution Procedure for the Calculation of Flows in Reciprocating Engine Chambers" *Comput. Methods Appl. Mech. Eng.*, vol 79, (1990), 249-279.
- [31] Thomas L.H.: "Elliptic Problems in Linear Difference Equations over a Network" Watson Sci. Comput. Lab. Report, Columbia University, New York (1949).
- [32] Arcoumanis C.; Bicen A.F.; Whitelaw J.H.: "Squish and Swirl-Squish interaction in motored model engines" *J. Fluids Eng.* (1983)
- [33] Bicen A.F., "Air flow characteristics of model internal-combustion engines" *PhD thesis*, University of London, (1983)
- [34] Ahmadi-Befrui B.: "Assesment of variants of the k-ε model for engine flow application" *Trans of ASME*, (87-FE-11). (1987)
- [35] Gul M. Z.; Yilmaz B.: "Comparison of single and two time-scale turbulence models for in-cylinder engine flows" *Proc. of ESDA2002/ATF-070*. (2002)

APPENDIX A

Length Scales of Turbulence		
Parameter	Definition	Physical Significance
Macro or Integral Length Scale (L)	For the direction (X) parallel to the mean flow (\bar{U}), L_X is defined as: $L_X = \int \bar{R}_X dX = \int \frac{\overline{u_\theta u_X}}{\overline{u_\theta^2}} dX$ where $\overline{u_\theta u_X}$ is the time average of the product of the turbulent velocity fluctuations, u , measured at points θ and X .	Represents a measure of the average size of the largest (energy containing) eddies. They are typically related to the size of the body or scales of the forces generating the motion.
Length Scale of Energy-Containing Eddies (ℓ)	$\ell = C_\mu^{3/4} k^{3/2} / \epsilon$, $C_\mu = 0.09$ where $k \equiv \frac{1}{2} [\overline{u'^2 + v'^2 + w'^2}]$ is the mean turbulence kinetic energy and ϵ its dissipation rate.	A measure of the average size of the energy-containing eddies. Generally: $\ell = 0.1 L_X$
Micro or Taylor Length Scale (λ)	$\lambda^2 = \frac{-\ell}{[\partial^2 \bar{R}_X / \partial X^2]_{X=0}} = \frac{2\overline{u'^2}}{[\partial u / \partial X]^2_{X=0}}$	This is the smallest measurable eddy size into which the larger eddies break up before eventual dissipation in the very fine eddy structure by viscous effects. It may also be interpreted as a measure of the local spatial variation of u .
Dissipation or Kolmogorov Microscale (η)	$\eta = (\nu^3 / \epsilon)^{1/4}$ where ν is the kinematic viscosity.	Represents a measure of the smallest dynamically important scale in the flow, in which the viscous dissipation of k into heat occurs.

Time Scales of Turbulence		
Parameter	Definition	Physical Significance
Macro or Integral Time Scale (L_t)	$L_t = \int \bar{R}_t dt = \int \frac{\overline{u_t u_{t+\tau}}}{\overline{u_t^2}} dt$ where $\overline{u_t u_{t+\tau}}$ is the time average of the product of turbulent velocity fluctuation, u_t , at a fixed point at an instant, t , and a delayed version of itself, $u_{t+\tau}$, where τ is the variable time delay (the so-called correlation time).	Considered as a rough measure of the time that it takes for a coherent structure to pass a point. In the absence of mean flow, it may be regarded as a measure of the lifetime of a turbulent eddy.
Decay or Dissipation Time Scale (τ_d)	$\tau_d = k / \epsilon$	Represents the time over which, in the absence of any turbulence production by the mean flow, a significant change in turbulence energy occurs.
Micro Time Scale (λ_t)	$\lambda_t^2 = \frac{-\tau}{[\partial^2 \bar{R}_t / \partial \tau^2]_{\tau=0}} = \frac{2\overline{u_t'^2}}{[\partial u_t / \partial \tau]^2_{\tau=0}}$	Inversely proportional to the highest measurable frequencies in the turbulent velocity field.
Kolmogorov Micro-Time Scale (η_t)	$\eta_t = (\nu / \epsilon)^{1/2}$	It can be considered as a measure of the mixing rate at the molecular level at which chemical reaction occurs.

General Remarks: (i) Measurement of these parameters in engine flows is based on the assumption that turbulence is stationary over the time interval Δt over which it is studied. This can be approximated in practice if the characteristic time scale of turbulence, λ_t , is smaller than Δt , which in turn must be smaller than the period, τ_p , of any slow variation in the mean flow field, so that $\lambda_t \ll \Delta t \ll \tau_p$ (Dent [1985]).

(ii) In stationary, homogeneous turbulence with constant mean velocity $\bar{U} \gg u'$, the macro- and micro-length and time scales are related by Taylor's Hypothesis: $L_X = \bar{U} L_t$, $\lambda_X = \bar{U} \lambda_t$. As these conditions seldom prevail in engine circumstances, results obtained using these relations must be interpreted with caution.

Table A.1 Definition and physical significance of some important turbulence scales in engine research [1]

APPENDIX B

TECHPLOT MACROS

#!MC 750

```
#!VarSet [MFBD] = 'C:\programs\TEC75'  
$!READDATASET  
"!TECHOME\WORK\TEZ\CASE2 KEPSTO\TEC_98_05.DAT"  
$!FRAMELAYOUT  
SHOWBORDER = FALSE  
SHOWHEADER = FALSE  
XYPOS  
{  
X = 0.5  
Y = 0.5  
}  
WIDTH = 3.5  
HEIGHT = 2.5  
$!ACTIVEFIELDZONES = [1]  
$!FIELDLAYERS SHOWCONTOUR = YES  
$!FIELDLAYERS SHOWMESH = NO  
$!FIELD [1]  
CONTOUR  
{  
CONTOURTYPE = LINES  
COLOR = BLACK  
}  
BOUNDARY {COLOR = BLACK}  
$!COLORSPECTRUM CONTOURCOLORMAP = GRAYSCALE  
$!GLOBALCONTOUR  
VAR = 5  
LABELS  
{  
SHOW = TRUE  
COLOR = BLACK  
LABELWITHVALUE = FALSE  
}  
LEGEND  
{  
SHOW = TRUE  
NUMFORMAT
```

```

{
FORMATTING = FIXEDFLOAT
PRECISION = 4
}
BOX
{
BOXTYPE = NONE
}
}
$!TWO D AXIS
AXISMODE = INDEPENDENT
XDETAIL
{
RANGEMIN = 0.0
RANGEMAX = 0.120
}
YDETAIL
{
RANGEMIN = 0.0
RANGEMAX = 0.040
}
$!REDRAW
$!CREATENEWFRAME
$!READDATASET "|TECHOME|/WORK/TEZ\CASE2_KEPS/TEC_98_025.DAT"
$!FRAME LAYOUT
SHOWBORDER = FALSE
SHOWHEADER = FALSE
XYPOS
{
X = 4.0
Y = 0.5
}
WIDTH = 3.5
HEIGHT = 2.5
$!ACTIVEFIELDZONES = [1]
$!FIELDLAYERS SHOWCONTOUR = YES
$!FIELDLAYERS SHOWMESH = NO
$!FIELD [1]
CONTOUR
{
CONTOURTYPE = LINES
COLOR =BLACK
}
BOUNDARY {COLOR = BLACK}
$!COLORSPECTRUM CONTOURCOLORMAP = GRAYSCALE
$!GLOBALCONTOUR
VAR = 5
LABELS
{
SHOW = TRUE
}

```

```

COLOR = BLACK
LABELWITHVALUE = FALSE
}
LEGEND
{
SHOW = TRUE
NUMFORMAT
{
FORMATTING = FIXEDFLOAT
PRECISION = 4
}
}
BOX
{
BOXTYPE = NONE
}
}
$!TWO D AXIS
AXISMODE = INDEPENDENT
XDETAIL
{
RANGEMIN = 0.0
RANGEMAX = 0.120
}
YDETAIL
{
RANGEMIN = 0.0
RANGEMAX = 0.040
}
}
$!REDRAW
$!CREATENEWFRAME
$!READDATASET
"TECHOME/WORK/TEZ\CASE2_KEPSTO/TEC_98_05.DAT"
$!FRAME LAYOUT
SHOWBORDER = FALSE
SHOWHEADER = FALSE
XYPOS
{
X = 0.5
Y = 3.0
}
WIDTH = 3.5
HEIGHT = 2.5
$!ACTIVEFIELDZONES = [2]
$!FIELDLAYERS SHOWCONTOUR = YES
$!FIELDLAYERS SHOWMESH = NO
$!FIELD [2]
CONTOUR
{
CONTOURTYPE = LINES
COLOR =BLACK

```

```

}
BOUNDARY {COLOR = BLACK}
$!COLORSPECTRUM CONTOURCOLORMAP = GRAYSCALE
$!GLOBALCONTOUR
VAR = 5
LABELS
{
SHOW = TRUE
COLOR = BLACK
LABELWITHVALUE = FALSE
}
LEGEND
{
SHOW = TRUE
NUMFORMAT
{
FORMATTING = FIXEDFLOAT
PRECISION = 4
}
}
BOX
{
BOXTYPE = NONE
}
}
$!TWO D AXIS
AXISMODE = INDEPENDENT
XDETAIL
{
RANGEMIN = 0.0
RANGEMAX = 0.120
}
YDETAIL
{
RANGEMIN = 0.0
RANGEMAX = 0.040
}
$!REDRAW
$!CREATENEWFRAME
$!READDATASET "|TECHOME|/WORK/TEZ\CASE2_KEPS/TEC_98_025.DAT"
$!FRAME LAYOUT
SHOWBORDER = FALSE
SHOWHEADER = FALSE
XYPOS
{
X = 4.0
Y = 3.0
}
WIDTH = 3.5
HEIGHT = 2.5
$!ACTIVEFIELDZONES = [2]

```

```

$!FIELDLAYERS SHOWCONTOUR = YES
$!FIELDLAYERS SHOWMESH = NO
$!FIELD [2]
CONTOUR
{
CONTOURTYPE = LINES
COLOR =BLACK
}
BOUNDARY {COLOR = BLACK}
$!COLORSPECTRUM CONTOURCOLORMAP = GRAYSCALE
$!GLOBALCONTOUR
VAR = 5
LABELS
{
SHOW = TRUE
COLOR = BLACK
LABELWITHVALUE = FALSE
}
LEGEND
{
SHOW = TRUE
NUMFORMAT
{
FORMATTING = FIXEDFLOAT
PRECISION = 4
}
}
BOX
{
BOXTYPE = NONE
}
}
$!TWO DAXIS
AXISMODE = INDEPENDENT
XDETAIL
{
RANGEMIN = 0.0
RANGEMAX = 0.120
}
YDETAIL
{
RANGEMIN = 0.0
RANGEMAX = 0.040
}
$!REDRAW
$!CREATENEWFRAME
$!READDATASET
"|\TECHOME|\WORK\TEZ\CASE2_KEPSTO\TEC_98_05.DAT"
$!FRAME LAYOUT
SHOWBORDER = FALSE
SHOWHEADER = FALSE

```

```

XYPOS
{
X = 0.5
Y = 5.5
}
WIDTH = 3.5
HEIGHT = 2.5
$!ACTIVEFIELDZONES = [3]
$!FIELDLAYERS SHOWCONTOUR = YES
$!FIELDLAYERS SHOWMESH = NO
$!FIELD [3]
CONTOUR
{
CONTOURTYPE = LINES
COLOR = BLACK
}
BOUNDARY {COLOR = BLACK}
$!COLORSPECTRUM CONTOURCOLORMAP = GRAYSCALE
$!GLOBALCONTOUR
VAR = 5
LABELS
{
SHOW = TRUE
COLOR = BLACK
LABELWITHVALUE = FALSE
}
LEGEND
{
SHOW = TRUE
NUMFORMAT
{
FORMATTING = FIXEDFLOAT
PRECISION = 4
}
}
BOX
{
BOXTYPE = NONE
}
}
$!TWO D AXIS
AXISMODE = INDEPENDENT
XDETAIL
{
RANGEMIN = 0.0
RANGEMAX = 0.120
}
YDETAIL
{
RANGEMIN = 0.0
RANGEMAX = 0.040
}

```

```

}
$!REDRAW
$!CREATENEWFRAME
$!READDATASET "|TECHOME|/WORK/TEZ\CASE2_KEPS/TEC_98_025.DAT"
$!FRAMELAYOUT
SHOWBORDER = FALSE
SHOWHEADER = FALSE
XYPOS
{
X = 4.0
Y = 5.5
}
WIDTH = 3.5
HEIGHT = 2.5
$!ACTIVEFIELDZONES = [3]
$!FIELDLAYERS SHOWCONTOUR = YES
$!FIELDLAYERS SHOWMESH = NO
$!FIELD [3]
CONTOUR
{
CONTOURTYPE = LINES
COLOR =BLACK
}
BOUNDARY {COLOR = BLACK}
$!COLORSPECTRUM CONTOURCOLORMAP = GRAYSCALE
$!GLOBALCONTOUR
VAR = 5
LABELS
{
SHOW = TRUE
COLOR = BLACK
LABELWITHVALUE = FALSE
}
LEGEND
{
SHOW = TRUE
NUMFORMAT
{
FORMATTING = FIXEDFLOAT
PRECISION = 4
}
}
BOX
{
BOXTYPE = NONE
}
}
$!TWO DAXIS
AXISMODE = INDEPENDENT
XDETAIL
{

```

```

RANGEMIN = 0.0
RANGEMAX = 0.120
}
YDETAIL
{
RANGEMIN = 0.0
RANGEMAX = 0.040
}
$!REDRAW
$!CREATENEWFRAME
$!READDATASET
"|TECHHOME|/WORK/TEZ/CASE2_KEPSTO/TEC_98_05.DAT"
$!FRAMELAYOUT
SHOWBORDER = FALSE
SHOWHEADER = FALSE
XYPOS
{
X = 0.5
Y = 8.0
}
WIDTH = 3.5
HEIGHT = 2.5
$!ACTIVEFIELDZONES = [4]
$!FIELDLAYERS SHOWCONTOUR = YES
$!FIELDLAYERS SHOWMESH = NO
$!FIELD [4]
CONTOUR
{
CONTOURTYPE = LINES
COLOR = BLACK
}
BOUNDARY {COLOR = BLACK}
$!COLORSPECTRUM CONTOURCOLORMAP = GRAYSCALE
$!GLOBALCONTOUR†
VAR = 5
LABELS
{
SHOW = TRUE
COLOR = BLACK
LABELWITHVALUE = FALSE
}
LEGEND
{
SHOW = TRUE
NUMFORMAT
{
FORMATTING = FIXEDFLOAT
PRECISION = 4
}
}
BOX

```

```

{
BOXTYPE = NONE
}
}
$!TWODAXIS
AXISMODE = INDEPENDENT
XDETAIL
{
RANGEMIN = 0.0
RANGEMAX = 0.120
}
YDETAIL
{
RANGEMIN = 0.0
RANGEMAX = 0.040
}
$!REDRAW
$!CREATENEWFRAME
$!READDATASET "|TECHOME|/WORK/TEZ\CASE2_KEPS/TEC_98_025.DAT"
$!FRAMELAYOUT
SHOWBORDER = FALSE
SHOWHEADER = FALSE
XYPOS
{
X = 4.0
Y = 8.0
}
WIDTH = 3.5
HEIGHT = 2.5
$!ACTIVEFIELDZONES = [4]
$!FIELDLAYERS SHOWCONTOUR = YES
$!FIELDLAYERS SHOWMESH = NO
$!FIELD [4]
CONTOUR
{
CONTOURTYPE = LINES
COLOR =BLACK
}
BOUNDARY {COLOR = BLACK}
$!COLORSPECTRUM CONTOURCOLORMAP = GRAYSCALE
$!GLOBALCONTOUR
VAR = 5
LABELS
{
SHOW = TRUE
COLOR = BLACK
LABELWITHVALUE = FALSE
}
LEGEND
{

```

```

SHOW = TRUE
NUMFORMAT
{
  FORMATTING = FIXEDFLOAT
  PRECISION = 4
}
BOX
{
  BOXTYPE = NONE
}
}
$!TWODAXIS
AXISMODE = INDEPENDENT
XDETAIL
{
  RANGEMIN = 0.0
  RANGEMAX = 0.120
}
YDETAIL
{
  RANGEMIN = 0.0
  RANGEMAX = 0.040
}
$!REDRAW

$!RemoveVar |MFBD|

#!MC 750
$!VarSet |MFBD| = 'C:\programs\TEC75'
$!READDATASET "|TECHOME|\WORK\TEZ\CASE2_KEPSTO\tec_98_05.DAT"
$!FRAMELAYOUT
SHOWBORDER = FALSE
SHOWHEADER = FALSE
XYPOS
{
  X = 0.5
  Y = 0.5
}
WIDTH = 3.5
HEIGHT = 2.5
$!ACTIVEFIELDZONES = [5]
$!FIELDLAYERS SHOWCONTOUR = YES
$!FIELDLAYERS SHOWMESH = NO
$!FIELD [5]
CONTOUR
{
  CONTOURTYPE = LINES
  COLOR =BLACK
}
BOUNDARY {COLOR = BLACK}

```

```

$!COLORSPECTRUM CONTOURCOLORMAP = GRAYSCALE
$!GLOBALCONTOUR
VAR = 5
LABELS
{
SHOW = TRUE
COLOR = BLACK
LABELWITHVALUE = FALSE
}
LEGEND
{
SHOW = TRUE
NUMFORMAT
{
FORMATTING = FIXEDFLOAT
PRECISION = 4
}
}
BOX
{
BOXTYPE = NONE
}
}
$!CONTOURLEVELS NEW
RAWDATA
8
0.1000
0.2000
0.4000
0.5000
0.6000
0.8000
1.0000
1.2000
$!TWO DAXIS
AXISMODE = INDEPENDENT
XDETAIL
{
RANGEMIN = 0.0
RANGEMAX = 0.120
}
YDETAIL
{
RANGEMIN = 0.0
RANGEMAX = 0.040
}
$!REDRAW
$!CREATENEWFRAME
$!READDATASET "|TECHHOME|/WORK/TEZ\CASE2_KEPS/tec_98_025.DAT"
$!FRAME LAYOUT
SHOWBORDER = FALSE

```

```
SHOWHEADER = FALSE
XYPOS
{
X = 4
Y = 0.5
}
WIDTH = 3.5
HEIGHT = 2.5
$!ACTIVEFIELDZONES = [5]
$!FIELDLAYERS SHOWCONTOUR = YES
$!FIELDLAYERS SHOWMESH = NO
$!FIELD [5]
CONTOUR
{
CONTOURTYPE = LINES
COLOR = BLACK
}
BOUNDARY {COLOR = BLACK}
$!COLORSPECTRUM CONTOURCOLORMAP = GRAYSCALE
$!GLOBALCONTOUR
VAR = 5
LABELS
{
SHOW = TRUE
COLOR = BLACK
LABELWITHVALUE = FALSE
}
LEGEND
{
SHOW = TRUE
NUMFORMAT
{
FORMATTING = FIXEDFLOAT
PRECISION = 4
}
}
BOX
{
BOXTYPE = NONE
}
}
$!CONTOURLEVELS NEW
RAWDATA
8
0.1000
0.2000
0.4000
0.5000
0.6000
0.8000
1.0000
```

```

1.2000
$!TWODAXIS
AXISMODE = INDEPENDENT
XDETAIL
{
RANGEMIN = 0.0
RANGEMAX = 0.120
}
YDETAIL
{
RANGEMIN = 0.0
RANGEMAX = 0.040
}
$!REDRAW
$!CREATENEWFRAME
$!READDATASET
"|TECHOME/WORK/TEZ/CASE2_KEPSTO/TEC_98_05.DAT"
$!FRAMELAYOUT
SHOWBORDER = FALSE
SHOWHEADER = FALSE
XYPOS
{
X = 0.5
Y = 3
}
WIDTH = 3.5
HEIGHT = 2.5
$!ACTIVEFIELDZONES = [6]
$!FIELDLAYERS SHOWCONTOUR = YES
$!FIELDLAYERS SHOWMESH = NO
$!FIELD [6]
CONTOUR
{
CONTOURTYPE = LINES
COLOR =BLACK
}
BOUNDARY {COLOR = BLACK}
$!COLORSPECTRUM CONTOURCOLORMAP = GRAYSCALE
$!GLOBALCONTOUR
VAR = 5
LABELS
{
SHOW = TRUE
COLOR = BLACK
LABELWITHVALUE = FALSE
}
LEGEND
{
SHOW = TRUE
NUMFORMAT

```

```

{
FORMATTING = FIXEDFLOAT
PRECISION = 4
}
BOX
{
BOXTYPE = NONE
}
}
$!CONTOURLEVELS NEW
RAWDATA
7
0.1000 .
0.2000
0.4000
0.5000
0.6000
0.8000
1.0000
$!TWO D AXIS
AXISMODE = INDEPENDENT
XDETAIL
{
RANGEMIN = 0.0
RANGEMAX = 0.120
}
YDETAIL
{
RANGEMIN = 0.0
RANGEMAX = 0.040
}
$!REDRAW
$!CREATENEWFRAME
$!READDATASET "|TECHHOME|/WORK/TEZ\CASE2_KEPS/TEC_98_025.DAT"
$!FRAME LAYOUT
SHOWBORDER = FALSE
SHOWHEADER = FALSE
XYPOS
{
X = 4
Y = 3
}
WIDTH = 3.5
HEIGHT = 2.5
$!ACTIVEFIELDZONES = [6]
$!FIELDLAYERS SHOWCONTOUR = YES
$!FIELDLAYERS SHOWMESH = NO
$!FIELD [6]
CONTOUR
{

```

```
CONTOURTYPE = LINES
COLOR =BLACK
}
BOUNDARY {COLOR = BLACK}
$!COLORSPECTRUM CONTOURCOLORMAP = GRAYSCALE
$!GLOBALCONTOUR
VAR = 5
LABELS
{
SHOW = TRUE
COLOR = BLACK
LABELWITHVALUE = FALSE
}
LEGEND
{
SHOW = TRUE
NUMFORMAT
{
FORMATTING = FIXEDFLOAT
PRECISION = 4
}
}
BOX
{
BOXTYPE = NONE
}
}
$!CONTOURLEVELS NEW
RAWDATA
7
0.1000
0.2000
0.4000
0.5000
0.6000
0.8000
1.0000
$!TWO DAXIS
AXISMODE = INDEPENDENT
XDETAIL
{
RANGEMIN = 0.0
RANGEMAX = 0.120
}
YDETAIL
{
RANGEMIN = 0.0
RANGEMAX = 0.040
}
}
$!REDRAW
$!CREATENEWFRAME
```

```

$!READDATASET
"|TECHHOME|/WORK/TEZ\CASE2 KEPSTO/TEC_98_05.DAT"
$!FRAMELAYOUT
SHOWBORDER = FALSE
SHOWHEADER = FALSE
XYPOS
{
X = 0.5
Y = 5.5
}
WIDTH = 3.5
HEIGHT = 2.5
$!ACTIVEFIELDZONES = [7]
$!FIELDLAYERS SHOWCONTOUR = YES
$!FIELDLAYERS SHOWMESH = NO
$!FIELD [7] CONTOUR
{
CONTOURTYPE = LINES
COLOR =BLACK
}
BOUNDARY {COLOR = BLACK}
$!COLORSPECTRUM CONTOURCOLORMAP = GRAYSCALE
$!GLOBALCONTOUR
VAR = 5
LABELS
{
SHOW = TRUE
COLOR = BLACK
LABELWITHVALUE = FALSE
}
LEGEND
{
SHOW = TRUE
NUMFORMAT
{
FORMATTING = FIXEDFLOAT
PRECISION = 4
}
}
BOX
{
BOXTYPE = NONE
}
}
$!CONTOURLEVELS NEW
RAWDATA
6
0.1000
0.1500
0.2000
0.3000

```

```

0.3500
0.4000
$!TWO DAXIS
AXISMODE = INDEPENDENT
XDETAIL
{
RANGEMIN = 0.0
RANGEMAX = 0.120
}
YDETAIL
{
RANGEMIN = 0.0
RANGEMAX = 0.040
}
$!REDRAW
$!CREATENEWFRAME
$!READDATASET "|TECHOME|/WORK/TEZ\CASE2_KEPS/TEC_98_025.DAT"
$!FRAMELAYOUT
SHOWBORDER = FALSE
SHOWHEADER = FALSE
XYPOS
{
X = 4
Y = 5.5
}
WIDTH = 3.5
HEIGHT = 2.5
$!ACTIVEFIELDZONES = [7]
$!FIELDLAYERS SHOWCONTOUR = YES
$!FIELDLAYERS SHOWMESH = NO
$!FIELD [7] CONTOUR
{
CONTOURTYPE = LINES
COLOR = BLACK
}
BOUNDARY {COLOR = BLACK}
$!COLORSPECTRUM CONTOURCOLORMAP = GRAYSCALE
$!GLOBALCONTOUR
VAR = 5
LABELS
{
SHOW = TRUE
COLOR = BLACK
LABELWITHVALUE = FALSE
}
LEGEND
{
SHOW = TRUE
NUMFORMAT
{

```

```
FORMATTING = FIXEDFLOAT
PRECISION = 4
}
BOX
{
BOXTYPE = NONE
}
}
$!CONTOURLEVELS NEW
RAWDATA
6
0.1000
0.1500
0.2000
0.3000
0.3500
0.4000
$!TWO D AXIS
AXISMODE = INDEPENDENT
XDETAIL
{
RANGEMIN = 0.0
RANGEMAX = 0.120
}
YDETAIL
{
RANGEMIN = 0.0
RANGEMAX = 0.040
}
$!REDRAW
$!CREATENEWFRAME

$!READDATASET
"|TECHOME/WORK/TEZ\CASE2_KEPSTO/TEC_98_05.DAT"
$!FRAME LAYOUT
SHOWBORDER = FALSE
SHOWHEADER = FALSE
XYPOS
{
X = 0.5
Y = 8
}
WIDTH = 3.5
HEIGHT = 2.5
$!ACTIVEFIELDZONES = [8]
$!FIELDLAYERS SHOWCONTOUR = YES
$!FIELDLAYERS SHOWMESH = NO
$!FIELD [8]
CONTOUR
{
```

```
CONTOURTYPE = LINES
COLOR =BLACK
}
BOUNDARY {COLOR = BLACK}
$!COLORSPECTRUM CONTOURCOLORMAP = GRAYSCALE
$!GLOBALCONTOUR
VAR = 5
LABELS
{
SHOW = TRUE
COLOR = BLACK
LABELWITHVALUE = FALSE
}
LEGEND
{
SHOW = TRUE
NUMFORMAT
{
FORMATTING = FIXEDFLOAT
PRECISION = 4
}
}
BOX
{
BOXTYPE = NONE
}
}
$!CONTOURLEVELS NEW
RAWDATA
5
0.1000
0.1500
0.2000
0.2500
0.3000
$!TWO DAXIS
AXISMODE = INDEPENDENT
XDETAIL
{
RANGEMIN = 0.0
RANGEMAX = 0.120
}
YDETAIL
{
RANGEMIN = 0.0
RANGEMAX = 0.040
}
$!REDRAW
$!CREATENEWFRAME
$!READDATASET "|TECHOME/WORK/TEZ/CASE2_KEPS/TEC_98_025.DAT"
$!FRAME LAYOUT
```

```

SHOWBORDER = FALSE
SHOWHEADER = FALSE
XYPOS
{
X = 4
Y = 8
}
WIDTH = 3.5
HEIGHT = 2.5
$!ACTIVEFIELDZONES = [8]
$!FIELDLAYERS SHOWCONTOUR = YES
$!FIELDLAYERS SHOWMESH = NO
$!FIELD [8]
CONTOUR
{
CONTOURTYPE = LINES
COLOR =BLACK
}
BOUNDARY {COLOR = BLACK}
$!COLORSPECTRUM CONTOURCOLORMAP = GRAYSCALE
$!GLOBALCONTOUR
VAR = 5
LABELS
{
SHOW = TRUE
COLOR = BLACK
LABELWITHVALUE = FALSE
}
LEGEND
{
SHOW = TRUE
NUMFORMAT
{
FORMATTING = FIXEDFLOAT
PRECISION = 4
}
}
BOX
{
BOXTYPE = NONE
}
}
$!CONTOURLEVELS NEW
RAWDATA
5
0.1000
0.1500
0.2000
0.2500
0.3000
$!TWO DAXIS

```

```

AXISMODE = INDEPENDENT
XDETAIL
{
RANGEMIN = 0.0
RANGEMAX = 0.120
}
YDETAIL
{
RANGEMIN = 0.0
RANGEMAX = 0.040
}
$!REDRAW

$!RemoveVar [MFBD]

#!MC 750
$!VarSet [MFBD] = 'C:\programs\TEC75'
$!READDATASET
"!TECHOME\WORK\TEZ\CASE2_KEPSTO\TEC_98_05.DAT"
$!FRAMELAYOUT
SHOWBORDER = FALSE
SHOWHEADER = FALSE
XYPOS
{
X = 0.5
Y = 0.5
}
WIDTH = 3.5
HEIGHT = 2.5
$!ACTIVEFIELDZONES = [9]
$!FIELDLAYERS SHOWCONTOUR = YES
$!FIELDLAYERS SHOWMESH = NO
$!FIELD [9]
CONTOUR
{
CONTOURTYPE = LINES
COLOR =BLACK
}

BOUNDARY {COLOR = BLACK}
$!COLORSPECTRUM CONTOURCOLORMAP = GRAYSCALE
$!GLOBALCONTOUR
VAR = 5
LABELS
{
SHOW = TRUE
COLOR = BLACK
LABELWITHVALUE = FALSE
}

```

```

LEGEND
{
SHOW = TRUE
NUMFORMAT
{
FORMATTING = FIXEDFLOAT
PRECISION = 4
}
}
BOX
{
BOXTYPE = NONE
}
}
$!CONTOURLEVELS NEW
RAWDATA
5
0.1200
0.1400
0.1600
0.1800
0.20000
$!TWO DAXIS
AXISMODE = INDEPENDENT
XDETAIL
{
RANGEMIN = 0.0
RANGEMAX = 0.120
}
YDETAIL
{
RANGEMIN = 0.0
RANGEMAX = 0.040
}
}
$!REDRAW
$!CREATENEWFRAME
$!READDATASET "I:\TECHHOME\WORK\TEZ\CASE2_KEPS\TEC_98_025.DAT"
$!FRAME LAYOUT
SHOWBORDER = FALSE
SHOWHEADER = FALSE
XYPOS
{
X = 4
Y = 0.5
}
WIDTH = 3.5
HEIGHT = 2.5
$!ACTIVEFIELDZONES = [9]
$!FIELDLAYERS SHOWCONTOUR = YES
$!FIELDLAYERS SHOWMESH = NO
$!FIELD [9]

```

```

CONTOUR
{
CONTOURTYPE = LINES
COLOR =BLACK
}
BOUNDARY {COLOR = BLACK}
$!COLORSPECTRUM CONTOURCOLORMAP = GRAYSCALE
$!GLOBALCONTOUR
VAR = 5
LABELS
{
SHOW = TRUE
COLOR = BLACK
LABELWITHVALUE = FALSE
}
LEGEND
{
SHOW = TRUE
NUMFORMAT
{
FORMATTING = FIXEDFLOAT
PRECISION = 4
}
}
BOX
{
BOXTYPE = NONE
}
}
$!CONTOURLEVELS NEW
RAWDATA
5
0.1200
0.1400
0.1600 †
0.1800
0.20000
$!TWO DAXIS
AXISMODE = INDEPENDENT
XDETAIL
{
RANGEMIN = 0.0
RANGEMAX = 0.120
}
YDETAIL
{
RANGEMIN = 0.0
RANGEMAX = 0.040
}
}
$!REDRAW
$!RemoveVar |MFBD|

```

APPENDIX C

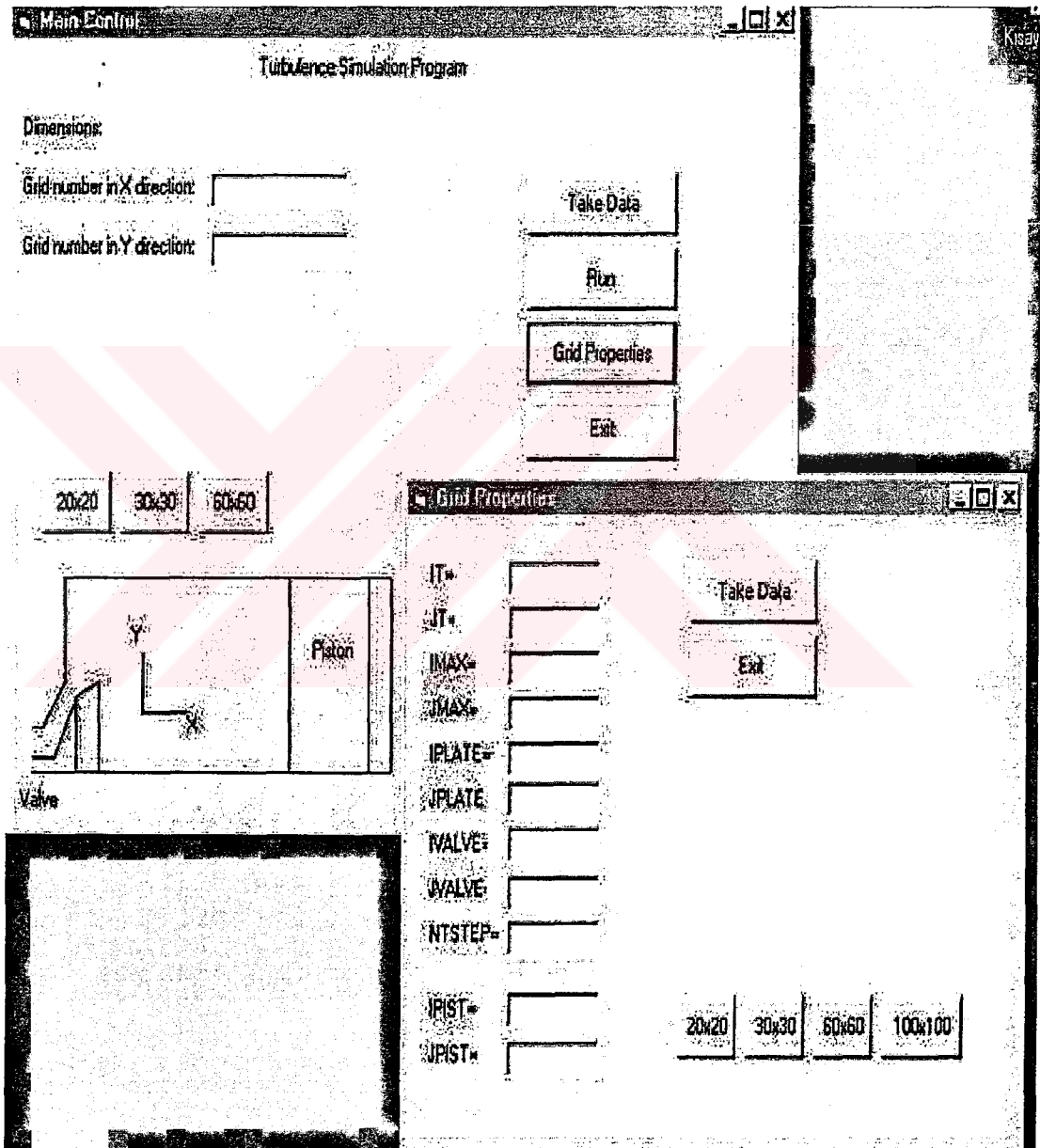


Figure C. 1 Preprocessing tool, developed by using Visual Basic programming language.

CURRICULUM VITAE

Barış YILMAZ was born on April 4, 1974 in Kars, Turkey. After graduating from Adana Science High School, he started his degree in Nuclear Engineering at Hacettepe University in 1991. He entered the Master of Science program of Mechanical Engineering at Marmara University in 1999. Meanwhile, he joined the academic staff of Faculty of Engineering of Marmara University as a Research Assistant in October 1999. He has been working as a Research Assistant in Marmara University for three years.



Dr. YILMAZ BARIS
YILMAZ BARIS